

NUMERICAL CALCULATION OF TRANSPORT PROPERTIES OF ROCK WITH
GEOMETRY OBTAINED USING SYNCHROTRON X-RAY COMPUTED
MICROTOMOGRAPHY

A Thesis Submitted to the College of
Graduate Studies and Research
In Partial Fulfillment of the Requirements
For the Degree of Master of Science
In Geology
Department of Geological Sciences
University of Saskatchewan
Saskatoon

By

MICHAEL BRIAN BIRD

PERMISSION TO USE

In presenting this thesis in partial fulfilment of the requirements for a Postgraduate degree from the University of Saskatchewan, I agree that the Libraries of this University may make it freely available for inspection. I further agree that permission for copying of this thesis in any manner, in whole or in part, for scholarly purposes may be granted by the professor or professors who supervised my thesis work or, in their absence, by the Head of the Department or the Dean of the College in which my thesis work was done. It is understood that any copying or publication or use of this thesis or parts thereof for financial gain shall not be allowed without my written permission. It is also understood that due recognition shall be given to me and to the University of Saskatchewan in any scholarly use which may be made of any material in my thesis.

DISCLAIMER

Avizo[®] (<http://www.vsg3d.com/avizo/overview>) and COMSOL Multiphysics[®] (<http://www.comsol.com>) were exclusively used to meet the thesis requirements for the degree of Master of Science at the University of Saskatchewan. Reference in this thesis to any specific commercial products, process, or service by trade name, trademark, manufacture, or otherwise, does not constitute or imply its endorsement, recommendation, or favouring by the University of Saskatchewan. The views and opinions of the author expressed herein do not state or reflect those of the University of Saskatchewan, and shall not be used for advertising or product endorsement purposes.

Requests for permission to copy or to make other use of material in this thesis in whole or part should be addressed to:

Head of the Department of Geological Sciences
University of Saskatchewan
Saskatoon, Saskatchewan S7N 5E2
Canada

OR

Dean
College of Graduate Studies and Research
University of Saskatchewan
107 Administration Place
Saskatoon, Saskatchewan S7N 5A2
Canada

ABSTRACT

Macroscopic properties of rocks are functions of pore-scale geometry and can be determined from laboratory experiments using rock samples. Macroscopic properties can also be determined from computer simulations using 3D pore geometries derived from various imaging techniques. Using 3D imagery and computer simulations, we can calculate the porosity, permeability, formation resistivity factor and cementation exponent in reservoir drill cores.

The objective of this thesis was to develop a workflow using Synchrotron X-ray Computed Microtomography (CMT) images and commercially available software in order to determine the macroscopic properties in reservoir drill cores for Midale Marly (M0) and Vuggy Shoal (V6) rocks. The workflow started by using CMT data that provided three-dimensional images of the reservoir rocks taken from drill cores in the Weyburn oil field. The resulting CMT grey scale images were used to isolate the pore space in the rock image. A three-dimensional mesh, representing the pore space, was then used to obtain the solution of the Navier-Stokes equations for an incompressible fluid and Laplace's equation for electrical current flow. Solutions of the Navier-Stokes equations were computed with different inlet pressures for the same pore geometry in order to confirm a direct proportionality between the mass fluid flux and pressure gradient as Darcy's Law specifies. Previously measured laboratory transport properties were compared with my calculated transport properties on a smaller sub-volume of the same rock core imaged using 0.78 μm resolution CMT images. For the Midale Marly rock, the calculated permeability ranged from 0.01 to 3.53 mD. The formation resistivity factor ranged from 29.3 to 309.43 and the cementation exponent ranged from 1.99 to 2.10. The sample was verified to be nearly isotropic as the permeability was similar for three orthogonal fluid flow directions. Even though the sub-volume analyzed was smaller than a Representative Elementary Volume (REV), the results are within an order of magnitude of the previously calculated laboratory results as completed by Glemser (2007) and fall on the same power law trend. A Vuggy (V6) sample was investigated after the sample had been exposed to CO_2 , and dissolution within the rock matrix resulted in large visible pore spaces. Using 7.45 μm resolution CMT images, the permeability for a large isolated pore could not be calculated using the previous workflow due to computer memory limitations. Resampling enabled the data to fit into the available computer memory.

The permeability values ranged from $2.66 \cdot 10^5$ to $8.59 \cdot 10^5$ mD for resampling the CMT images from 2x to 10x.

ACKNOWLEDGEMENTS

I would like to thank my advisor, Dr. Samuel Butler for providing the opportunity to complete this thesis under his guidance. His mentoring and extraordinary knowledge created a great positive environment for me to advance my research skills and enhance my mathematical ability.

Thank you to my committee members, Dr. Chris Hawkes, Dr. Tom Kotzer and Dr. James Merriam for their constructive feedback. They all demonstrated scheduling flexibility for meeting with me on multiple weekends to discuss my progress. Thank you to Dr. Ian Stavness for externally examining this thesis and providing valuable feedback.

Thank you to the Petroleum Technology Research Centre (PTRC), the National Science and Engineering Research Council of Canada (NSERC) and GENIVAR Inc. for financially supporting this study.

Thank you to my family and friends for the encouragement and support during this thesis. A special thanks to my GENIVAR co-workers and friends, Samuel Teklé, Bud Norris and Kevin Henshaw for providing thesis input, accommodating my work schedule and allowing me to develop new insights into the world of bridge engineering. Your patience with me talking about practical applications of advanced calculus and the novelty of using synchrotrons was appreciated. Your attention to detail and acute insight as professional engineers encouraged me complete my thesis and also helped me to expand my skillset as a professional engineer. Thank you also to Sandor Sule for his friendship, random coffee breaks while working late at night, and helping me acquire reference materials.

Thank you to my great friends Dion Newton, Dwight Newton and Paul Sly for graciously letting me stay at their house countless times and to my sister, Allison Rawlings, for the home cooked meals during my visits.

Most of all, thank you to my parents, Brian and Judy Bird, for their inspiration, encouragement and unconditional love. I could not have completed this thesis without you.

TABLE OF CONTENTS

	Page
PERMISSION TO USE	i
DISCLAIMER	i
ABSTRACT	ii
ACKNOWLEDGEMENTS	iv
TABLE OF CONTENTS	v
LIST OF TABLES	viii
LIST OF FIGURES	ix
LIST OF SYMBOLS	xv
LIST OF ABBREVIATIONS	xvii
1 INTRODUCTION	1
1.1 Continuum Mechanics in Porous Media	1
1.2 Imaging Pore Scale Structure	4
1.2.1 Pore Imaging Techniques	6
1.2.2 High Resolution Imaging using the Synchrotron	8
1.3 Rock Core Sample Used	10
1.3.1 Estimating Porosity, Permeability, Formation Factor and Cementation Exponent from Pore Scale Geometries (from Glemser, 2007)	13
1.4 Weyburn Oilfield Background	17
1.5 Oil Recovery Factors	19
1.6 Numerical Methods	21
2 PORE EXTRACTION METHODOLOGY	24
2.1 Introduction	24
2.2 Computer Specifications	24
2.3 Importing Synchrotron core data into Avizo Fire	25
2.4 Avizo Fire Workflow	25
2.5 Import Data	26
2.6 Crop Data	27
2.7 Threshold and Binarize Image	28
2.8 Skeletonization	33
2.9 Filter Data	35

2.10	Determine Voxel Connections	37
2.11	Generate Surface	38
2.12	Export Surface	43
3	PHYSICS METHODOLOGY	45
3.1	COMSOL Multiphysics Workflow	45
3.2	Import Geometry	45
3.3	Add Physics	47
3.4	Set Initial Values and Boundary Conditions	48
3.5	Mesh 3D Volume	51
3.6	Partial Differential Equation Solver Considerations	52
3.7	Representative Elementary Volume Surface	53
3.8	Estimating Porosity, Permeability, Formation Resistivity Factor and Cementation Exponent from Pore Scale Geometries	62
4	RESULTS 1, HIGH RESOLUTION MARLY SAMPLES (0.78 μm RESOLUTION)	64
4.1	Darcy's Flow Regime Verification	64
4.2	Fluid Flow and Electrical Current Density Results	65
4.3	Darcy Velocity Scaling to Reservoir Conditions	99
4.4	Summary for Results 1, High Resolution Marly Samples (0.78 μm)	100
5	RESULTS 2, POST CO₂ FLOOD SAMPLE (7.45 μm RESOLUTION)	102
5.1	Core Sample Used in Results 2	102
5.2	Smooth CMT data by resampling	103
5.3	Import and Crop data	103
5.4	Threshold and binarize data	104
5.5	Resample test (0.78 μm CMT data)	105
5.6	Darcy's Flow Regime Verification	109
5.7	Resample data (7.45 μm CMT data)	110
5.8	Darcy Velocity Scaling to Reservoir Conditions	125
5.9	Resampling Observations	127
5.10	Summary for Results 2, Post CO ₂ Flood Sample (7.45 μm)	128
6	OVERALL SUMMARY	130
6.1	Recommendations for Future Research	134

		Page
APPENDIX A	Representative Elementary Volume	A-1
APPENDIX B	Scaling Factors for Modifying Equations to Real World Values	B-1
APPENDIX C	Computer Specifications	C-1

LIST OF TABLES

	Page
Table 1.1	Applications of imaging techniques to porous media systems 5
Table 1.2	Core samples within the Weyburn Oilfield that were used in previous research. The representative lithological unit, well location, sample depth and CMT resolution is displayed (from Glemser 2007)..... 10
Table 1.3	Porosity and permeability in the Weyburn Oilfield (Churcher et al., 1994; Glemser, 2007)..... 13
Table 1.4	Porosity, permeability and resistivity for the KD-03-18 sample using the permeability core, 10 μm and 0.78 μm resolution CMT core (Glemser, 2007). 14
Table 1.5	Enhanced Oil Recovery Methods (from Al-Mjeni et al.,2011) 20
Table 2.1	Connectivity of Regions in the KD-18-03 Subsample 38
Table 3.1	Representative Elementary Volume (REV) Porosity Change Investigation 56
Table 3.2	Porosity change for Random 200 Voxel Regions..... 57
Table 4.1	Darcy's Flow Regime Verification for [Model 1]..... 64
Table 4.2	Calculated Properties for the KD-18-03 Subsample..... 68
Table 4.3	Computational results for the KD-18-03 Subsample..... 70
Table 4.4	Results for Permeability, Formation Resistivity Factor and Cementation Exponent 71
Table 4.5	Archie's Law calculation of 'a' for the KD-18-03 Subsample..... 73
Table 4.6	Common cementation exponent 'm' values 73
Table 4.7	Cropped Regions used inside KD-18-03, subsection 3 98
Table 4.8	Darcy Velocity Comparision of Marly (M3) and Marly (M0) Core Samples... 100
Table 5.1	Calculated Permability using Resampled Data on Model 5 107
Table 5.2	Darcy's Flow Regime Verification 110
Table 5.3	Calculated Properties for [Model 6] with Resampling 112
Table 5.4	Calculated Permeability with Resampling for [Model 7] 116
Table 5.5	Calculated Properties for [Model 8] 121
Table 5.6	Subsample Volumes used in Results 2 125
Table 5.7	Darcy Velocity Comparision for Vuggy (V6) Core Sample 126

LIST OF FIGURES

Page

Figure 1.1 (A) A 2D slice inside 3D sub-volume from a synchrotron image representing the inside of a Midale Marly rock. The 8 bit greyscale image ranges from the pore space (grey-black, '0') to the rock matrix (white, '255') with a range from '0' to '85' representing the rock pore space. (B) The isolated area has four isolated regions, as highlighted, for calculating the average porosity. The green square is an estimate of the size of the Representative Element Volume (REV) and all other colored squares are smaller than the REV. (C) The porosity vs. characteristic length in terms of an REV (after Bear, 1972)..... 3

Figure 1.2 Image of the European Synchrotron Radiation Facility (ESRF) in Grenoble, France. (ESRF / P. Ginter, 2012)..... 8

Figure 1.3 Schematic of the CMT apparatus (from Glemser, 2007)..... 9

Figure 1.4 Sample cores taken from the Weyburn oil field. Thesis work focused on the KD-18-03 Marly core sample, as circled in red. (A) Cores used in CMT analysis. (B) Larger diameter cores used in petrophysical laboratory measurements. KD 03-18 was previously studied using CMT, petrophysical laboratory measurements and mineralogical analysis (from Glemser 2007). 11

Figure 1.5 Sample cores with similar dimensions to KD-18-03. (A) Large diameter core used in petrophysical laboratory measurements. (B) Core used in 10 μm CMT analysis. (C) Hole that was drilled to obtain the sample D. (D) Representative region of the core region used for 0.78 μm CMT based core analysis. The reference object is a Canadian dollar which has a diameter of 26.5 mm (Royal Canadian Mint, 2012). 12

Figure 1.6 (A) Location of Weyburn and Midale Oil Fields located in southeast Saskatchewan, Canada near the Unites States border (screenshot from Google Maps). The length of the oilfield is about 180 km horizontally. The approximate location of the Williston basin is shown as extending into Saskatchewan and Manitoba (Canada) and Montana, North Dakota and South Dakota (United States). (B) The Weyburn oilfield study area located immeditely west of the Midale oilfield. Cenovus Energy is the majority owner and operator of the Weyburn Unit, and Apache Canada is the operator of the Midale Unit. (C) Drilling locations for the Marly and Vuggy core samples. The Midale Marly (MO) unit called KD-18-03 is identified as the Unique Well Identifier (UWI) format 12-19-6-13-W2 (B and C after Glemser, 2007). 18

Figure 2.1	(A) Combining the CMT data from KD-18-03 via post-processing in Avizo. The top and bottom section are referred to as subsection 1 and subsection 8 respectively. (B) An isolated 8 bit greyscale image from cropped section is also displayed from subsection 3. The voxels in this subsample have a resolution of 0.78 μm , so the actual scale of this 30 x 30 x 30 voxel subsample is 23.4 μm in all directions.	27
Figure 2.2	(A) Isolated Greyscale 8 bit image from KD-03-18. The 3D figure is 30 x 30 x 30 voxels (23.4 x 23.4 x 23.4 μm). (B) The 2D orthoslice section, as isolated from the 3D image, with dimensions of 30 x 30 voxels (23.4 x 23.4 μm).	28
Figure 2.3	(A) The 3D cropped orthoslice section of slice # 160 (out of a total from slice # 0 to slice #255). The 3D cropped index values are 600 to 1099, 1200 to 1699, 0 to 255 in the x,y and z directions respectively. The 3D histogram is represented by 500 x 500 x 8 voxels at 0.78 μm resolution for a real scale resolution of 390 x 390 x 200 μm . (B) Histogram of Greyscale 8 bit image from KD-03-18, subsection 3. The threshold value of 85 is shown on the histogram plot.	30
Figure 2.4	(A) 8 bit greyscale image. (B) Thresholded image to 85 where the red voxels are shown that represent the pore space. Both image scales are 30 x 30 voxels (23.4 x 23.4 μm).	31
Figure 2.5	Binary Image using Quantification-Thresholding (from Visilog, 2010)	32
Figure 2.6	(A) Thresholded Image and (B) Binarized Image. Both image scales are 30 x 30 voxels (23.4 x 23.4 μm).	32
Figure 2.7	Skeletonization of the Binary Image.....	33
Figure 2.8	Skeleton of Binary Image with Orthoslices of both binary and 8 bit greyscale CMT images.	34
Figure 2.9	Filtering the signal using a moving average (from Visilog, 2010)	35
Figure 2.10	Binary image before (A) and after (B) a 3D Gauss filter was applied. The changes between the images is noted in red circles. The scale of both images is 30 x 30 voxels (23.4 x 23.4 μm).	36
Figure 2.11	Connectivity of elements. (A) Left image is 6 voxel connections. (B) middle image is 18 voxel connections. (C) Right image is 26 voxel connections. (Visualization Sciences Group, 2010a)	37
Figure 2.12	Connectivity of Regions in the Subsample as listed in Table 2.1. The scale of the image is 30 x 30 x 30 voxels (23.4 x 23.4 x 23.4 μm).	39

Figure 2.13	(A) Surface of all connected voxels in subvolume. (B) Surface of largest connected voxels in subsample (B). The scale for both images is 30 x 30 x 30 voxels (23.4 x 23.4 x 23.4 μm).....	40
Figure 2.14	(A) Spatial plot of connected pore space using the AutoSkeleton method. (B) Surface of all connected regions in subsample. (C) Spatial plot of connected pore space superimposed inside the surface of all connected regions in a subsample. The scales of all images is 30 x 30 x 30 voxels (23.4 x 23.4 x 23.4 μm).....	41
Figure 2.15	RemeshSurface algorithm used for reducing the number of elements in a mesh surface. (A) Non-remeshed surface representing the pore space. (B) The surface was remeshed to 59% of the original mesh using the RemeshSurface algorithm. The scales of the images is 30 x 30 x 30 voxels (23.4 x 23.4 x 23.4 μm).....	42
Figure 3.1	View of triangular surface imported into COMSOL. The connected pore space is shown after exporting the STL file from Avizo. The image size is 30 x 30 x 30 voxels (23.4 x 23.4 x 23.4 μm).....	46
Figure 3.2	Setting Boundary Conditions and Initial Values on the STL import mesh. The image size is 30 x 30 x 30 voxels (23.4 x 23.4 x 23.4 μm).....	49
Figure 3.3	3D tetrahedral mesh representing both the surface and the domain. (A) The domain mesh is displayed with a transparency level of 70% to help visualize mesh complexity. (B) Magnified section of the surface mesh. The image size is 30 x 30 x 30 voxels (23.4 x 23.4 x 23.4 μm).....	51
Figure 3.4	(A) A 2D slice inside a 3D sub-volume from a synchrotron image representing the inside of a Midale Marly rock. The 8 bit greyscale ranges from the pore space (grey-black, 0) to the rock matrix (white, 255) with a threshold value of 85 representing the rock pore space. (B) The isolated sub-volume has eight isolated regions for calculating the average porosity. The four largest squares are larger than a REV and all other colored squares are smaller than the a REV. (C) The porosity vs. characteristic length in terms of a REV (after Bear, 1972). The images range from a length scale of 1.6 to 858 μm . The black, red, blue and green squares are above the side length, L_0 , and are considered to be a REV for porosity.	55
Figure 3.5	Porosity (%) vs. Log of Sample Length (μm)	58
Figure 3.6	Porosity and Standard Deviation vs. Log of Sample Length (μm).....	59
Figure 3.7	REV region located within the Midale Marly KD-18-03 subsample. The 3D dimensions of the box are 200 x 200 x 200 voxels (156 x 156 x 156 μm).....	60
Figure 3.8	Connected pore space from a 200 voxel ³ (156 μm ³) region within KD-18-03. ..	61

Figure 4.1	Flow diagrams and electrical current density diagrams. A, B and C, show solutions to the Navier-Stokes equations in the x-direction, y-direction and z-direction respectively. D, E and F, show solutions to Laplace's equations in the x-direction, y-direction and z-direction respectively. The sample size is 30 x 30 x 30 voxel (23.4 x 23.4 x 23.4 μ m). The streamlines show the Current Density Magnitude and Velocity Magnitude. The red color represents the high values while the blue color represents the low values.	66
Figure 4.2	Log of Formation Resistivity Factor (F) vs. Log of Effective Porosity (%).....	72
Figure 4.3	Log of Permeability (mD) vs. Log of Porosity (%).....	74
Figure 4.4	Reference figure used to display the representative views of Figures 4.5 to 4.22 (A) 3D orthographic view (B) 2D view looking in the z- direction (view of outside face looking inside). (C) 2D view looking in the x- direction (view of outside face looking inside). (D) 2D view looking in the y- direction (view of outside face looking inside). (B,C,D) All views show 2D a view looking from outside the 2D face to inside the 3D cube.....	75
Figure 4.5	Flow diagrams from KD-18-03 subsample (Model 1-y5).	77
Figure 4.6	Electrical current density diagrams from KD-18-03 subsample (Model 1-y5).	78
Figure 4.7	Flow diagrams from KD-18-03 subsample (Model 1-z5).	79
Figure 4.8	Electrical current density diagrams from KD-18-03 subsample (Model 1-z5). ..	80
Figure 4.9	Flow diagrams from KD-18-03 subsample (Model 1-x5).	81
Figure 4.10	Electrical current density diagrams from KD-18-03 subsample (Model 1-x5).	82
Figure 4.11	Flow diagrams from KD-18-03 subsample (Model 2-z4).	84
Figure 4.12	Electrical current density diagrams from KD-18-03 subsample (Model 2-z4). ..	85
Figure 4.13	Flow diagrams from KD-18-03 subsample (Model 2-x1).	86
Figure 4.14	Electrical current diagrams from KD-18-03 subsample (Model 2-x1).....	87
Figure 4.15	Flow diagrams from KD-18-03 subsample (Model 2-y1).	88
Figure 4.16	Electrical current density diagrams from KD-18-03 subsample (Model 2-y1).	89
Figure 4.17	Flow diagrams from KD-18-03 subsample (Model 3-y1).	91
Figure 4.18	Electrical current density diagrams from KD-18-03 subsample (Model 3-y1).	92
Figure 4.19	Flow diagrams from KD-18-03 subsample (Model 4-y1).	94

Figure 4.20	Electrical current density diagrams from KD-18-03 subsample (Model 4-y1).	95
Figure 4.21	Flow diagrams from KD-18-03 subsample (Model 4-x1).	96
Figure 4.22	Electrical current density diagrams from KD-18-03 subsample (Model 4-x1).	97
Figure 5.1	A large pore was selected that had observable CO ₂ dissolution. (A) The orthoslice view displayed shows image 50 out of 100 images. (B) The region of dissolution was isolated to a 100 x 100 voxel region using the coordinates 1250:1350, 1450:1550, 0:100. The physical subsample size is 745 x 745 μm.	104
Figure 5.2	Thresholding the 100 voxel region of segment 2, slice 4. (A) Image thresholding value of 130. (B) Image thresholding value of 160. (C) Image thresholding value of 143. The thresholding region was isolated to a 100 x 100 voxel region. The physical subsample size is 745 x 745 μm.....	105
Figure 5.3	Flow diagrams to compare resampling on KD-18-01 subsample. (A) Image is the non-resampled image (1.0x resampled). (B) Image is 1.5x resampled. (C) Image is 2.0x resampled. (D) Image is 3.0x resampled. All image sizes are 30 x 30 x 30 voxels (23.4 x 23.4 x 23.4 μm).....	108
Figure 5.4	Flow diagram with image 3.0x resampled. Image size is 30 x 30 x 30 voxels (23.4 x 23.4 x 23.4 μm).	109
Figure 5.5	Connected pore space of resampled images A through F. The images were resampled 1x (non resampled), 2x, 3x, 4x, 6x and 8x resampled respectively. The figure displays 5,000 streamlines of the velocity field originating from the inlet at the top surface. The streamline color is the pressure (red = high; blue = low). The inlet boundary condition is a pressure of '1' [N/voxel ²] and the bottom outlet boundary condition is a pressure of '0' [N/voxel ²]. The surface mesh is shown in black to indicate how the mesh complexity is reduced with increased resampling. The subsample size is 100 ³ voxels ³ (745 ³ μm ³) with a CMT resolution of 7.45 μm.	113
Figure 5.6	Flow diagrams from Model 6-z4 (non resampled). The subsample size is 100 ³ voxels ³ (745 ³ μm ³) with a CMT resolution of 7.45 μm.....	114
Figure 5.7	Connected pore space of resampled images A through F. The images were resampled 2x, 3x, 4x, 6x, 8x and 10x respectively. The figure displays 1,000 streamlines of the velocity field originating from the inlet at the top surface. The streamline color is the velocity magnitude. The inlet boundary condition is a pressure of '1' [N/voxel ²] and the bottom outlet boundary condition is a pressure of '0' [N/voxel ²]. The surface mesh is shown in black to indicate how	

the mesh complexity is reduced with increased resampling. The subsample size is 200^3 voxels³ ($1490^3 \mu\text{m}^3$) with a CMT resolution of $7.45 \mu\text{m}$ 117

Figure 5.8 Flow diagrams from Model 7-x1 (2.0 x resampled). The subsample size is 200^3 voxels³ ($1490^3 \mu\text{m}^3$) with a CMT resolution of $7.45 \mu\text{m}$ 119

Figure 5.9 Flow diagrams from Model 8-x1 (non resampled). The subsample size is 100^3 voxels³ ($745^3 \mu\text{m}^3$) with a CMT resolution of $7.45 \mu\text{m}$ 123

Figure 5.10 Electrical current density diagrams from Model 8-x1 (non resampled). The subsample size is 100^3 voxels³ ($745^3 \mu\text{m}^3$) with a CMT resolution of $7.45 \mu\text{m}$ 124

LIST OF SYMBOLS

Symbol	Meaning
\emptyset	Porosity, %
M_{wet}	Measured mass for the wet core, g
M_{dry}	Measured mass for dry core, g
ρ_{H_2O}	Density of water, $\frac{kg}{m^3}$
V_{sample}	Sample volume, m^3
k	Permeability, mD
μ	Dynamic viscosity of the test fluid, $Pa \cdot s$
Q	Flow rate, $\frac{m}{s}$
L	Length of the sample, m
A	Cross-sectional area of the sample, m^2
F	Formation resistivity factor
R_o	Resistivity of the brine saturated rock core, $\Omega \cdot m$
R_w	Resistivity of the brine, $\Omega \cdot m$
m	Cementation exponent
x	Cartesian component in the x-direction
y	Cartesian component in the y-direction
z	Cartesian component in the z-direction
ρ	Density, $\frac{kg}{m^3}$
\vec{u}	Velocity vector, $\frac{m}{s}$
p	Pressure, Pa

τ	Viscous stress tensor, Pa
\vec{j}	Current density vector, $\frac{A}{m^2}$
σ	Conductivity, $\frac{S}{m}$
\vec{E}	Electric field, $\frac{V}{m}$
V	Voltage, $\frac{J}{C}$
q_{ave}	Average mass fluid flux, $\frac{m}{s}$
dp/dx	Pressure gradient, $\frac{Pa}{m}$
R	Resistance, $\frac{V}{I}$
I	Current, $\frac{V}{\Omega}$
m	Cementation exponent

LIST OF ABBREVIATIONS

Abbreviation	Full Meaning
ASP	Alkali-Surfactant-Polymer
atm	Standard Pressure, defined as 101.325 <i>kPa</i>
BSE	Backscattered Electron
CCD	Charge-coupled Device
CSLM	Confocal Scanning Laser Microscopy
CMT	Computed Microtomography
COMSOL	COMSOL Multiphysics software
CT	Computed Tomography
CVM	Control Volume Method
EOR	Enhanced Oil Recovery
EPMA	Electron Probe Micro-Analysis
ESEM	Environmental Scanning Electron Microscopy
ESRF	European Synchrotron Radiation Facility
FDM	Finite Difference Method
FIB - SEM	Focused Ion Beam - Scanning Electron Microscopy
FEM	Finite Element Method
FVM	Finite Volume Method
IFT	Interfacial Tension
LAC	Linear Attenuation Coefficient
LBM	Lattice Boltzmann Methods
MRI	Magnetic Resonance Imaging
NMR	Nuclear Magnetic Resonance
PDE	Partial Differential Equation
PIXE	Proton Induced X-ray Emission
PIXE-T	Proton Induced X-ray Emission - Tomography
PVI	Photoluminescence Volumetric Imaging
REV	Representative Elementary Volume

ROI	Region of Interest
SEM	Scanning Electron Microscopy
SM	Spectral Method
SRXCTM	Synchrotron Radiation X-ray Cryo-tomographic Microscopy
STIM	Scanning Transmission Ion Microscopy
STIM-T	Scanning Transmission Ion Microscopy Tomography
TEM	Transmission Electron Microscopy
TLM	Transmitted Light Microscopy
UWI	Unique Well Identifier
WAG	Water-Alternating-Gas
XTM	X-Ray Topographic Microscopy

1 INTRODUCTION

1.1 Continuum Mechanics in Porous Media

Macroscopic properties of rocks like permeability, porosity and electrical conductivity are functions of pore-scale geometry. Macroscopic properties can be determined from laboratory experiments on large (cm scale) samples. Increasingly, macroscopic properties are being determined from computer simulations using 3D pore geometries derived from various imaging techniques. Due to complex geometry, computers are used to solve numerical approximations to the partial differential equations describing transport phenomena. Using 3D imagery and computer simulations, we can investigate a rock sample in many ways that are not possible with laboratory experiments alone. For example, we can visualize the flow inside the complex geometry and investigate hydrodynamic dispersion and the transport of chemical species with the pore walls. Multiphase flow can also be completed to simulate CO₂ injection. The rock sample can also be meshed in addition to the pore space to simulate thermal conductivity and elastic properties.

The objective of this thesis was to develop a workflow in order to determine the macroscopic properties and visualize the flow in a reservoir drill core of a Midale Marly and Vuggy Shoal rock. Other researchers have developed advanced computational petrophysical characterization incorporating research software (Carroll et al., 2011; Blunt et al., 2012; Mostaghimi et al., 2013; Wildenschild et al., 2012; Piller, et al., 2009). The advantage of this workflow is that I use commercial software with Multiphysics capabilities.

The workflow included thresholding, filtering, and extracting the porous network from the Synchrotron X-ray Computed Microtomography (CMT) data. It also included solving the Navier-Stokes equations for the fluid flow and Laplace's equation for the electrical current flow. The workflow started by using CMT data that provided us with high resolution three-dimensional images of the reservoir rocks taken from drill cores in the Weyburn oil field. The resulting CMT grey scale images were filtered and then used to isolate the pore space in the rock image. A three-dimensional finite element mesh, representing the pore spaces, was then used to obtain the solution of the Navier-Stokes equations for an incompressible fluid and

Laplace's equation for electrical current flow. The incompressible fluid flow through the porous network was verified to be in the Darcy flow regime, and the permeability of the CMT sub-sample was calculated based on a smaller version of the same sub-sample used previously for the laboratory permeability measurement. The computed macroscopic results were then compared with laboratory measurements to check the validity of the developed workflow created using imaged synchrotron CMT data.

Figure 1.1 shows a 2D slice inside a 3D sub-volume from a synchrotron image representing the inside of the Midale Marly rock used in this investigation. The resolution of this data is $0.78 \mu\text{m}$, as imaged at the European Synchrotron Radiation Facility (ESRF) in Grenoble, France. The dark grey areas signify the pore space and lighter areas signify the rock matrix. The image size, as shown in Figure 1.1 A, is $1597 \times 1597 \mu\text{m}$ in the x and y directions respectively. We consider a macroscopic property, such as porosity, within squares of side length L . In Figure 1.1 B, we show concentric squares of increasing L . The largest image sub-sample size, as shown in green, is $702 \times 702 \mu\text{m}$ in the x and y directions. In Figure 1.1 C, porosity is shown as a function of L and it can be seen to fluctuate strongly with L until L exceeds L_0 at which point the square includes a statistically representative sample of the rock (Bear, 1972). The porosity, shown in Figure 1.1 C, was not actually measured for each value of L , and is shown to demonstrate the possible changes in porosity with changes in L . A 3D cube with side length L_0 is called the Representative Element Volume (REV). If the medium is heterogeneous, then there is a larger length scale at which macroscopic properties change and whose length may be outside the REV. The rock may be heterogeneous on a larger scale length scales due to features such as fractures. At the larger length scales, the porosity would no longer be constant.

An important aspect to learn from our study is whether we could solve for fluid flow in a volume as large as an REV. The volume is considered to be an REV if the permeability was consistent even though the box size had increased. An estimate of the actual REV for porosity, based on the Midale Marly rock synchrotron data, was investigated later in this thesis.

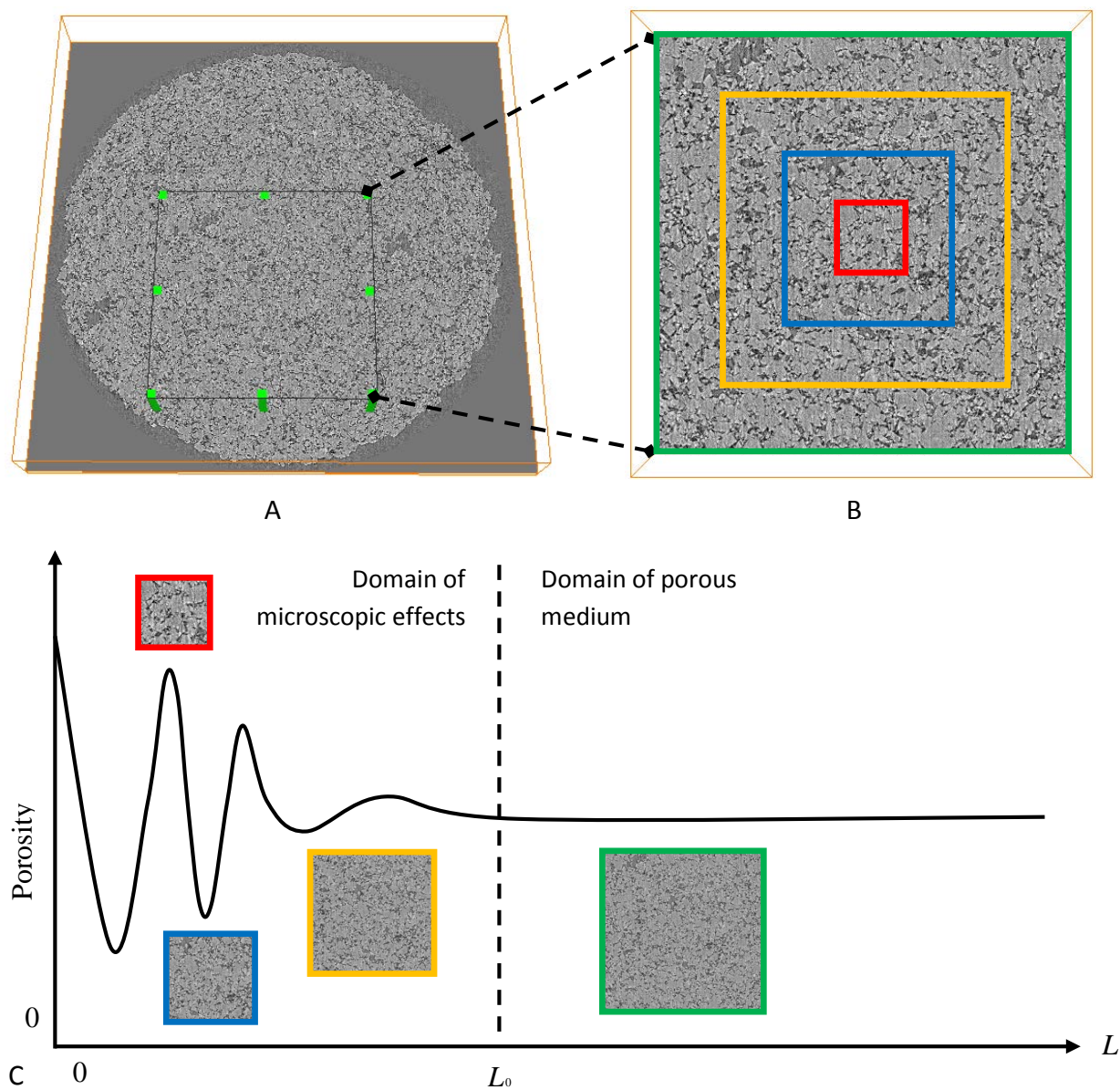


Figure 1.1 (A) A 2D slice inside 3D sub-volume from a synchrotron image representing the inside of a Midale Marly rock. The 8 bit greyscale image ranges from the pore space (grey-black, '0') to the rock matrix (white, '255') with a range from '0' to '85' representing the rock pore space. (B) The isolated area has four isolated regions, as highlighted, for calculating the average porosity. The green square is an estimate of the size of the Representative Element Volume (REV) and all other colored squares are smaller than the REV. (C) The porosity vs. characteristic length in terms of an REV (after Bear, 1972).

1.2 Imaging Pore Scale Structure

In this study, images were based on synchrotron X-ray tomography. However, many different imaging techniques exist. Table 1.1 gives many examples of studies of pore structure in different media using different imaging techniques and is updated from Al-Raoush & Willson, 2005. I will briefly summarize these various imaging methods. Table 1.1 is not exhaustive, but a summary of various methods and resolutions used.

Table 1.1 Applications of imaging techniques to porous media systems

System	Resolution	Media	Measured properties	Reference
X-ray CT	1.25 x 1.25 x 2 mm ³	Soil, glass beads	Soil bulk density	Petrovic et al. (1982) **
Synchrotron CMT	10 μm	Fontainebleau sandstone	Topology and connectivity	Spanne et al. (1994) **
Photoluminescence volumetric imaging (PVI)	1 μm	Glass beads	Porosity, volume fractions, and specific surface area	Montemagno and Gray (1995) **
X-ray CMT	7.5 μm	Fontainebleau sandstone	Porosity, volume fractions, permeability and connectivity	Auzerais et al. (1996) **
Nuclear Magnetic Resonance Imaging (NMR)	14.5 x 14.5 x 37 μm ³	Glass filter system	Pore size distribution	Pauli et al. (1996)
X-ray CT	400 μm	Rock samples	Porosity	Klobes et al. (1997) **
Positron emission tomography (PET)	*	Sandy sediment soil	Visualization of fluid transport through sample	Kahalili et al. (1998) **
Synchrotron CMT	2.7 μm	North Sea Brent Sandstone	Permeability, lattice Boltzmann	Coles et al. (1998)
Environmental Scanning electron microscopy (ESEM)	~1 μm	North Sea Brent Sandstone	Wettability and fluid flow in reservoir rocks	Combes et al. (1998)
X-ray CT	*	Glass beads	Volume fractions	Clausuitzer and Hopmans (1999) **
Synchrotron CMT	6 μm	Fontainebleau sandstone	Geometrical analysis	Lindquist and Venkatarangan (1999) **
Scanning electron microscopy (SEM)	1.6 μm	Silty and clayey quartz	Porosity, permeability, and specific surface area	Solymar and Fabricius (1999) **
Scanning transmission electron tomography (STIM-T)	1 μm	Ceramic material	Density contrast	Moretto et al. (2001)
Various	Various	Glass Beads	Porosity, volumetric water content	Wildenschild et al. (2002) **
FIB-SEM	5 nm	Siliceous Mudstones	Nanometer pore structure, permeability pathways	Loucks, Reed, Ruppel & Jarvie (2009)
Synchrotron CMT	0.74 μm	Soil Peds	Porosity, permeability, Lattice Boltzmann	Khan et al. (2011)

*Resolution is of the order of mm or not provided by the author. ** as quoted from Table 1 in (Al-Raoush et al., 2005)

1.2.1 Pore Imaging Techniques

A brief review of pore imaging techniques used in Table 1.1 is presented below. A single intrusive method, or destructive method, as mentioned in Table 1.1 is Focused Ion Beam - Scanning Electron Microscopy (FIB-SEM), all other methods are non-destructive, and include the electron microscope, the environmental scanning electron microscopy (ESEM), scanning ion microscopy tomography (STIM-T), nuclear magnetic resonance (NMR) microscopy, particle-induced X-ray emission tomography (PIXE-T), photoluminescence volumetric imaging (PVI) and synchrotron X-ray computed microtomography (CMT).

3D mapping using X-ray computed tomography (CT) is conducted by measuring the spatial distribution of attenuated intensity values due to absorption and scattering of the primary beam as it passes through an object (Selomulya et al., 2005). The standard X-ray CT method is normally conducted with medical or industrial X-ray sources with a typical resolution in the 100 to 1,000 μm range (Werth et al., 2010). The current research work was completed using synchrotron X-ray radiation and will be discussed in greater detail in the next section.

PVI has been used for visualization and quantification in multiphase porous media. In Montemagno and Grey's (1996) research, this imaging technique used a transparent, multiphase porous media system made of quartz sand and two immiscible fluids matched to the optical refractive index of fused silica (Montemagno et al., 1996). The fluids were then doped with fluorophores and laser light was used to reveal the porous media structure. The illumination was recorded by a charge-coupled device (CCD) camera and the images were combined to generate a 3D data set that allowed for a quantitative study within the porous medium. The sample volume was limited to about 125 mm^3 , with a resolution around at 1 μm , although a typical resolution of 10 μm is more common (Montemagno et al., 1996).

NMR microscopy is a non-invasive method for the characterization of porous systems, and allows visualization of the sample cross sections. In a particular study completed by Selomulya, 3D images were generated via the 2D double spin-echo pulse (Selomulya et al., 2005). The 3D result was a data set composed of sequentially arranged slice images of the entire sample which was used to characterize the material properties. The range for the slice thickness is 37-48 μm (Pauli et al., 1996).

SEM produces images when a focused electron beam interacts with the object and then the object re-emits energy. This energy is then gathered to provide information, such as the object topography. The resolution for 2D mapping by electron microscopy is around 5 microns, however, it typically requires high vacuum or freeze-drying (Bogner et al., 2007; Selomulya et al., 2005).

ESEM is similar to SEM except in ESEM you can work without a required high vacuum. This allows the observation of liquid-containing samples without any special preparation or metal coating (Combes et al., 1998).

The combination of STIM and tomography allows one to determine the three-dimensional constitution of microscopic samples. STIM-T provides cross-sectional views of the variations of density within the specimen in a non-destructive way (Moretto et al., 2001). STIM and particle-induced X-ray emission (PIXE) tomography work by rotating the specimen and bombarding it with electrons for STIM-T and protons for PIXE tomography. "STIM-T is based on the assumption that the slowing down of the particle crossing the sample is directly related to the areal density of the material (Michelet and Moretto, 1999)." The reconstruction algorithm is called the filtered back-projection and is used for low-noise data. The 3D reconstruction for PIXE data is more complex. The decrease in X-ray yields with the slowing down of the incident ion must be taken into consideration by computing an effective attenuation factor (Michelet and Moretto, 1999). "The spatial resolution can reach up to 1–2 mm, but both methods still necessitate freeze-drying and have fairly slow acquisition rates that are in terms of hours rather than minutes (Michelet and Moretto, 1999)."

FIB-SEM uses a focused ion beam for cutting thin slices combined with a scanning electron microscope for the high resolution imaging. The FIB provides a flat surface for high magnification imaging (Loucks et al., 2009). The downsides of using this method are that sample preparation artifacts can be hard to distinguish from the real pore space and high resolution results in a narrow field of view. Generally, due to finite computer memory constraints, higher resolution samples mean smaller sample sizes.

1.2.2 High Resolution Imaging using the Synchrotron

In the work presented, synchrotron X-ray Computed Microtomography (CMT) techniques were used to produce three-dimensional images with micron resolution of reservoir rocks taken from drill cores in the Weyburn oil field.

An image of the ESRF synchrotron in Grenoble, France is shown in Figure 1.2.



Figure 1.2 Image of the European Synchrotron Radiation Facility (ESRF) in Grenoble, France. (ESRF / P. Ginter, 2012)

Synchrotron X-rays are formed by decelerating electrons that follow a curved path in a magnetic field. Synchrotron radiation has several advantages over traditional X-ray sources including high intensity (number of photons per second), a high degree of collimation (source divergence leads to image blur) and tuneability of the photon energy (optimal x-ray energy can be selected for imaging) (Kinney et al., 1992). The highly collimated, parallel synchrotron x-ray beam simplifies the CMT reconstruction process and allows subtle differences in x-ray attenuation in comparison to a typical non-synchrotron x-ray (Glemser, 2007).

The advantage of using a monochromatic X-ray source, as used with the synchrotron x-rays in this study, is the elimination of image artifacts from beam hardening. Beam hardening is a result of higher attenuations because of a preferential absorption of low energy photons (Ruffino et al., 2003). Beam hardening effects seen on conventional, non-synchrotron CMT images, are observed as white noise especially surrounding the rock boundaries on CMT images (Glemser, 2007).

The high resolution, three-dimensional images produced were based on changes of the X-ray attenuation within the sample. The resulting grayscale image is a map of the linear attenuation coefficient (LAC), which was used to isolate the pore space by Glemser (2007). A schematic of the CMT imaging apparatus is shown in Figure 1.3.

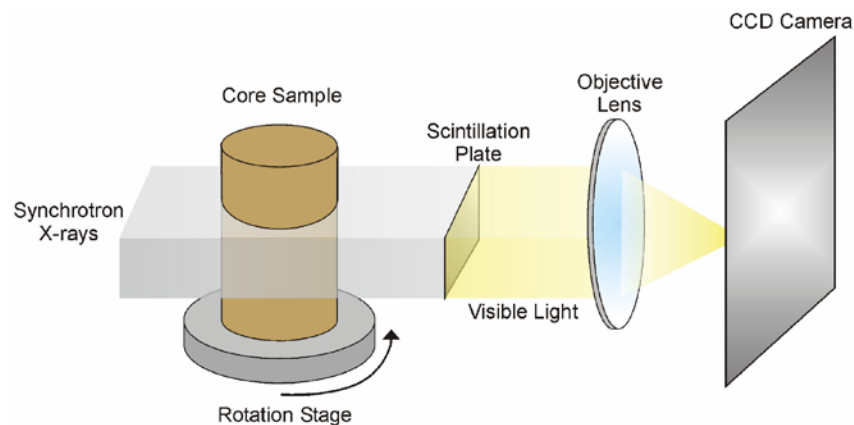


Figure 1.3 Schematic of the CMT apparatus (from Glemser, 2007)

The X-rays are first sent through the core sample, where the scintillation plate converts the X-rays into visible light. The visible light is then recorded by the CCD camera. The images were captured after rotating the sample 180 degrees. The CCD camera recorded the data as a series of 1800 radiographs. The 2D projections were reconstructed to produce a single 2D image, or slice, of the rock core using the filtered back projection algorithm. The 2D slices can be stacked together to produce a 3D image. The resulting image is 8 bit, ranging from 0 (black) to 255 (white).

1.3 Rock Core Sample Used

The cores used originated about 12 km south of Weyburn in Townships 5 to 7 and Ranges 11 to 14 W2M (Glemser, 2007; Wegelin, 1984). Six sections of Midale Carbonate core were extracted from the drill cores (five wells) previously recovered from the Weyburn Oilfield. Three of the samples were taken from the Marly unit and three from the Vuggy unit. The representative lithological unit, Unique Well Identifier (UWI) location, sample depth and CMT resolution is displayed in Table 1.2. The UWI location references the section, township, range and meridian.

Table 1.2 Core samples within the Weyburn Oilfield that were used in previous research. The representative lithological unit, well location, sample depth and CMT resolution is displayed (from Glemser 2007).

Sample	Unit	Unique Well Identifier (UWI)	Depth (m)	CMT Resolution (μm)
ID-02-40	Vuggy (V2)	14-11-6-14W2	1426	10
KD-03-23	Vuggy (V4)	12-19-6-13W2	1408	10
ID-02-19	Vuggy (N/A)	12-26-6-14W2	N/A	7.46
KD-11-03	Marly (M3)	8-20-6-13W2	1394	7.46
KD-18-03	Marly (M0)	12-19-6-13W2	1391	10 and 0.78
MB	Marly (N/A)	6-8-6-13W2	1446	7.46

Remarks: N/A - Information not available

The corresponding images of the reservoir rock cores taken from the Weyburn Oilfield are shown in Figure 1.4.

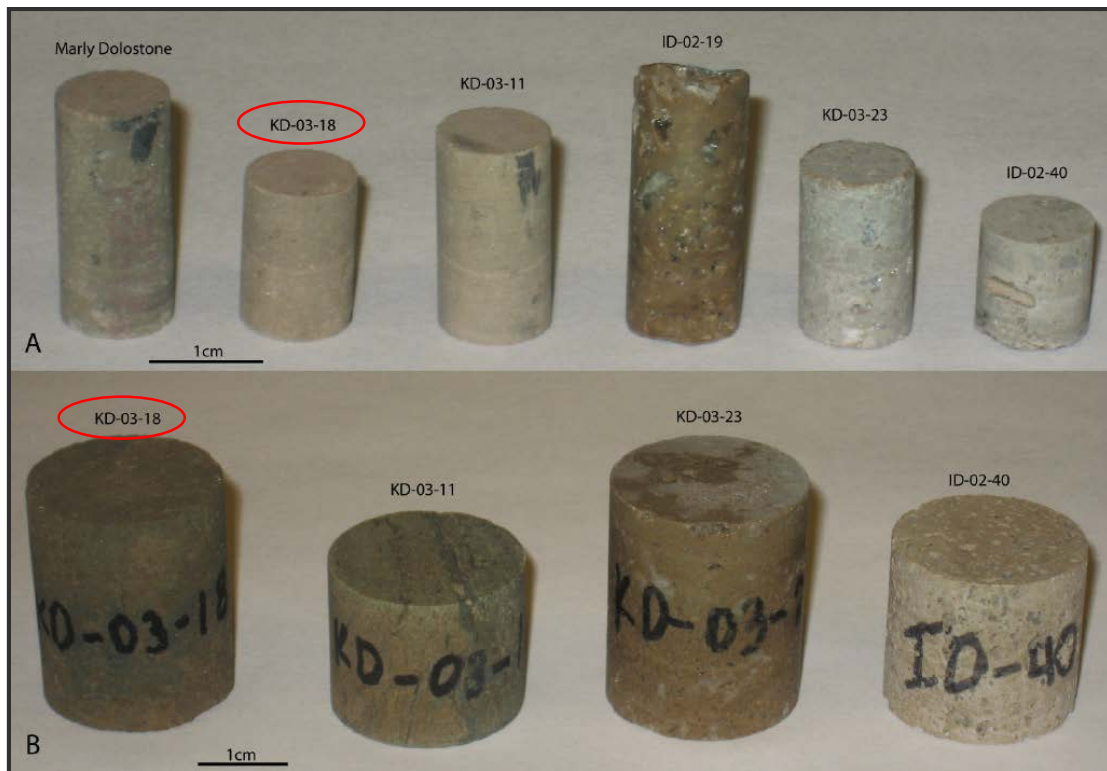


Figure 1.4 Sample cores taken from the Weyburn oil field. Thesis work focused on the KD-18-03 Marly core sample, as circled in red. (A) Cores used in CMT analysis. (B) Larger diameter cores used in petrophysical laboratory measurements. KD 03-18 was previously studied using CMT, petrophysical laboratory measurements and mineralogical analysis (from Glemser 2007).

Figure 1.4 A (KD-18-03), as shown in the top row, was used for CMT analysis. Figure 1.4 B (KD-18-03), as shown in the bottom row, was used for petrophysical laboratory measurements as completed during Chad Glemser's M.Sc. thesis project (Glemser, 2007). The Figure 1.4 A is a smaller sub-volume of the same rock core as shown in Figure 1.4 B. Weyburn reservoir is relatively heterogeneous as can be observed by the color changes and varying surface textures.

My research focuses on the Midale Marly (M0) KD-18-03 core sample which was used for permeability measurements then later modeled with CMT resolutions of 10 μm and 0.78 μm (Glemser, 2007).

Figure 1.5 shows a rock core sample with similar physical dimensions to the Midale Marly (M0) KD-18-03 core. The large diameter core, shown in Figure 1.5 A, was used for conventional petrophysical analysis. The smaller diameter core, shown in Figure 1.5 B, was used for 10 μm resolution CMT analysis and the smallest diameter core, shown in Figure 1.5 C, was used for 0.78 μm resolution CMT analysis. The isolated subsample from within the 0.78 μm resolution core, shown in Figure 1.5 D, was the approximate subsample size shown in Figure 1.1 A. A smaller region inside of this subsample was selected for my numerical calculations.



Figure 1.5 Sample cores with similar dimensions to KD-18-03. (A) Large diameter core used in petrophysical laboratory measurements. (B) Core used in 10 μm CMT analysis. (C) Hole that was drilled to obtain the sample D. (D) Representative region of the core region used for 0.78 μm CMT based core analysis. The reference object is a Canadian dollar which has a diameter of 26.5 mm (Royal Canadian Mint, 2012).

1.3.1 Estimating Porosity, Permeability, Formation Factor and Cementation Exponent from Pore Scale Geometries (from Glemser, 2007)

The two main reservoir layers in the Midale beds are in the Marly zone, a low permeability chalky dolomite overlaying the Vuggy zone, a highly fractured and permeable limestone. (Wilson et al., 2004). Table 1.3 refers to the porosity and permeability in the Weyburn Oilfield for both Vuggy and Marly rock structures.

Table 1.3 Porosity and permeability in the Weyburn Oilfield (Churcher et al., 1994; Glemser, 2007).

	Marly Dolostones	Vuggy Shoal	Vuggy Intershoal
Rock Texture	Mudstone - Wackestone	Packstone - Grainstone	Mudstone - Packstone
Porosity Types	Intercrystalline Vuggy Moldic	Vuggy Moldic Intercrystalline Fenestral	Vuggy Intercrystalline
% Porosity (Average)	16-38 (26)	8-21 (15)	2-15 (10)
Permeability (mD) (Average)	1-150 (10)	0.3-500 (50)	0.01-20 (3)
Thickness (m) (Average)	0.1-9.8 (4.3)	0.1-18.6 (6)	

The porosity, permeability and electrical resistivity for the Midale Marly KD-18-03 are summarized in Table 1.4 as completed by Glemser (Glemser, 2007).

Table 1.4 Porosity, permeability and resistivity for the KD-03-18 sample using the permeability core, 10 μm and 0.78 μm resolution CMT core (Glemser, 2007).

		Permeability Core	CMT Core (10 μm resolution)	CMT Core (0.78 μm resolution)
Porosity (%)	CMT	-	0.26	32.0
	Water Saturation	31.7	39.4	-
	Mercury Porosimetry	34.5	-	-
Measured Permeability (mD)	Gas	16.9	-	-
	Liquid	7.7	-	-
Simulated Katz-Thompson Permeability (mD)	Predicted from CMT	-	372	7.73
	Predicted from Mercury Injection	-	6.91	-
Electrical Resistivity	Formation Factor (F)	11.71	-	-
	Cementation Exponent (m)	1.87	-	-

As referenced from Glemser, 2007

All of the data measured and computed in Table 1.4 was acquired by Glemser (2007). Glemser's results will be used for comparison with my results for the same KD-18-03 Midale Marly rock sample using the 0.78 μm resolution dataset.

Using CMT greyscale data, the porosity was calculated using pore extraction software by thresholding the pore space region for both the 10 μm and 0.78 μm resolution datasets. The difference between the porosity results for the 10 μm and 0.78 μm CMT images indicate that a significant portion of the Midale Marly pore space exists below the 10 μm resolution threshold and above the 0.78 μm resolution threshold (Glemser, 2007). The effective porosity determination for water saturation was completed using the permeability core and the 10 μm resolution CMT core by Glemser (2007) using the following formula.

$$\phi = \frac{M_{wet} - M_{dry}}{\rho_{H_2O} \times V_{sample}} \quad (1.1)$$

where M_{wet} , M_{dry} , ρ_{H_2O} and V_{sample} represent the measured mass for the wet core, measured mass for dry core, density of water, and sample volume.

Porosity was also determined by Glemser (2007) using a Ruska Mercury Injection Permeameter following standard procedures (ASTM D4404-84). The porosity by water saturation and mercury porosimetry is roughly equivalent to the porosity calculated using the 0.78 μm CMT data.

Gas permeability measurements were completed on the permeability cores during Glemser's thesis work in 2007. The gas permeability was measured using a Ruska Gas Permeameter. The cylindrical core sample was injected with compressed nitrogen gas to determine the gas permeability of the core. The permeability was calculated at three different pressure drops. Slippage effects result in artificially high permeabilities and were accounted for by extrapolating the permeability values to zero pressure (Glemser, 2007). The gas permeability was then calculated using the formula:

$$k = \frac{\mu QL}{AP} \quad (1.2)$$

where μ , Q , L , A , and P represent the viscosity of the test fluid, flow rate, length of the sample, cross-sectional area of the sample and pressure drop.

The liquid permeability measurements were performed using a Ruska Liquid Permeameter. First, the core was saturated to eliminate the presence of air-water interfaces. The sample was immersed in a synthetic brine for 7 days to ensure saturation. A pressure of 202.7 kPa was applied to force the fluid through the core (Glemser, 2007). The time to deliver a 5 ml burette of synthetic brine was recorded. The average flow rate was calculated by dividing the volume of the fluid in the burette by the time required to empty to burette. Equation 1.2 was then used to calculate the permeability.

If the pore geometry and electrical formation factor are known, the estimated permeability can be calculated using the Katz-Thompson equation:

$$k = -\frac{l_c^2}{226F} \quad (1.3)$$

where l_c is the critical pore diameter (in μm), F is the formation factor calculated from the electrical resistivity and $\frac{1}{226}$ is a constant dependent on the fractal nature of pore space within sedimentary rocks.

The critical pore diameter is equal to the local pore diameter assumed to be responsible for dictating fluid percolation across the rock core (Glemser, 2007). Using CMT data, Glemser found the pore-throat diameters directly from the image analysis. It can also be determined from a mercury injection capillary pressure curve porosimetry (Glemser, 2007).

The electrical resistivity measurements are used along with empirical relationships between rock resistivity and porosity to help us understand macroscopic properties of the rock (Glemser, 2007). The formation resistivity factor is defined as:

$$F = \frac{\rho_o}{\rho_w} \quad (1.4)$$

where ρ_o and ρ_w represent the resistivity of the brine saturated rock core and resistivity of the brine.

The resistance of the sample can be calculated using:

$$R = \frac{V}{I} \quad (1.5)$$

where V is the voltage drop across the sample and I is the current.

The resistivity of the sample can be calculated using:

$$\rho = R \frac{A}{L} \quad (1.6)$$

where R, A and L are the resistance, area and length.

Archie's Law is an empirical approximation that relates the formation resistivity factor, porosity and cementation exponent together (Archie, 1942). Archie's Law gives:

$$F = a \cdot \phi^{-m} \quad (1.7)$$

where a is usually close to 1, and ϕ is the porosity and m is the cementation exponent.

This cementation exponent describes the distribution of pores and generally increases in value with increasing cementation (Glemser, 2007). Glemser obtained the cementation exponent by cross-plotting direct measurements of porosity against the formation resistivity factor. It was also assumed that $a=1$.

The cementation exponent can be determined from equation 1.7 to be:

$$m = \frac{\log a - \log F}{\log \phi} \quad (1.8)$$

where F is the formation factor and ϕ is the porosity. The value of m is typically close to 2 for carbonate rocks (Doveton, 1999).

1.4 Weyburn Oilfield Background

Figure 1.6 A shows the location of the Weyburn and Midale Oil Fields in southeast Saskatchewan, Canada near the United States border. The approximate location of the Williston basin extends into Saskatchewan and Manitoba (Canada) and Montana, North Dakota and South Dakota (United States). Figure 1.6 B shows the Weyburn oilfield study area located beside the Midale oilfield. Cenovus Energy is the majority owner and operator of the Weyburn Unit, and Apache Canada is the operator of the Midale Unit. Figure 1.6 C shows the drilling locations for the Marly and Vuggy core samples.

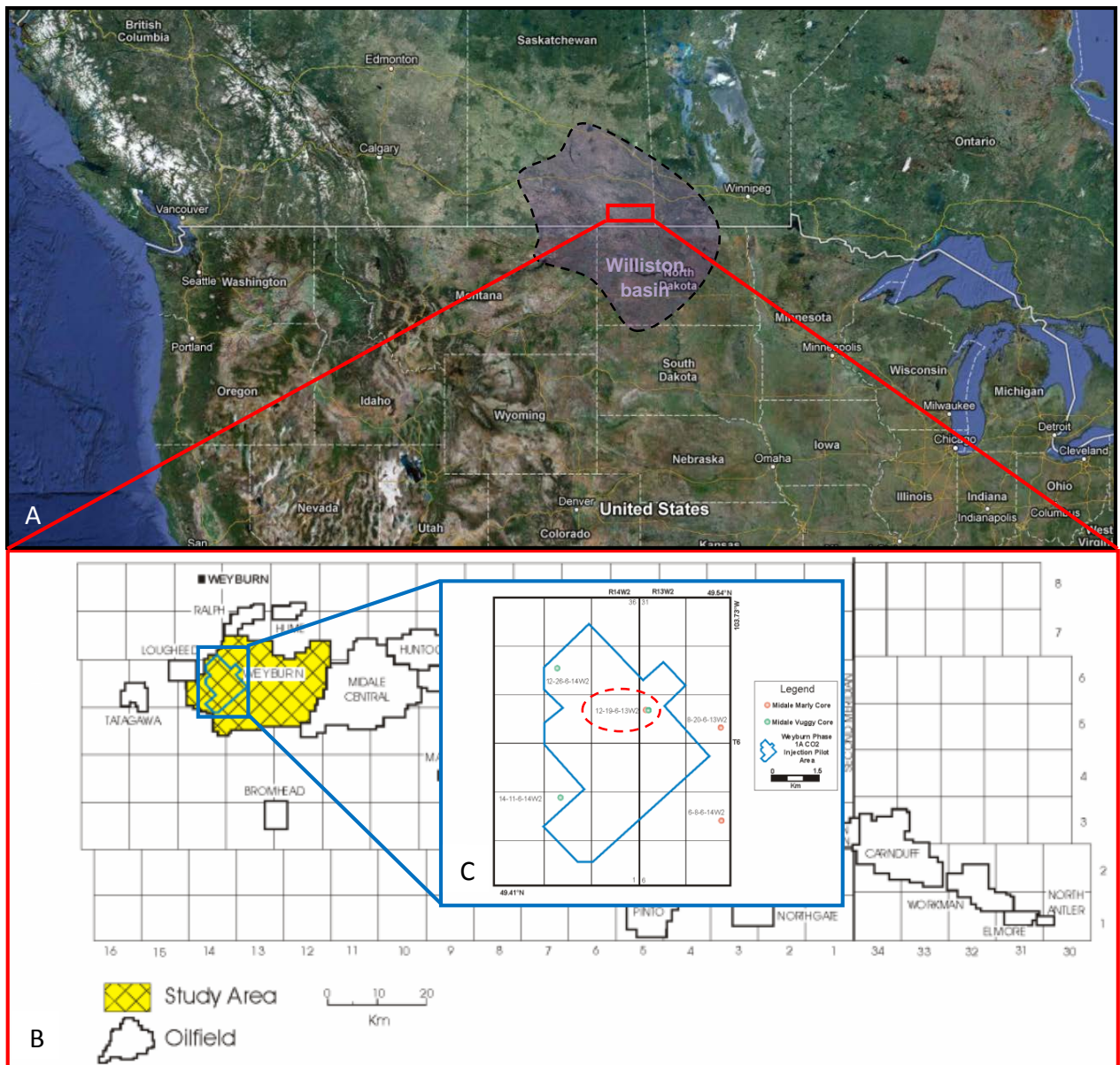


Figure 1.6 (A) Location of Weyburn and Midale Oil Fields located in southeast Saskatchewan, Canada near the Unites States border (screenshot from Google Maps). The length of the oilfield is about 180 km horizontally. The approximate location of the Williston basin is shown as extending into Saskatchewan and Manitoba (Canada) and Montana, North Dakota and South Dakota (United States). (B) The Weyburn oilfield study area located immediately west of the Midale oilfield. Cenovus Energy is the majority owner and operator of the Weyburn Unit, and Apache Canada is the operator of the Midale Unit. (C) Drilling locations for the Marly and Vuggy core samples. The Midale Marly (MO) unit called KD-18-03 is identified as the Unique Well Identifier (UWI) format 12-19-6-13-W2 (B and C after Glemser, 2007).

CO₂ injection began in the fall of 2000 with the intention of reversing the declining production typically associated with a maturing oil pool. After 10 years of CO₂ injection, oil production increased by 60% and about 155 million barrels of incremental oil are expected to be recovered that will extend the life of the field by more than 30 years. Similarly, in the adjacent Midale Oil Field, full field CO₂ injection began by Apache Canada in September 2005 with a forecast of 30 to 40 years of extended life and 60 million barrels of incremental production (Whittaker et al., 2011).

1.5 Oil Recovery Factors

Oil recovery is partially dependent on macroscopic petro-physical properties of the reservoir rock. Oil recovery processes are historically defined as primary, secondary and tertiary. Primary processes generally produce oil by using natural energy and are often the result of excess reservoir pressure though pumping is often required to facilitate the flow of oil to surface. Natural energy sources include natural water or gas drive (Al-Mjeni et al., 2011). Typical oil recovery by this primary mechanism is 15-20% (Simon, 1981).

Secondary processes assist oil to flow by providing energy via either natural gas or water injection. The Weyburn oilfield is one example of wells using water injection, typically referred to as water flooding (Whittaker et al., 2011). Typical oil recovery by the secondary recovery mechanism is 20-50% (Simon, 1981).

Tertiary processes typically include everything besides primary and secondary processes, such as the CO₂ injection process now used in the Weyburn oilfield. With advances in reservoir processes, the distinction between primary, secondary and tertiary processes have been blurred. For example, engineers sometimes found that it is better to use waterflooding before pressure decline, or that a tertiary method should be used in place of a waterflood, or that potential recovery by a tertiary method might be lost due to reservoir damage from earlier activities (Al-Mjeni et al., 2011). Overall, the processes have lost the original sense of chronological order.

Secondary and tertiary processes are typically referred to as Enhanced Oil Recovery (EOR) (Simon, 1981). The waterflood method is not typically considered as an EOR method unless it

is combined with another flooding method. EOR methods include gasflooding (immiscible and miscible), thermal techniques and chemical flooding as summarized in Table 1.5.

Table 1.5 Enhanced Oil Recovery Methods (from Al-Mjeni et al.,2011)

EOR Method		Pressure Support	Sweep Improvement	IFT Reduction	Wettability Alteration	Viscosity Reduction	Oil Swelling	Hydrocarbon Single Phase	Compositional Change ¹	Incremental Recovery Factor
Waterflood	Waterflood									Base case ²
	Engineered water									Low
Gasflood: immiscible	Hydrocarbon									Moderate
	CO ₂									High
	Nitrogen or flue gas							3	3	Moderate
Gasflood: miscible	Hydrocarbon								4	High
	Hydrocarbon WAG								4	Very high
	CO ₂									High
	CO ₂ WAG									Highest
Thermal	Steam									High
	High-pressure air									High
Chemical	Polymer									Low
	Surfactant									Moderate
	ASP									High

IFT = interfacial tension
WAG = water-alternating-gas
ASP = alkali-surfactant-polymer

1. Change of composition of liquid hydrocarbon.
2. Waterflooding provides the base case for comparison of other methods.
3. Oil stripping occurs as miscibility develops.
4. Condensing and vaporizing exchange.

The EOR Methods mentioned in Table 1.5 are briefly discussed below.

CO₂ injection is typically combined with waterflood methods. In the Weyburn oilfield alone, there are more than 100 wells that inject CO₂ during different phases of the EOR operation and most of the wells alternate injecting CO₂ and water while there are at least 17 CO₂ only injectors (Al-Mjeni et al., 2011).

Gasflood EOR injection can be either under immiscible or miscible conditions based on the pressure, temperature and composition of the gas. In an immiscible flood, gas and oil remain in distinct phases. The gas invades the rock as a non-wetting phase and displaces the oil from the largest pores first (Al-Mjeni et al., 2011). In a miscible flood, gas and oil form one phase. The mixing typically causes the oil volume to swell while lowering the interfacial tension between the water and oil (Al-Mjeni et al., 2011). Gasflood CO₂ injection into the reservoir results in several mechanisms that promote oil recovery. CO₂ dissolves in the oil, swells it, reduces its viscosity and provides a low CO₂-oil interfacial tension so that the CO₂ can enter smaller pores containing oil (Simon, 1981).

Steam can be used to recover dense, viscous oil. As steam condenses in the reservoir, the oil is heated and the oil viscosity is reduced (Simon, 1981). Thermal EOR uses steam injection that is forced into the ground. After a soaking period, the condensing steam heats the formation and

reduces the oil viscosity. Oil production follows and then the process can either be repeated or the well may also be converted to an injection well in a pattern flood (Al-Mjeni et al., 2011).

Injecting surface-active chemicals dissolved in water and/or oil lowers the interfacial tension between the solution and reservoir oil, allowing the solution to enter and displace oil from more pores (Simon, 1981). Using the chemical EOR methods, a brine preflush stage is sometimes used to change the salinity or rock/fluid properties. An alkali-surfactant solution then mixes with the oil and changes its properties to mobilize additional oil. The polymer solution is used to improve the mobility differential between the oil and the injected fluids. The freshwater buffer is then used to optimize the recovery of the chemicals, followed by a water drive (Al-Mjeni et al., 2011).

Understanding porous media flow and transport is of central importance in the oil recovery processes and in the geological sequestration of CO₂ (Wildenschild et al., 2012). The pore scale, at which individual grains and fluid interfaces can be resolved using x-ray microtomography, is the scale at which many physical phenomena are rooted. It is repeatedly shown that larger-scale processes are often governed by these small scale phenomena (Wildenschild et al., 2012). Pore scale modeling allows a direct insight into oilfield recovery processes and can be used as a screening tool that can be used to indicate recovery trends and act as a reservoir management guide (Blunt et al., 2012).

1.6 Numerical Methods

Numerical techniques for finding approximate solutions to the Navier-Stokes and Laplace partial differential equations (PDEs) include the finite difference method (FDM), finite element method (FEM), finite volume method (FVM), spectral method (SM) and Lattice Boltzmann Methods (LBM).

FEM is a powerful tool for analysis. FEM methods are typically used in software packages that include mesh generation algorithms that make setting up mesh areas easy to implement without being an expert in this area (Rypl et al., 2006). As the pore space inside the pore-scale geometry is complicated, so is the resulting mesh. FEM excels at handling complicated mesh structures

due to a changing mesh grid. The FEM method packages are typically readily available for purchase, whereas other numerical techniques are not as readily available.

The FDM is typically restricted to handle simple mesh shapes, therefore making it difficult to import complex geometry. Additionally, FDM is not as readily available as other third party software packages, such as those using FEM. The benefit of the FDM is it is relatively easy to implement without using an existing software package.

Spectral Methods (SM's) are referred to as global methods and solutions to the PDE's converge exponentially, therefore, accuracy is typically higher than FEM or FDM. SM computations not only depend on neighboring information, but on the entire domain. The grid size can be reduced, therefore saving computer memory that is typically used for mesh generation. The SM uses Fourier basis functions, but can also be made using other orthogonal basis functions. The downside of SM is that they are not good for complicated geometry and don't handle variable coefficients very well.

The FVM is similar to the FEM and FDM, where values are calculated on the meshed geometry. The term 'finite volume' refers to the volume surrounding each node on the mesh. Volume integrals in the PDE, that contain a divergence term, are converted to surface integrals using the divergence theorem. These terms are then evaluated as fluxes at the surfaces of each finite volume. The fluxes on the boundary are then discretized with respect to the unknowns (R. Eymard et al., 2006). An advantage of using the FVM is that it can be easily formulated to allow for unstructured meshes, however, in some cases, it may be difficult to design schemes which provide enough precision (R. Eymard et al., 2006). The FEM can be more precise than the FVM when using higher order polynomials (R. Eymard et al., 2006).

As far as first principle approaches are concerned, Lattice Boltzmann Methods (LBM) have gained popularity since their introduction in the early 1990s due to its ability to deal with complex 3D geometries and complex multiphysics (Piller et al., 2009). Unlike conventional Navier-Stokes solvers, the LBM does not approximate the equations directly but simulates the fluid behavior on an intermediate (mesoscopic) scale and determines pressure and velocity as moments of the particle density (Succi, 2001). The success of the LBM lies in that the basic single-phase simulation of a voxel based lattice is formed by no more than 15 lines of high-

level programming statements, the basic steps (fluid particle propagation, fluid collision) are amenable to parallelization, and the periodic boundary condition and bounce back conditions describing fluid-solid grain interactions are easy to implement (Piller et al., 2009).

We selected to use the software package, called COMSOL Multiphysics, for this research because it was readily available and because of its flexibility (i.e., it can be used to model various user-selected physical processes). One of the major advantages of using COMSOL Multiphysics is that it is commercially available and can be used to investigate physical properties that cannot be obtained using laboratory methods. We were also familiar with using the software from previous work. COMSOL uses the FEM for solving various partial differential equations, including the Navier-Stokes equations and Laplace's equation.

2 PORE EXTRACTION METHODOLOGY

2.1 Introduction

The CMT data was thresholded to extract the connected pore space from the rock matrix using Avizo. A surface representing the boundary between the pore space and rock matrix could then be sent to COMSOL Multiphysics. COMSOL was then used to mesh the pore volume and solve the Navier-Stokes equations for the fluid flow and Laplace's equation for the electrical current density. The computer specifications and pore extraction methodology used in the workflow are discussed below.

2.2 Computer Specifications

It was realized early in the research stage that significant computing power was going to be required to successfully isolate the pore space and solve the Navier-Stokes equations inside the pore space. Therefore, a more powerful, custom computer was built to handle the anticipated computations.

A 64-bit operating system is highly recommended by both COMSOL and Avizo. COMSOL recommends 4-8 GB physical RAM per core of the computer and a dual 6-core processor with 96 GB of RAM is recommended for larger models (COMSOL Multiphysics, 2012b). Avizo recommends a GPU that is used during image segmentation, among other calculations (Visualization Sciences Group, 2012).

Overall the RAM and video card were the most important pieces of the computer architecture. The RAM was the limiting factor for inserting larger volumes of data into both COMSOL and Avizo. The meshing phase and solution of the PDE's in COMSOL was also heavily dependent on the amount of system RAM installed. The video card was also a limiting factor for viewing the data. The RAM installed in the video card was also important as the newer video cards render the 3D geometry, and associated mesh, several times faster than older video cards. For example, the previous generation of computer gaming video card took 15 minutes to rotate the 3D image. The newer video card rotated the same image multiple times per second.

Computer specification recommendations are available on-line from both COMSOL and Avizo. As it may be helpful for future work, the computer specifications used in this work are included in Appendix C.

2.3 Importing Synchrotron core data into Avizo Fire

A method to extract the KD-18-03 pore space and calculate the associated permeability was pursued. The extraction of the digital 3D pore spaces was carried out using a computer program called Avizo Fire. Avizo Fire is the standard Avizo with the Visilog 6 software built into the program to include advanced pore extraction features.

The optimal pore extraction methodology considered all the capabilities of Avizo Fire including thresholding, filtering algorithms, binarization of the data, and utilization of various digital filters. Avizo Fire 6 was used for extracting the pore space and then COMSOL Multiphysics 4.3 was used to solve the full 3D Navier-Stokes equations in the pore space in order to calculate the sub-sample macroscopic properties. The suggested methodology for the pore extraction is given in the following sections.

2.4 Avizo Fire Workflow

The following workflow was used to import the data into Avizo Fire and convert this data into a form that was used by COMSOL Multiphysics.

- import data
- crop data
- threshold and binarize data
- filter data
- determine voxel connections
- generate surface
- export surface

2.5 Import Data

The CMT reconstruction phase generated a series of 2D slices which combined together to build a 3D image. The resulting image is 8 bit, ranging from 0 (black) to 255 (white). The reconstructed 3D images were recorded in sections to reduce file size (Glemser, 2007). KD-18-03 has eight reconstructed images with each image being about 1 gigabyte in size. To view the 8 bit greyscale 3D image, 2D isosections have been extracted as shown in Figure 2.1. They were recombined together with each of the eight sections vertically separated by 39 μm (50 voxels) to help display the image sections. The CMT image resolution is 0.78 μm per voxel, where a voxel is defined as a volumetric pixel. I use the term voxel to indicate the side length of a volume unit.

Figure 2.1 A displays one slice per subsection of the reconstructed image data from KD-18-03. The eight subsections are referred to as subsection 1, at the top, decreasing to subsection 8, at the bottom. Subsection 3 was used for the thesis work as the remaining sections have artifacts, such as ringing, and some missing CMT data. The missing data can be observed in subsection 1 and subsection 5. Subsection 1 has a large area where the image was not recorded. Subsection 5 has the same missing rock information at the edge of the sample. Figure 2.1 B displays a smaller isolated image inside subsection 3. This smaller subsample was isolated so that the pore space extraction process could be completed using the available computer memory without having to downsample the image resolution. The regions isolated in Figure 2.1 B were taken from 500 to 530 (x-direction voxels), 500 to 530 (y-direction voxels) and 0 to 30 (z-direction voxels). The voxels in this subsample have a CMT resolution of 0.78 μm , so the actual scale is 23.4 μm in all directions.

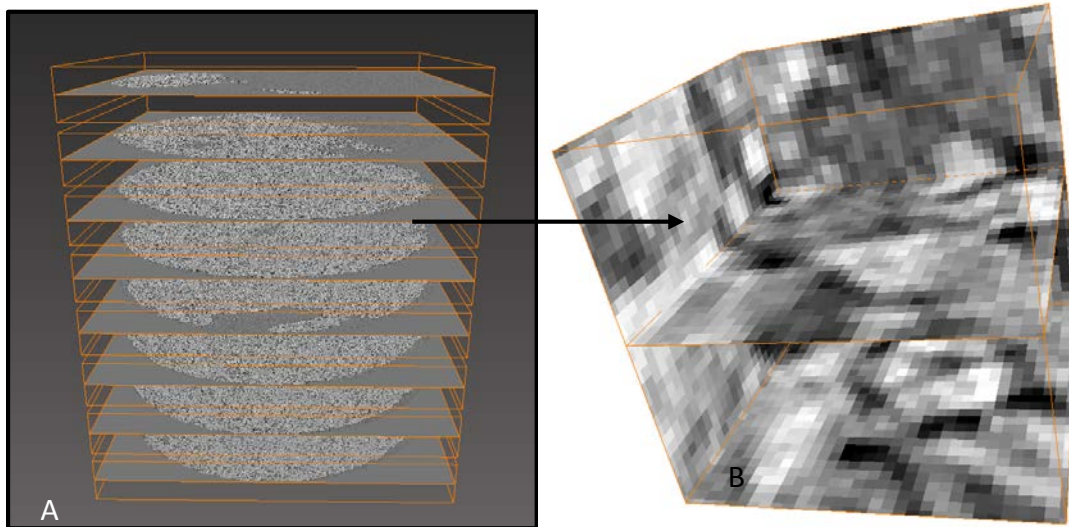


Figure 2.1 (A) Combining the CMT data from KD-18-03 via post-processing in Avizo. The top and bottom section are referred to as subsection 1 and subsection 8 respectively. (B) An isolated 8 bit greyscale image from cropped section is also displayed from subsection 3. The voxels in this subsample have a resolution of $0.78 \mu\text{m}$, so the actual scale of this $30 \times 30 \times 30$ voxel subsample is $23.4 \mu\text{m}$ in all directions.

2.6 Crop Data

Figure 2.2 is shown to demonstrate the process of changing from 3D to 2D for visualization purposes for the subsequent figures. Figure 2.2 A displays a randomly selected 3D section from KD-18-03 (subsection 3). The voxel regions isolated in Figure 2.2 B is the same as shown in Figure 2.1 B.

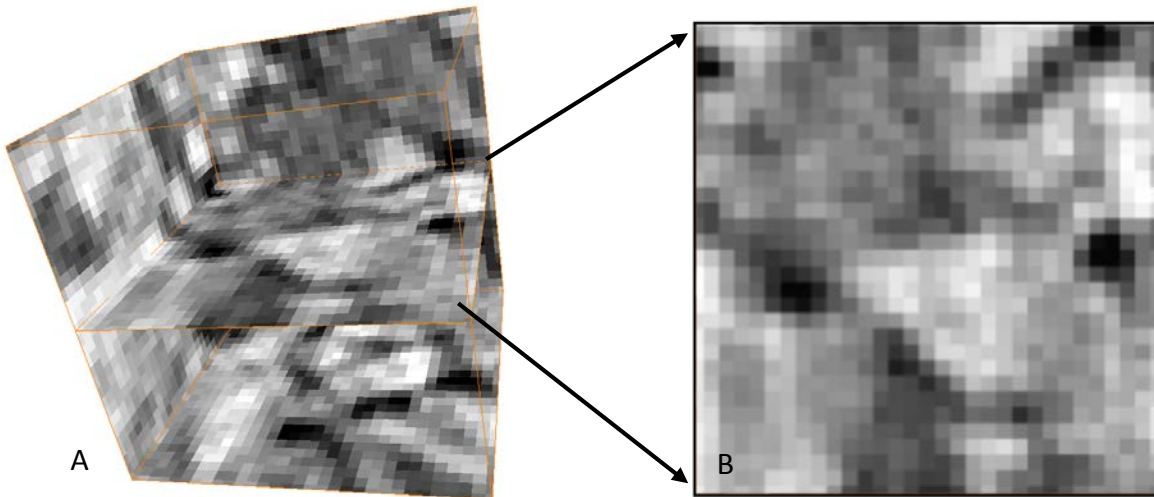


Figure 2.2 (A) Isolated Greyscale 8 bit image from KD-03-18. The 3D figure is 30 x 30 x 30 voxels (23.4 x 23.4 x 23.4 μm). (B) The 2D orthoslice section, as isolated from the 3D image, with dimensions of 30 x 30 voxels (23.4 x 23.4 μm).

2.7 Threshold and Binarize Image

Subjective decisions often need to be made when thresholding data and there can be much variation among experts as to the best choices. The thresholding variation associated with multiple imaging strategies was investigated in the paper called, "Observer-dependent variability of the thresholding step in the quantitative analysis of soil images and X-ray microtomography data" (Baveye et al., 2010). A field soil, a soil thin section and a virtual section through a 3D CT data set were investigated by thirteen experts around the world. The lack of standardization translated into thresholded images that differ substantially. The same images, after thresholding by experts, resulted in a porosity that ranged from 24.02% to 75.50%. Various recommendations to narrow the porosity range are given in the paper. One of these recommendations require the authors to specify the method of thresholding adopted and the sensitivity of the final thresholding value selected. The greater scientific community needs to standardize the thresholding method, however, this will require a significant amount of consultation (Baveye et al., 2010). Alternatively, the porosity obtained by thresholding the CMT data could be compared to the laboratory measured porosity.

There are various strategies that can be used for extracting the pore space. Such strategies typically use filters, enhance image contrast, reduce noise and typically include data binarization (Baveye et al., 2010). Considering the vast number of thresholding strategies available, a single threshold value can be difficult to determine. If the thresholding range is too large, the permeability results may be artificially higher than the correct permeability. The permeability would also be artificially lower for a thresholding range that is too low.

Thresholding values for the pore space and minerals were investigated by Glemser (2007). The KD-18-03 CMT core 8 bit image was visually compared to the thin-section viewed under cross polarized light from the same core. Electron Probe Micro-Analysis (EPMA) was then completed for semi-quantitative analysis on the carbonate thin sections and Backscattered Electron (BSE) imaging was used to resolve mineral composition of the rock matrix. The grey levels from the BSE were then used as a calibration for the minerals and were directly compared to the X-ray attenuation values that were used to extract the pore space from the CMT data. Glemser (2007) found that LAC values from 0-85 represented pore-space where the greyscale is proportional to the linear attenuation coefficient (LAC) (Glemser, 2007).

The porosity results, as given in Table 1.4, show that the porosity of the permeability core, calculated by water saturation is 39.4% and by mercury porosimetry is 34.5%. These values are roughly equivalent to the CMT porosity, 32.0%, calculated by thresholding the pore space of the 0.78 μm CMT data. Given the above methodology and results from Glemser (2007), I am confident that the thresholding values used are reasonable and applicable for isolating the pore space inside the KD-18-03 image data.

A histogram of KD-18-03, as shown in Figure 2.3, appears to have a weakly bimodal distribution with peaks around 60 and 160. The pore space threshold is 85 and is displayed as the red line in Figure 2.3 B.

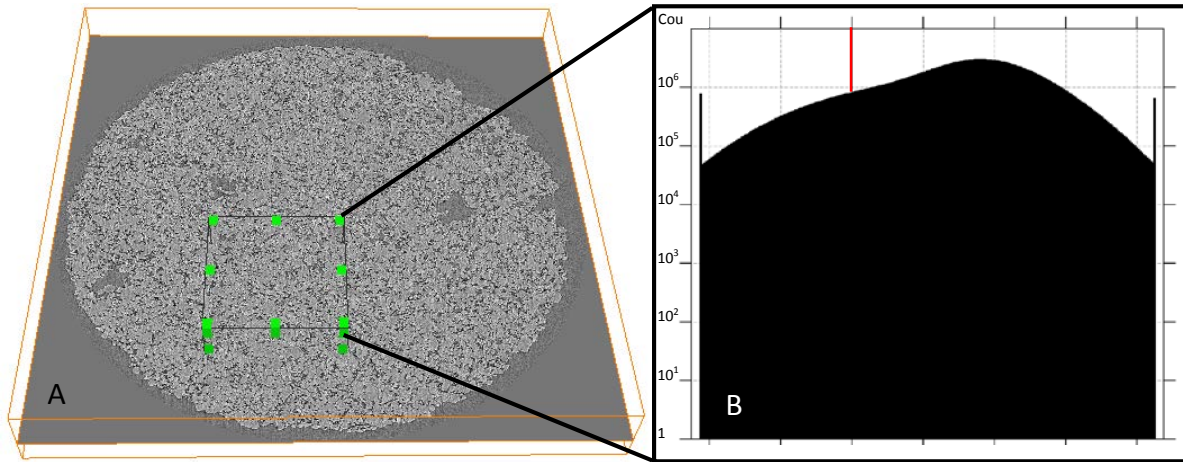


Figure 2.3 (A) The 3D cropped orthoslice section of slice # 160 (out of a total from slice # 0 to slice #255). The 3D cropped index values are 600 to 1099, 1200 to 1699, 0 to 255 in the x,y and z directions respectively. The 3D histogram is represented by 500 x 500 x 8 voxels at 0.78 μm resolution for a real scale resolution of 390 x 390 x 200 μm . (B) Histogram of Greyscale 8 bit image from KD-03-18, subsection 3. The threshold value of 85 is shown on the histogram plot.

Figure 2.4 A illustrates the 8 bit greyscale CMT image without thresholding applied. Figure 2.4 B illustrates the thresholded pore space to a value of 85, out of a possible range of 0 to 255 bits. The thresholded value is shown in red.

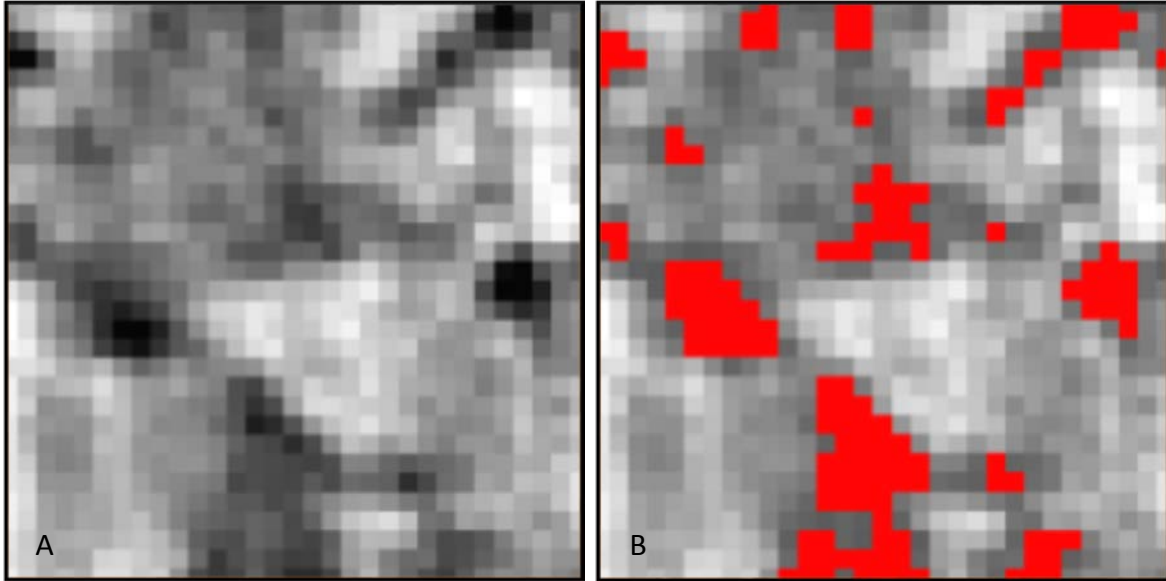


Figure 2.4 (A) 8 bit greyscale image. (B) Thresholded image to 85 where the red voxels are shown that represent the pore space. Both image scales are 30 x 30 voxels (23.4 x 23.4 μm).

The image can now be binarized so the voxels of interest are set to ‘1’ and to ‘0’ for all other voxels (the background). The Quantification-Thresholding package in Avizo Fire thresholds the image and then converts the grey level image into a binary image. Equation 2.1 and Figure 2.5 illustrates how Avizo Fire transforms the image from grey scale to binary.

$$O(n, m) = \begin{cases} 0 & \text{if } \lambda_1 \leq I(n, m) \leq \lambda_2 \\ 1 & \text{if } I(n, m) < \lambda_1 \text{ or } I(n, m) > \lambda_2 \end{cases} \quad (2.1)$$

where λ_1 and λ_2 are the input threshold values between 0 and 255.

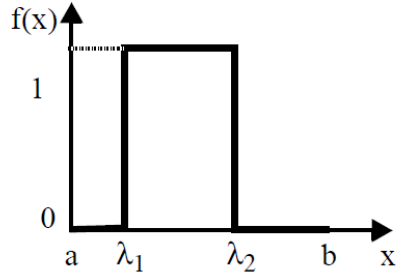


Figure 2.5 Binary Image using Quantification-Thresholding (from Visilog, 2010)

In this case, $\lambda_1 = 0$ and $\lambda_2 = 85$. All pore space is identified as '1' with all other voxels identified as '0'. Figure 2.6 displays the thresholded image and binarized image. The Quantification-Thresholding algorithm, available using Avizo Fire, can be completed by entering the λ_1 and λ_2 parameters directly. This method can also be accomplished without using the Quantification-Thresholding algorithm. Avzio, as a standalone package, has a similar thresholding tool along with a separate binarization tool. Avizo Fire combines these processes. Both results are identical to those shown in Figure 2.6 A-B.

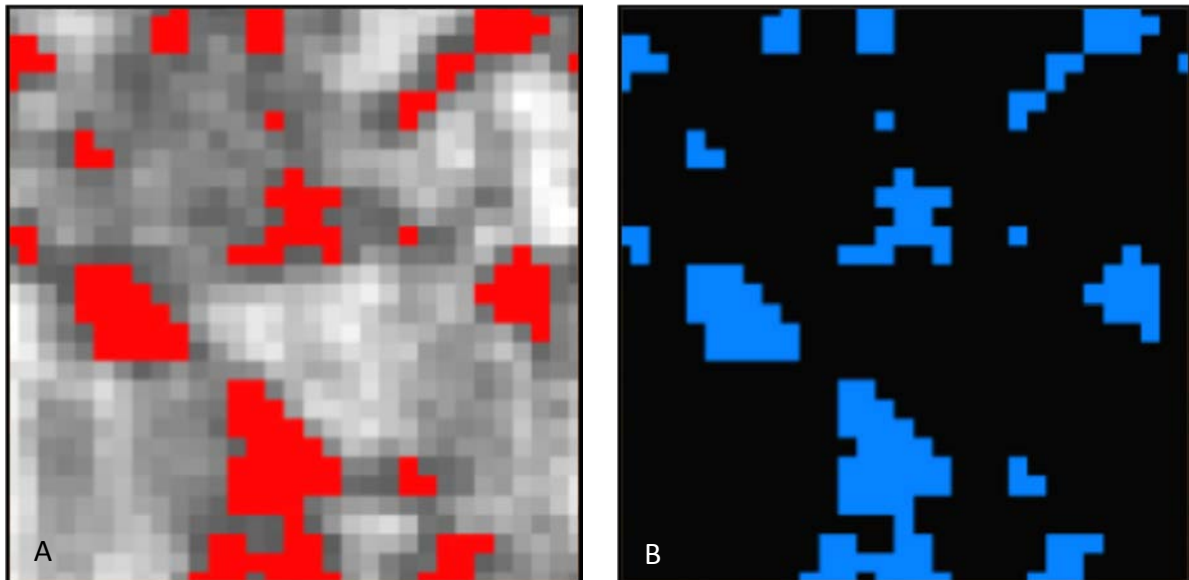


Figure 2.6 (A) Thresholded Image and (B) Binarized Image. Both image scales are 30 x 30 voxels (23.4 x 23.4 μm).

2.8 Skeletonization

After the image was thresholded and binarized, it was useful to check to see if the pore spaces were connected. A quick way to observe connectivity is with the AutoSkeleton module in Avizo Fire. Using a threshold value of 85, the pore space is as shown in Figure 2.7. The pore space thickness corresponds to the tube color variations. The intersections of various connected pore spaces generally have the largest pore throat diameters in this subsample.

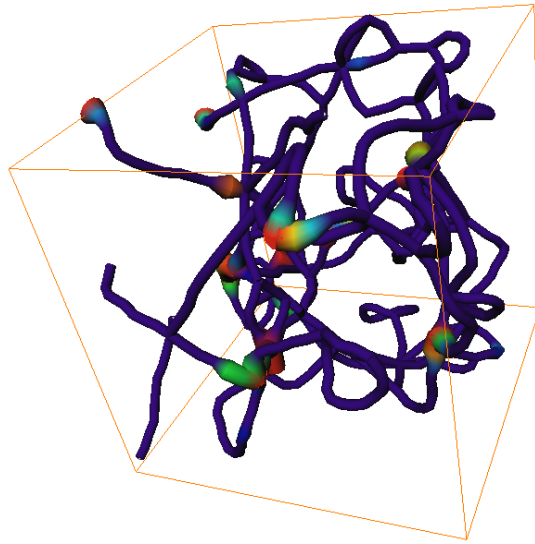


Figure 2.7 Skeletonization of the Binary Image

The AutoSkeleton module worked by extracting the centerline of the pore space from the binarized data. This module only works with data that is first segmented into a label, describing the pore space, or a binarized image of the pore space (Visualization Sciences Group, 2010b). The skeletonization process was also completed without using the built in AutoSkeleton module. The AutoSkeleton module effectively combines several separated modules that had to be executed in sequence. First, the AutoSkeleton calculates a distance map of the binarized image and then performs a thinning of the binarized data, such that a string of connected voxels remains. The voxel skeleton is then converted to a Spatial Graph object. The distance to the nearest boundary (boundary distance map) is stored at every point in the Spatial Graph object as a thickness attribute, which can be used as an estimate of the local thickness (Visualization Sciences Group, 2010a).

The AutoSkeleton Spatial Graph could not be directly exported to run in COMSOL since additional software would be required to first convert the data into a usable import format for COMSOL. The AutoSkeleton also uses approximations, which are not necessarily valid for extracting the pore space. The separate modules described above were completed separately with various model parameters changed to investigate the approximations used in the AutoSkeleton module. As will be shown later, in Figure 2.14, the connected pore space didn't exactly match the pore space due to approximations made both via user input and module algorithms. Figure 2.8 displays the skeletonization of the binarized data, including both the orthoslices of the binarized image and the 8 bit greyscale image.

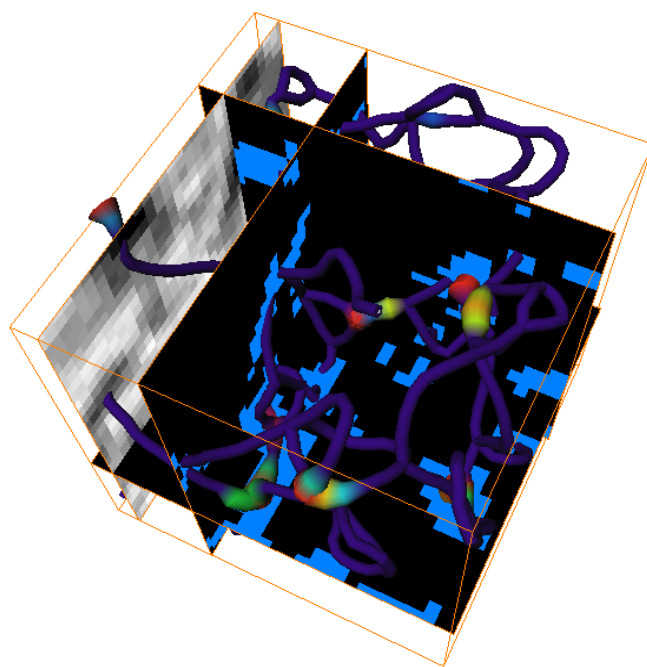


Figure 2.8 Skeleton of Binary Image with Orthoslices of both binary and 8 bit greyscale CMT images.

The AutoSkeleton was still used as a visual tool to estimate the pore space connectivity. This was a time saving strategy used when considering multiple subsamples, as the user doesn't have to proceed with the pore extraction workflow if the pore space is not visibly connected.

2.9 Filter Data

A problem in extracting the pore space was how to estimate the binary image as the input ‘signal’ when it was mixed with noise. One solution is the moving average, where the value of each voxel was replaced by the average of its neighbors. This filter is based on the assumption that short ranged variations result from noise. The filtered output can then be viewed as the main trend of the function, as shown in Figure 2.9. The data shown in Figure 2.9 is not actual data, but is shown to roughly represent how a filtered signal can smooth the noisy initial signal data.

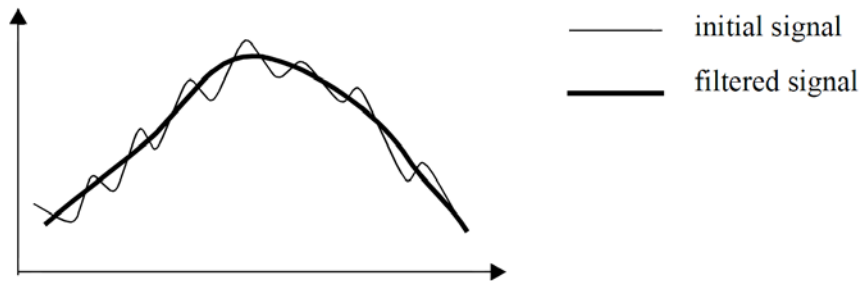


Figure 2.9 Filtering the signal using a moving average (from Visilog, 2010)

The Gaussian filter is a low-pass filter that reduces the contrast and softens the edges of objects in an image. The low-pass filter permits low frequencies to pass but attenuates high frequencies and noise. Overall, this filter reduces contrast and also tends to defocus the image. The 3D Gaussian filter was used to blur the image and get rid of complex geometry and associated artifacts that were found to cause surface generation topography errors when sending the data from Avizo to COMSOL. A 3D Gaussian filter is typically represented by the function,

$$G(x, y, z) = \frac{1}{(\sqrt{2\pi}\sigma_{rel})^3} e^{-\frac{(x^2+y^2+z^2)}{2\sigma_{rel}^2}} \quad (2.2)$$

where x , y and z are the distances from the point of interest and σ is the standard deviation of the Gaussian distribution.

The Gaussian filter in Avizo Fire smoothed or blurred an image by performing a convolution operation with a Gaussian filter kernel (Visualization Sciences Group, 2010b). The ‘kernel size’ allowed the user to change the size of the convolution kernel in each dimension. The minimum kernel size is ‘1’ which means that the image was not blurred at all in the associated direction. A $\sigma_{rel} = 0.4$ with a 3x3x3 kernel produced the best results for importing the data into COMSOL. The term best results meant that the complex pore space geometry was smoothed and the image artifacts were removed so that transport properties could be calculated using COMSOL later in the workflow. An example of the original binarized image and Gaussian smoothed binarized image is shown in Figure 2.10.

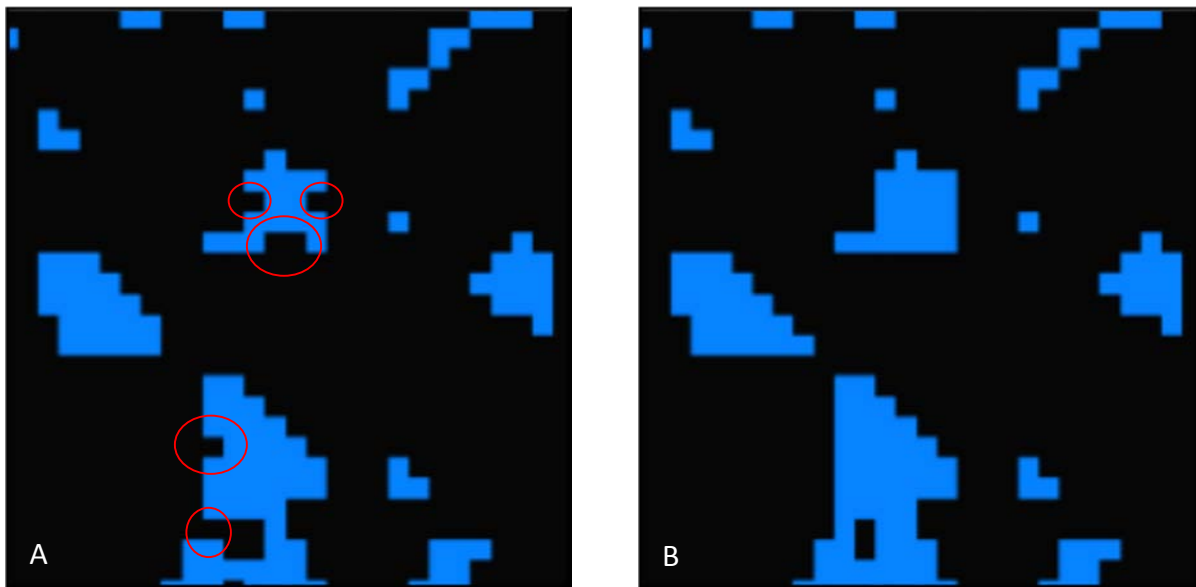


Figure 2.10 Binary image before (A) and after (B) a 3D Gauss filter was applied. The changes between the images is noted in red circles. The scale of both images is 30 x 30 voxels (23.4 x 23.4 μm).

The 3D median filter in Avizo was also tried as it is a simple edge-preserving smoothing filter. The filter worked by sorting pixels covered by a $N \times N$ mask according to their grey value. The center pixel was then replaced by the median of these pixels, i.e., the middle entry of the sorted list. The size of the pixel mask may be adjusted via the ‘kernel size’. A value of 3 denotes a 3x3 or mask (respectively 3x3x3 in 3D) (Visualization Sciences Group, 2010a). This filter may be best applied prior to binarization in order to reduce the amount of noise in an image. The median filter was tried before incorporating the 3D Gaussian filter. The image results had a significant loss of connected pore space using various kernel sizes on the binarized image. This filter was

not practical for smoothing; however, it may be useful for preconditioning the image before segmentation in the future as large images (~100 voxels) appear to be increasingly sensitive to artifacts once imported into COMSOL.

2.10 Determine Voxel Connections

An Avizo module, called Connected Components, searches for connected pore space in the 3D image. The types of connectivity can be varied by changing the flood-fill type to the following regions as shown in Figure 2.11.

- Figure 2.11 A, 6 neighbors (common face with center voxel)
- Figure 2.11 B, 18 neighbors (common face, or edge, with center voxel)
- Figure 2.11 C, 26 neighbors (all voxels)

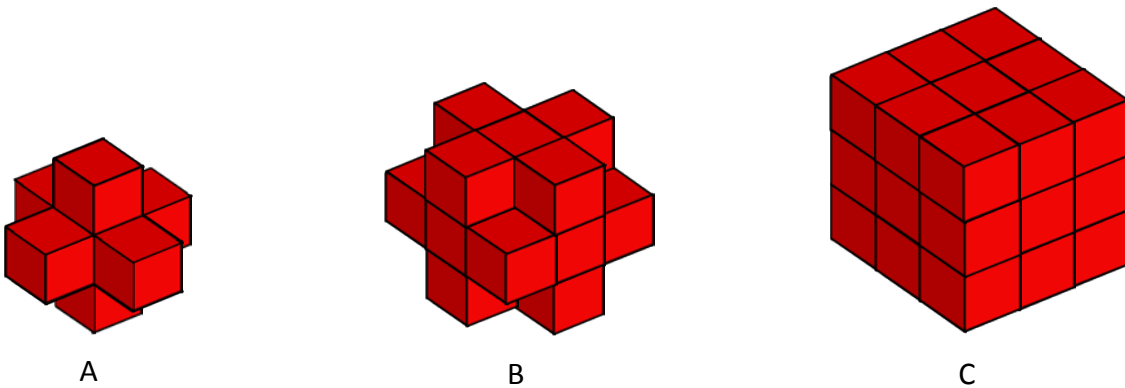


Figure 2.11 Connectivity of elements. (A) Left image is 6 voxel connections. (B) middle image is 18 voxel connections. (C) Right image is 26 voxel connections. (Visualization Sciences Group, 2010a)

If 18 or 26 neighbors were used, additional filtering was required as the majority of these voxels were connected by a single point or a single edge without a physical thickness in the adjacent coordinate plane. In addition, meshing the generated geometry required manual reconnection of the pore space using Avizo and COMSOL. This made the problem very time consuming to solve using the current solving methodology. The 6 voxel neighbors model was used because it makes the most physical sense as the voxel connections have a non-zero area.

2.11 Generate Surface

Surface generation of the connected pore space can take a significant amount of computer memory. Based on my observations, the volume of the connected pore space is approximately proportional to the amount of computer memory required for surface generation. Avizo has a built in algorithm for filtering out smaller numbers of connected voxels. For most simulations, the minimum number of connected voxels was set to 10, thereby eliminating the smaller connected regions and decreasing the voxel volume selection time. This was used to save time and it does not affect the connected voxel volume results.

Table 2.1 displays the pore space connectivity of a subsample in KD-18-03. Eight connected regions are displayed (connected volume # 0 to 7) that have a connected pore space of 10 voxels or larger. For larger simulations completed, the number of connected pore space volumes is in the thousands.

Table 2.1 Connectivity of Regions in the KD-18-03 Subsample

Connected Volume #	Volume	Center X	Center Y	Center Z
0	5682	515.0	515.0	625.0
1	79	527.0	519.5	612.5
2	14	517.0	520.5	610.5
3	74	509.0	521.5	612.0
4	13	502.0	528.0	610.5
5	31	515.5	502.5	622.5
6	17	528.5	526.5	637.0
7	24	510.5	515.0	638.5

Figure 2.12 displays the connectivity of regions listed in Table 2.1. The largest connected region has a volume of 5,682 voxels, as displayed in blue. The other colors represent the smaller connected pore space, connected volumes # 1-7, that did not intersect with the cube boundaries.

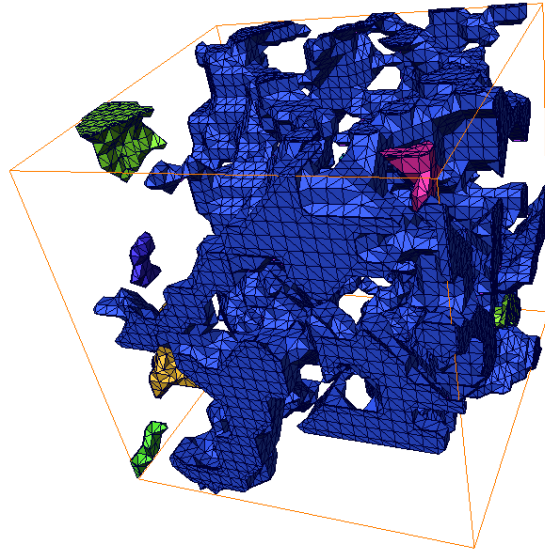


Figure 2.12 Connectivity of Regions in the Subsample as listed in Table 2.1. The scale of the image is 30 x 30 x 30 voxels (23.4 x 23.4 x 23.4 μm).

The surface view module in Avizo Fire was used to isolate whatever connected volume number we wanted to extract for processing. If this isolation process is neglected, COMSOL would import all the indexes and is likely to run out of memory either during the import process or during the calculations. This was relevant for larger subsamples of 30 voxels and greater. Figure 2.13 A displays the surface of the connected pore space in a subsample and Figure 2.13 B displays the surface of only the largest connected pore space in the subsample.

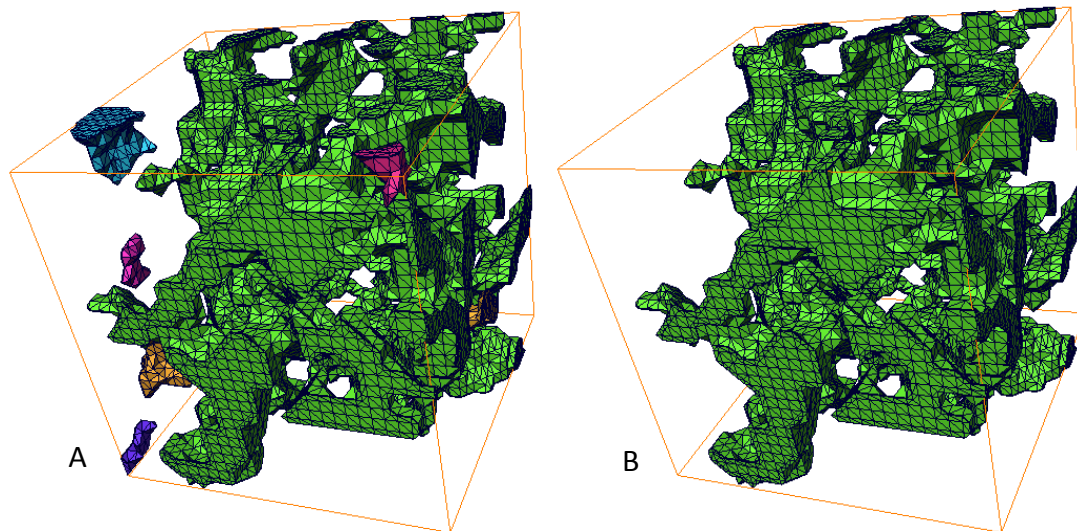


Figure 2.13 (A) Surface of all connected voxels in subvolume. (B) Surface of largest connected voxels in subsample (B). The scale for both images is 30 x 30 x 30 voxels (23.4 x 23.4 x 23.4 μm).

A comparison between using the AutoSkeleton method vs. all the connected voxel regions is shown in Figure 2.14. Figure 2.14 A displays the AutoSkeleton spatial plot data underneath a surface mesh representing the connected regions. The AutoSkeleton result was useful in estimating the connectivity. Figure 2.14 B displays the surface of all connected voxels in the subsample. Figure 2.14 C illustrates the combination of Figure 2.14 A-B. The surface of the connected voxel region has been displayed in red to highlight the complexity of the resultant surface mesh. Figure 2.14 C displays a green circle to highlight an area of interest. The AutoSkeleton spatial plot generally intersects the connected pore space, however, in the highlighted region, the spatial plot overestimates the connectivity of the pore space by joining regions not previously connected in Figure 2.14 B. The red mesh in Figure 2.14 C also has more volume than the tubular spatial plot generated. Generally, the spatial plot appears to overestimate the connectivity of the pore space and underestimate the pore throats inside the connected pore space. This observation was briefly discussed with Avizo representatives at a conference in Calgary, Alberta in 2010. After a brief discussion about my work, I was cautioned about using the AutoSkeleton spatial plot to help estimate the permeability of a rock sample.

Regardless, the AutoSkeleton is a useful visualization tool to quickly observe the approximate connectivity of the subsample pore space.

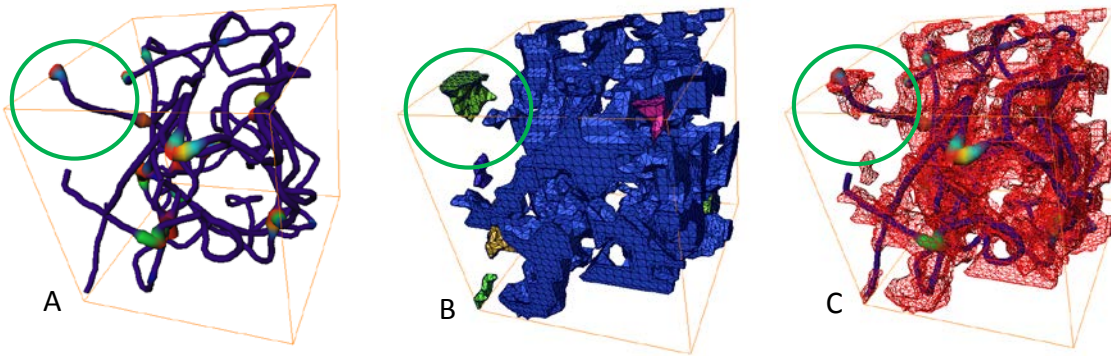


Figure 2.14 (A) Spatial plot of connected pore space using the AutoSkeleton method. (B) Surface of all connected regions in subsample. (C) Spatial plot of connected pore space superimposed inside the surface of all connected regions in a subsample. The scales of all images is 30 x 30 x 30 voxels (23.4 x 23.4 x 23.4 μm).

RemeshSurface is an algorithm in Avizo Fire that interpolates the original mesh to reduce the number of triangles generated in a subsample. The complexity of the generated mesh is a main contributor to using significant amounts of computer memory. An example of extreme surface remeshing is shown in Figure 2.15. Figure 2.15 A displays the original mesh and Figure 2.15 B displays the interpolated mesh at 59% of the original mesh elements. The RemeshSurface algorithm was constrained to interpolate the original surface smoothly so that the original geometry surface location was preserved.

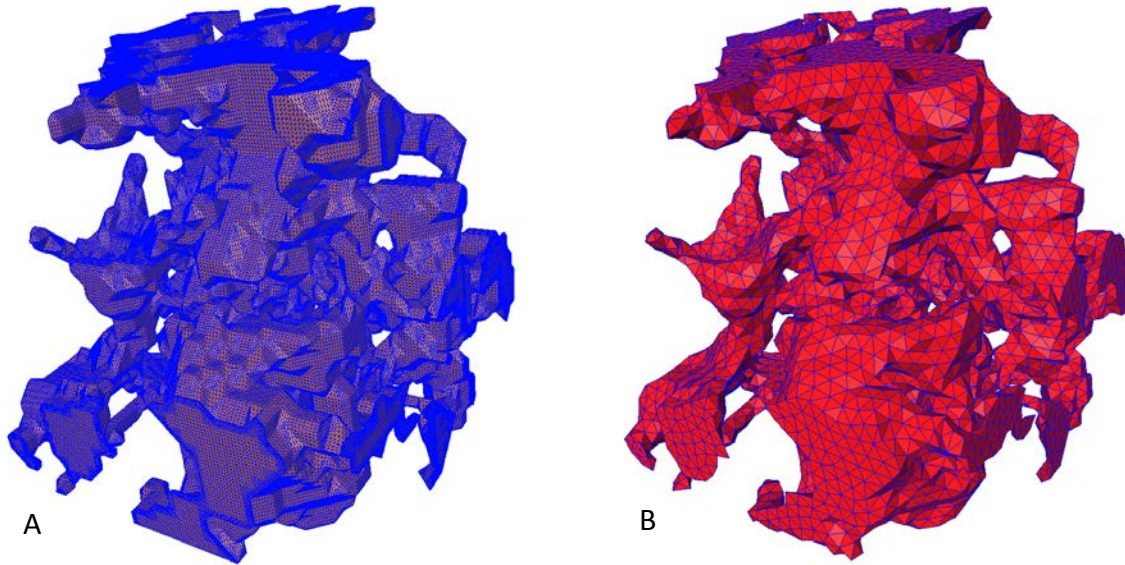


Figure 2.15 RemeshSurface algorithm used for reducing the number of elements in a mesh surface. (A) Non-remeshed surface representing the pore space. (B) The surface was remeshed to 59% of the original mesh using the RemeshSurface algorithm. The scales of the images is 30 x 30 x 30 voxels (23.4 x 23.4 x 23.4 μm).

The RemeshSurface tool was not used for most of the subsamples analyzed as inconsistent topology was typically found during the data importation into COMSOL. The generated mesh surface resulted in multiple triangle intersections on the mesh surface with manual tweaking required to run the 'stl' file in Comsol. Several of the triangular surfaces could be automatically corrected by using the built in AVZIO 'fix intersection' algorithm and the manual face partitioning in COMSOL, however, for the larger samples, it was considered too time consuming. For a 50 μm subsample size, roughly 350 manual corrections were required for each mesh surface. These topology errors were addressed using the simplification editor built into Avizo, and further refined after importing the result in COMSOL and before generating the 3D mesh representing the pore space. This process was not required for most subsamples as the computer had enough RAM to fit the simulation into the finite computer memory. For samples that could not be run inside the finite computer memory available, the RemeshSurface tool was used as a smoothing pre-conditioner and to reduce the number of mesh elements.

2.12 Export Surface

The connected pore space observed in Avizo Fire was exported to COMSOL to create a finite-element mesh representing the pore space. The Navier-Stokes equations for an incompressible fluid were then solved on the finite-element mesh.

There are multiple exportation file formats supported in Avizo Fire and several importation file formats that COMSOL accepts. For example, within Avizo Fire, the AutoSkeleton plot could be exported, but could not be imported into a format accepted by COMSOL. The surface mesh in Avizo had multiple export options, but only formats that can be imported by COMSOL were considered in this work. For the pore extraction methodology, all of the available export/import file options were tested. The STereoLithography (STL) file format was able to export a triangular surface representing the connected pore space from Avizo and import the surface into COMSOL for 3D mesh generation. The STL file format approximates 3D surfaces of a solid model in order to achieve a smooth surface (Rypl et al., 2006). The STL file output resulted in a multi-faceted triangular surface that combined individual triangles based on vertex information and the unit normal of the individual triangle (Stroud et al., 2000). An STL file, as used later in the work, incorporated 104,064 lines of information to generate the triangulated surface representing the rock pore space. An example of the ASCII STL file format is:

```
solid K:/Masters/Results/thesis_sample50.stl (14866 triangles, 7334 nodes)
  facet normal -0.970716 0.240230 0.000000
    outer loop
      vertex 508.500000 499.899994 611.000000
      vertex 508.747681 500.900818 610.755798
      vertex 508.500000 499.899994 610.000000
    endloop
  endfacet
  facet normal 0.999949 -0.007174 -0.007176
    outer loop
      vertex 517.500000 499.899994 610.000000
      vertex 517.500000 500.000000 609.900024
      vertex 517.512268 500.904785 610.705078
    endloop
  endfacet
  .
  .
  .
endsolid
```

Another pore extraction format alternative is the Nastran export format. The standard Avizo software has an add-on package called Avizo Wind which included the Nastran file format. This file format enabled a 3D tetrahedral mesh to be created directly in Avizo, as opposed to the STL file format where the surface mesh was exported from Avizo Fire and the 3D tetrahedral mesh was generated using COMSOL. Generally, the Nastran exportation format was easier to use, however, increasing or decreasing the mesh resolution in COMSOL was used frequently. The mesh resolution changes were used to test the convergence of the numerical solution between input mass fluid flux and output mass fluid flux. COMSOL also has additional mesh controls where the mesh was automatically modified to a finer or coarser mesh. The Nastran format was found to be easier for setting up the initial mesh. Considering the multiple mesh resolution changes required, COMSOL's advanced mesh control algorithm and the additional cost for the Avizo Wind add-on module, COMSOL was more practical to use for the samples investigated in this work, therefore, the STL file format was used.

3 PHYSICS METHODOLOGY

3.1 COMSOL Multiphysics Workflow

COMSOL Multiphysics was used to import the triangular surface generated using Avizo, and mesh the triangular surface representing the boundary between the pore space and rock matrix. COMSOL was then used to solve the Navier-Stokes equations for the fluid flow and Laplace's equation for the electrical current density. The following COMSOL Multiphysics workflow shows a brief summary of each process as described below.

- Import geometry
- Add physics
- Set initial values and boundary conditions
- Mesh 3D volume
- Analyze solution

3.2 Import Geometry

The triangular surface that represents the connected pore space was imported into COMSOL using the STL file format. Figure 3.1 displays the imported triangular surface before it was meshed using COMSOL.

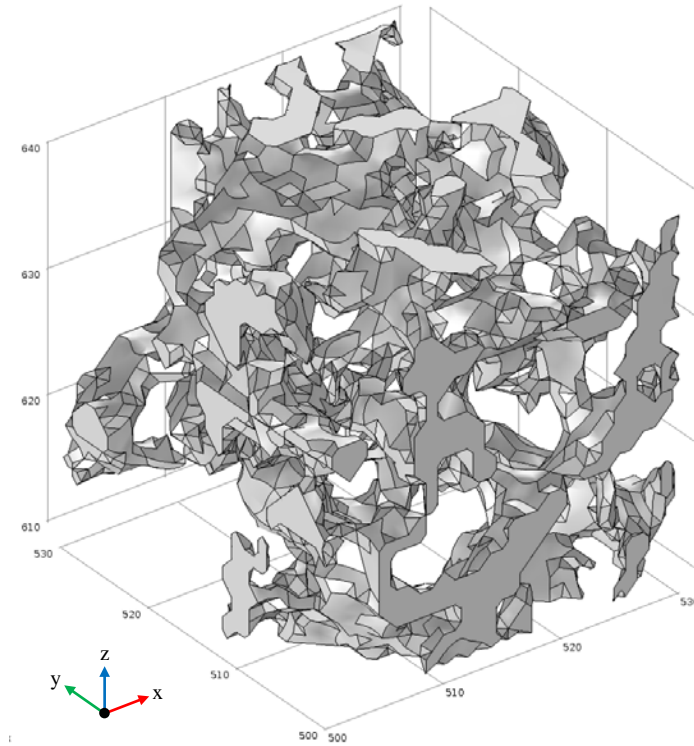


Figure 3.1 View of triangular surface imported into COMSOL. The connected pore space is shown after exporting the STL file from Avizo. The image size is 30 x 30 x 30 voxels (23.4 x 23.4 x 23.4 μm).

The geometry from the STL file format is generally not unique. In other words, there may exist several geometries that are represented by the same STL file generated. Full automation of the STL file importation is generally impossible without user intervention (Rypl et al., 2006). An STL file format deficiency is the lack of coherence between the facets. A facet is a graphical method consisting of subdividing the edges and triangulation of the faces. If many small facets exist in the STL file, then there is a risk for mismatching vertices, and hence for creating incorrect topology (Stroud et al., 2000).

STL geometry modifications were required to correct the topology for some simulations. For these simulations, manual face partitioning in COMSOL was completed. This included adjusting the maximum angle in the face, maximum face neighbor angle, minimum relative area and removal of small faces. After completing manual fixes, COMSOL was able to import the STL triangular surface representation and generate a 3D mesh without internal geometry errors. The manual face partitioning process took anywhere from several hours to two weeks to complete depending on the complexity of the subsample mesh.

3.3 Add Physics

The Laminar Flow COMSOL Module was used to model fluid flow through the pore spaces using the steady-state incompressible Navier-Stokes equations. The equations used in the COMSOL PDE solver are:

$$\rho[\vec{u} \cdot \nabla \vec{u}] = -\nabla p + \nabla \cdot \tau \quad (3.1)$$

where ρ , \vec{u} , p , and τ are the density, velocity vector, pressure and viscous stress tensor.

The viscous stress tensor is:

$$\tau = \eta[\nabla \vec{u} + (\nabla \vec{u})^T] = \eta \begin{bmatrix} 2\frac{\partial u}{\partial x} & \frac{\partial u}{\partial y} + \frac{\partial v}{\partial x} & \frac{\partial u}{\partial z} + \frac{\partial w}{\partial x} \\ \frac{\partial v}{\partial x} + \frac{\partial u}{\partial y} & 2\frac{\partial v}{\partial y} & \frac{\partial v}{\partial z} + \frac{\partial w}{\partial y} \\ \frac{\partial w}{\partial x} + \frac{\partial u}{\partial z} & \frac{\partial w}{\partial y} + \frac{\partial v}{\partial z} & 2\frac{\partial w}{\partial z} \end{bmatrix} \quad (3.2)$$

where η is the dynamic viscosity.

The mass conservation equation is:

$$\nabla \cdot \vec{u} = 0 \quad (3.3)$$

The form of Equation 3.3 implies that the fluid is incompressible.

The Electric Currents COMSOL Module was used to model current flow through the pore space. The equations used in the COMSOL PDE solver are:

$$\nabla \cdot \vec{j} = 0 \quad (3.4)$$

where \vec{j} is the current density vector.

$$\vec{J} = \sigma \vec{E} + \vec{J}_e \quad (3.5)$$

where σ , \vec{E} , and \vec{J}_e are the conductivity, electric field, and current density of other forces respectively.

$$\vec{E} = -\nabla V \quad (3.6)$$

where \vec{E} , and V are the electric field and voltage.

When equations 3.4, 3.5 and 3.6 are combined, assuming \vec{J}_e is zero and σ is constant, the equations result in Laplace's equation:

$$\nabla^2 V = 0 \quad (3.7)$$

3.4 Set Initial Values and Boundary Conditions

The initial values and boundary conditions were applied to the mesh surface. Figure 3.2 displays the triangular surface after it was meshed using COMSOL.

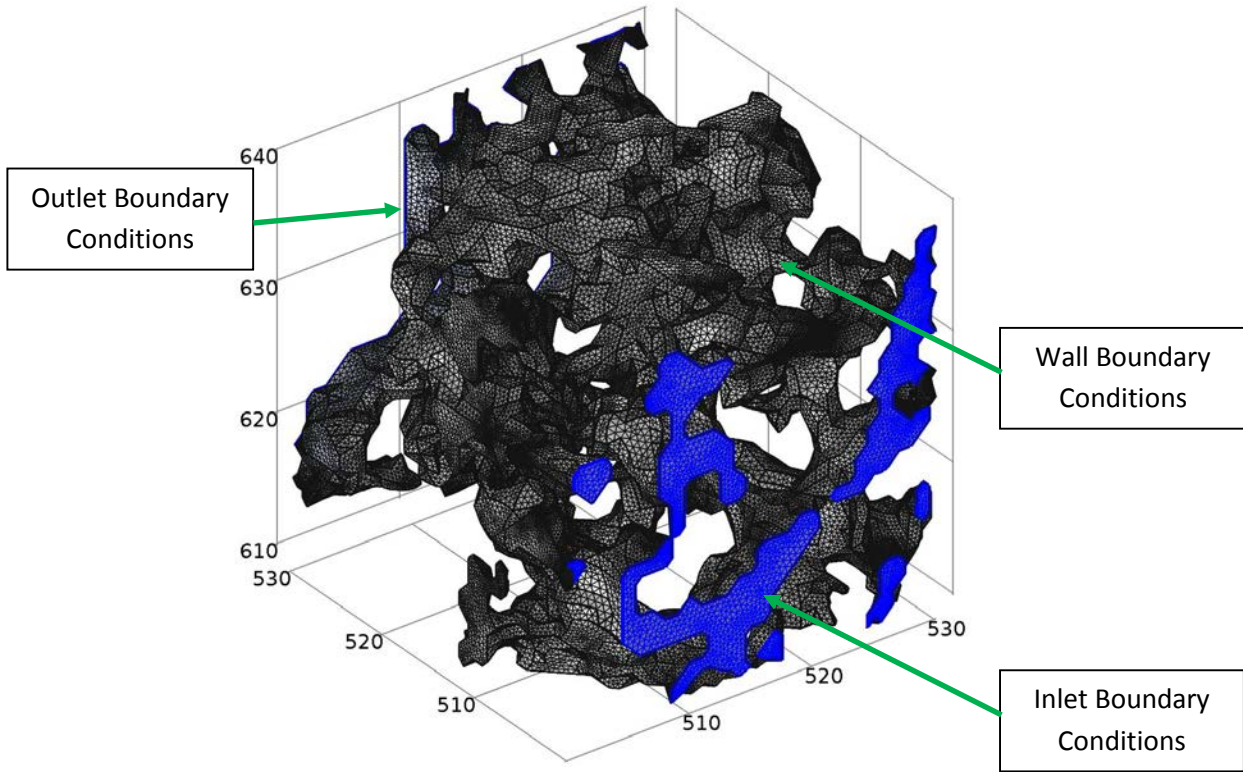


Figure 3.2 Setting Boundary Conditions and Initial Values on the STL import mesh. The image size is 30 x 30 x 30 voxels (23.4 x 23.4 x 23.4 μm).

The inlet boundary condition is:

$$p = 1, \quad \eta[\nabla\vec{u} + \nabla\vec{u}^T]\vec{n} = 0 \quad (3.8)$$

$$V = 1 \quad (3.9)$$

The second term in Equation 3.8 indicates that the viscous stress is zero.

The outlet boundary condition is:

$$p = 0, \quad \eta[\nabla\vec{u} + \nabla\vec{u}^T]\vec{n} = 0 \quad (3.10)$$

$$V = 0 \quad (3.11)$$

The wall boundary condition is applied along the pore walls:

$$\vec{u} = 0 \quad (3.12)$$

$$n \cdot \vec{j} = 0 \quad (3.13)$$

where there is no slip for the fluid flow and electrical insulation for current flow on the walls.

The initial values are:

$$u = 0, p = 0 \quad (3.14)$$

$$V = 0 \quad (3.15)$$

where flow velocity, u , pressure, p , and electric potential, V , are zero.

The parameter values used are '1' because we have scaled the solutions. The solutions used voxel units as imported from Avizo and were later corrected to the μm units. The details of the scaling is shown in Appendix B, called Scaling Factors for Modifying Equations to Real World Values. Appendix B shows how the calculated transport properties were obtained for a result shown in Table 4.2. The parameter values are:

$$\rho = 1, \quad \mu = 1 \quad (3.16)$$

$$\sigma = 1 \quad (3.17)$$

3.5 Mesh 3D Volume

Figure 3.3 displays the subsample surface mesh and domain mesh after importing the STL file into COMSOL. Figure 3.3 A displays the 3D domain mesh. A transparency level of 70% was used to help visualize the 3D mesh complexity. Figure 3.3 B shows a magnified region of the surface mesh.

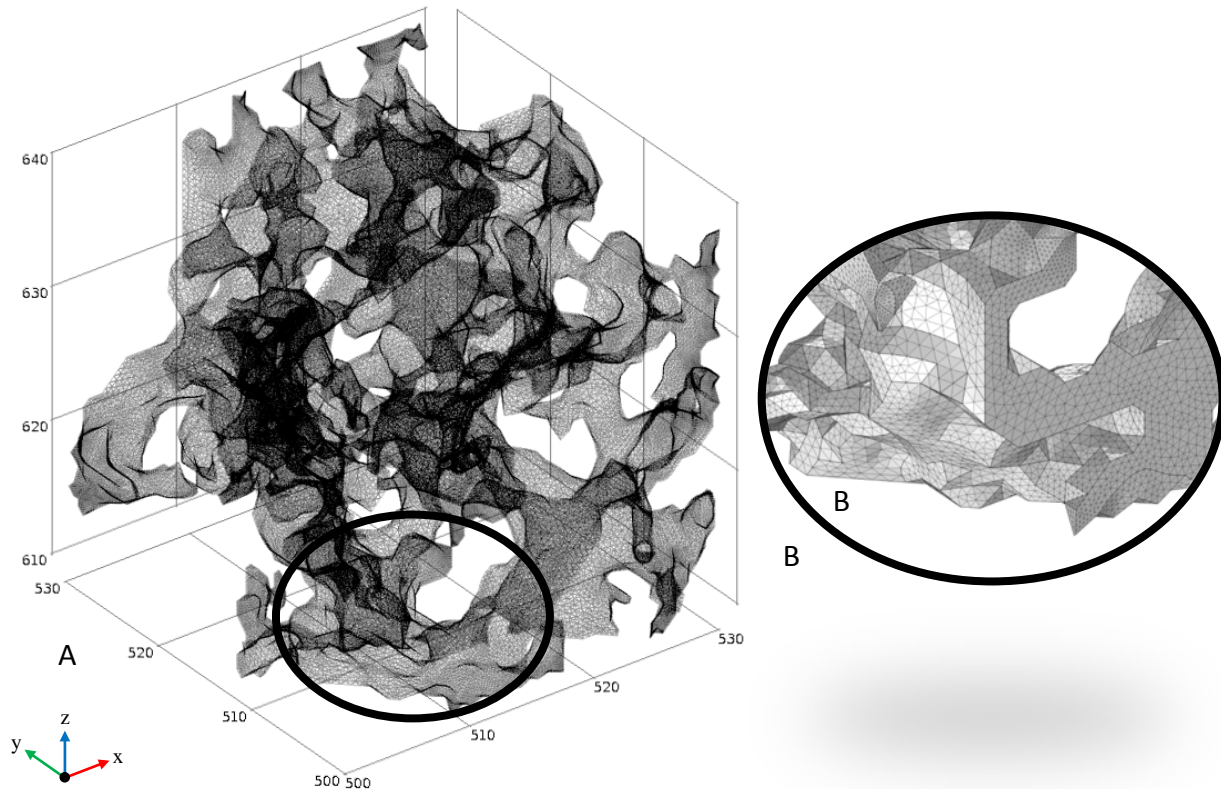


Figure 3.3 3D tetrahedral mesh representing both the surface and the domain. (A) The domain mesh is displayed with a transparency level of 70% to help visualize mesh complexity. (B) Magnified section of the surface mesh. The image size is 30 x 30 x 30 voxels (23.4 x 23.4 x 23.4 μm).

The fine triangular resolution of the surface mesh was amplified while generating a larger number of interior mesh elements. The subsample surface mesh and resultant domain mesh resulted in many equations that had to be solved. The solution time and memory required are strongly related to the number of equations in the Model (COMSOL Multiphysics, 2011c). The 3D tetrahedral mesh, shown in Figure 3.3, has 1,989,322 mesh elements and generates 4,332,920 equations to solve for the combined Navier-Stokes and Laplace equations. COMSOL calculates the number of equations as the number of dependent variables multiplied by the

number of nodes. The dependent variables in the steady state Navier-Stokes Equations are velocity and pressure. Voltage is the dependent variable in Laplace's Equation. The number of nodes was dependent on the mesh settings used. If tetrahedral mesh elements are used, it is approximately 4.6 times the number of elements (COMSOL Multiphysics, 2011c).

Mesh settings used in COMSOL also varied with the complexity of the STL file. Boundary layer meshes are generally easier to generate correctly in 3D. Free tetrahedral meshes were used when the automatic boundary layer mesh produced meshing errors. A boundary layer mesh is typically used across boundaries where there are strong gradients. This is also true for laminar flow conditions since there is a no-slip boundary condition on the walls with pressure gradients at the inlet. In comparison with boundary layer meshes, free tetrahedral meshes required a higher mesh resolution to achieve the same inlet and outlet mass flux on the boundaries.

3.6 Partial Differential Equation Solver Considerations

The steady state partial differential equation solvers used in COMSOL were either direct, segregated, or iterative multigrid. The segregated solver could be useful to determine the convergence of each variable in the partial differential equations. The segregated solver was used for several simulations, but it wasn't essential as the Navier-Stokes equations and Laplace's equation are independent (i.e. velocity and pressure are independent of the voltage). The iterative multigrid solver can use either Incomplete LU factorization or Multigrid to solve. The multigrid solver can be used with a coarser mesh used first to guess the solution and a higher resolution mesh to calculate the solution within the mass fluid flux convergence limits. For complex mesh cases, a third mesh was generated in order to obtain convergence of the solution. The mesh generation process was problematic, and manual corrections were required for coarser meshes as well as the higher resolution meshes. To save time, a direct solver was used for a single mesh case. Theoretically, a direct solver will use more physical memory when solving the equations; however, in practice this was not found to be the case. Multiple mesh generation used significant hard drive space, up to approximately 800 GB in some cases, before COMSOL would start the solution process. Overall, a direct solver was used for complex meshing cases as only a single mesh was required for a solution. For simple mesh cases, an iterative multigrid system was used to generate a coarse mesh case for a first guess, followed

by a higher resolution mesh to generate solutions. The segregated, direct and iterative multigrid solvers were found to generate the same solution, within a tolerance of 0.1%.

3.7 Representative Elementary Volume Surface

It is very important that the model of the pore space is representative of the rock structure at a larger scale when using pore scale modeling to predict macroscopic parameters (Mostaghimi et al., 2013). An important aspect to learn from my study is whether I could solve for fluid flow in a volume as large as a Representative Element Volume (REV). The volume was considered to be a REV if macroscopic properties, such as porosity and permeability, did not change with an increased box size. An estimate of the actual REV for porosity was made, as shown in Figure 1.1, based on the Midale Marly rock synchrotron data.

Figure 3.4 shows a 2D slice inside a 3D sub-volume from a synchrotron image representing the inside of the Midale Marly rock used in this investigation. The image size, as shown in Figure 3.4 A, is 1597 x 1597 μm in the x and y directions respectively. I considered porosity with squares of side length L. In Figure 3.4 B, I show concentric squares of increasing L. The largest image sub-sample size, as shown in blue, is 5.84 x 5.84 μm in the x and y directions. The z direction was omitted from the graph for clarity. The decreasing size of concentric squares are shown with the same CMT orthoslice layer to help visualize the decreasing size of the sub-sample with respect to the largest image sub-sample size. In Figure 3.4 C, the correct orthoslice layer within each of the concentric squares is shown. The CMT images were first cropped in 3D, then the images were thresholded and binarized before the porosity calculations were carried out. The volume of the box was first set at the maximum sample size for the sample volume with a sample length of 1100 voxels (858.0 μm). The largest of the concentric squares was set for a sample length of 255 voxels (198.9 μm) and the volume of the box was then decreased using sequentially smaller boxes.

The porosity is shown as a function of L and it can be seen to fluctuate strongly with L until L exceeds L_0 at which point the square includes a statistically representative sample of the rock (Bear, 1972). The porosity was for individual samples of lengths 1.5, 3.9, 15.6, 39.0, 78.0, 117.0, 156.0, 198.9, 858.0 μm . The cropped data regions and orthoslice numbers displayed are

given in Table 3.1. A 3D cube with side length L_0 is called the REV. If the medium is heterogeneous, then there is a larger length scale at which macroscopic properties change and whose length may be outside the REV.

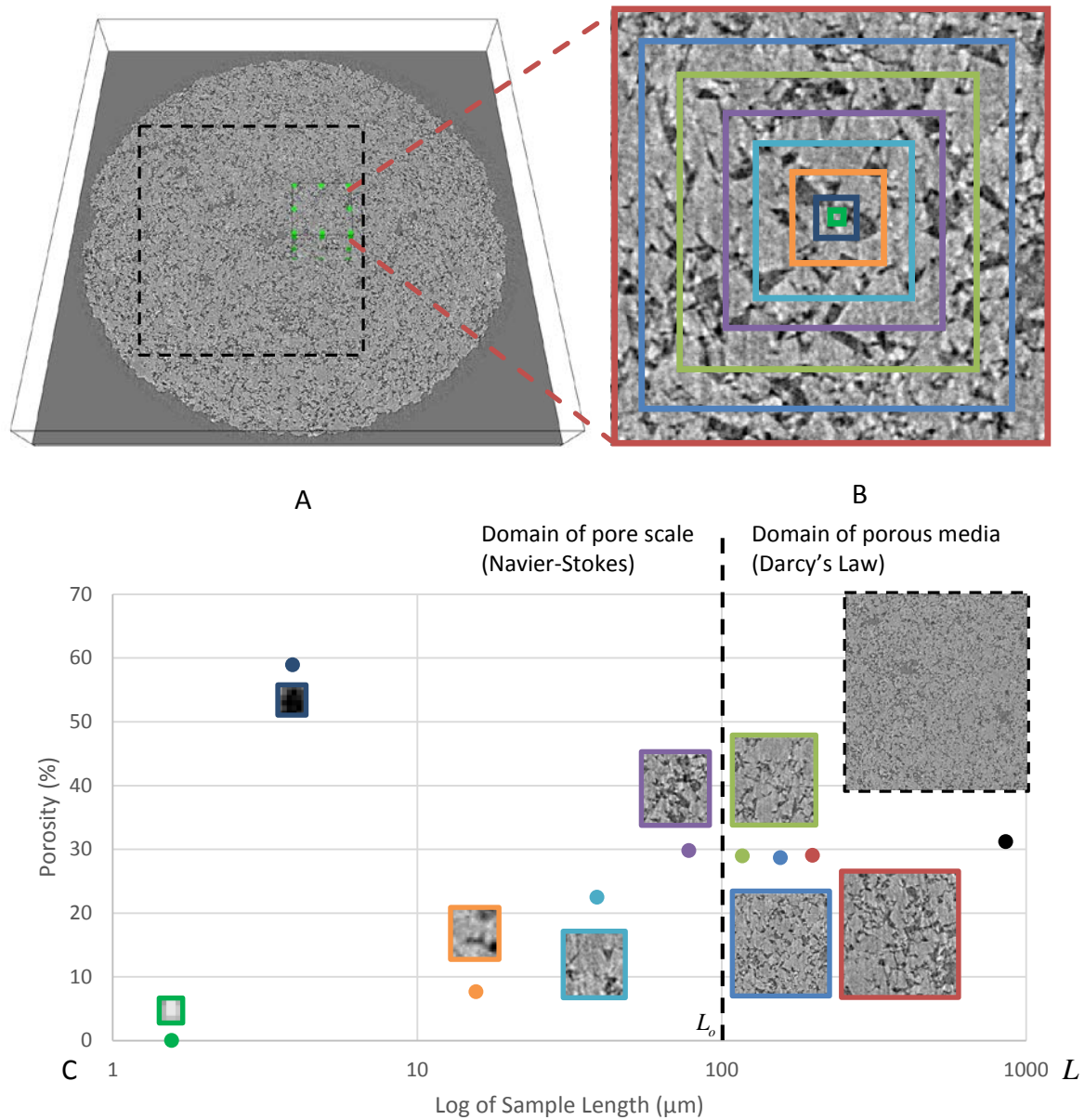


Figure 3.4 (A) A 2D slice inside a 3D sub-volume from a synchrotron image representing the inside of a Midale Marly rock. The 8 bit greyscale ranges from the pore space (grey-black, 0) to the rock matrix (white, 255) with a threshold value of 85 representing the rock pore space. (B) The isolated sub-volume has eight isolated regions for calculating the average porosity. The four largest squares are larger than a REV and all other colored squares are smaller than the a REV. (C) The porosity vs. characteristic length in terms of a REV (after Bear, 1972). The images range from a length scale of 1.6 to 858 μm . The black, red, blue and green squares are above the side length, L_0 , and are considered to be a REV for porosity.

Table 3.1 displays the sample volume, sample length, total porosity, isolated x, y and z regions and the slice number for the images displayed in Figure 3.4 C. The orthoslice number ranged from 0 to 255 in the z-direction. The calculated total porosity fluctuates with smaller samples, as illustrated in Figure 3.4 C. Relative constancy in the porosity calculations started around 78.0 μm^3 (100 voxels) indicating that the REV volume is roughly 78.0 μm cubed or 100 voxels cubed. The results are shown in Table 3.1.

Table 3.1 Representative Elementary Volume (REV) Porosity Change Investigation

Sample Length (voxels)	Sample Length (μm)	Total Porosity (%)	x-direction region	y-direction region	z-direction region	Orthoslice number
1100	858.0	31.2%	300 to 1400	500 to 1600	0 to 255	126
255	198.9	29.1%	1000 to 1255	1000 to 1255	0 to 255	177
200	156.0	28.7%	1025 to 1225	1025 to 1225	25 to 225	202
150	117.0	29.0%	1050 to 1200	1050 to 1200	50 to 200	60
100	078.0	29.8%	1075 to 1175	1075 to 1175	75 to 175	106
50	039.0	22.5%	1100 to 1150	1100 to 1150	100 to 150	123
20	015.6	07.8%	1125 to 1145	1125 to 1145	125 to 145	136
5	003.9	58.9%	1135 to 1140	1135 to 1140	125 to 130	125
2	001.6	00.0%	1138 to 1140	1138 to 1140	128 to 130	130

The largest square box that can fit inside the circular CMT sample, without including incorrect porosity values associated with CMT artifacts, is shown in Figure 3.4 A. This was taken from voxel position 300 to 1400, 500 to 1600 and 0 to 255 voxels in the x, y and z directions. The real dimensions of this box are 858.0 x 858.0 x 198.9 μm . The calculated porosity value was 31.16%. This porosity is reasonably close to the porosity range for sample sub-volumes between 78.0 μm and 198.9 μm in Table 3.1 where the porosity ranges from 28.7% to 29.8%.

To provide a more quantitative estimate of the REV, the number of sample volumes calculated was '20' for each of the 30, 50, 100 and 200 voxel regions. A random number generator was used to isolate the subsample volumes and porosity was determined within the cube. The random number generated was restricted to provide values within the cube volume of the

subsample domain. Since the CMT occupied a circular region, if the location of the randomly generated volume was outside of the CMT data domain, a new random number was generated. Table 3.2 lists the sample length, total porosity and standard deviation for a random isolated region ranging from 224 to 1492 μm (30 to 200 voxels). All of the porosity results, along with the randomly isolated regions, are listed in Appendix A.

Table 3.2 Porosity change for Random 200 Voxel Regions

Sample Length (voxel)	Sample Length (μm)	Sample Volume (voxel ³)	Sample Volume (μm^3)	Total Porosity (%)	Standard Deviation (%)	# of Samples (n)
30	23.4	27,000	12,812.9	21.8	17.4	20
50	39.0	125,000	59,319.0	24.6	10.2	20
100	78.0	10 ⁶	474,552.0	28.3	4.89	20
200	156.0	8·10 ⁶	3,796,416.0	29.3	2.85	20

The total porosity is 28.3% and 29.3% for the 100 and 200 voxel regions respectively. This porosity variation is less than 1%. The standard deviation is 4.89% for the 100 voxel region and 2.85% for the 200 voxel region.

Figure 3.5 illustrates all values of porosity calculated and the associated length. In this plot, the standard deviation is significantly less than the mean for the sample length of 156.0 μm (200 voxel) and 78.0 μm (100 voxel). The L_0 in the same location as shown in Figure 3.4 C, where the cube with side length L_0 and above is considered to be inside the REV.

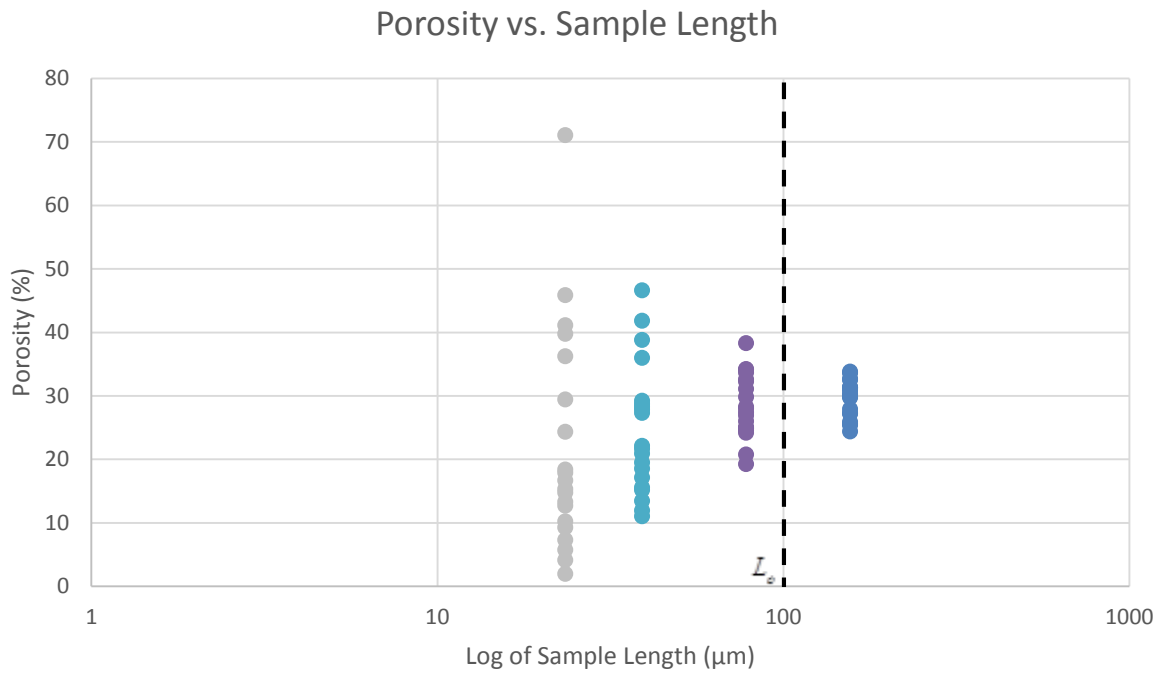


Figure 3.5 Porosity (%) vs. Log of Sample Length (μm)

Figure 3.6 displays the standard deviation vs. sample length for 20 measurements, shown in Table 3.2, along with the porosity vs. sample length, from Figure 3.4 C.

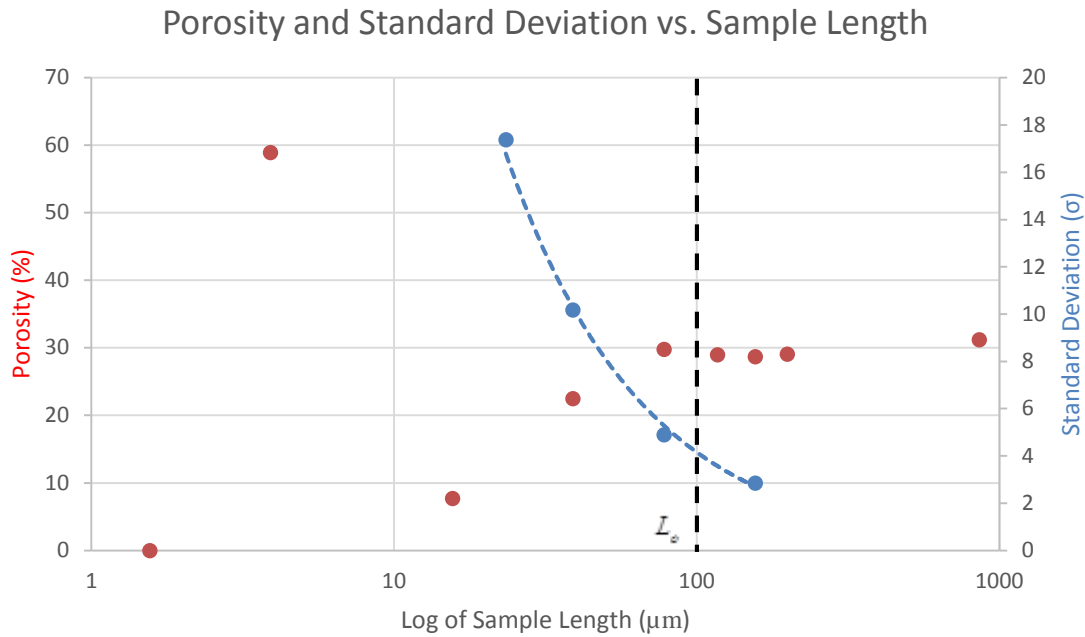


Figure 3.6 Porosity and Standard Deviation vs. Log of Sample Length (μm)

The number of samples used for each cube size was 20. The number of samples could have been increased for smaller cube volumes so that the total volume for the large cubes and the small cubes would have been the same, however, this was considered not necessary for the purposes of observing the trend shown Figure 3.6.

The standard deviation decreases with increasing sample length. For samples of side length 78.0 μm (100 voxels), the standard deviation becomes much less than the mean porosity, therefore the REV appears to begin in the range of 100 to 200 voxels (78 to 156 μm) for the Midale Marly KD-18-03 subsample. Figure 3.7 illustrates a 200 voxel region located within KD18-03 subsection 3.

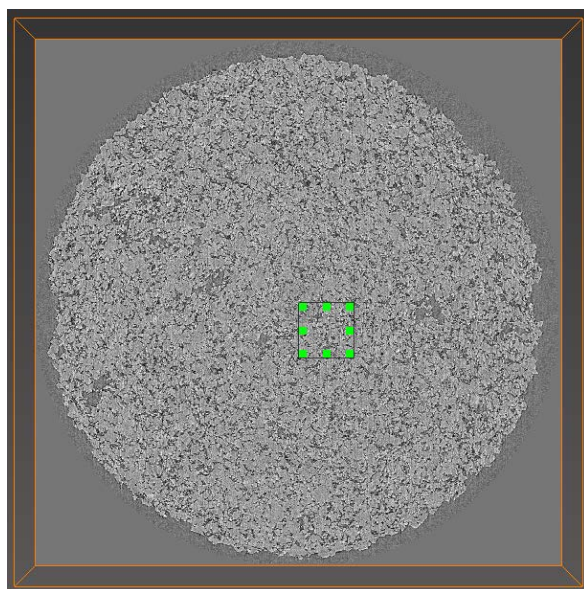


Figure 3.7 REV region located within the Midale Marly KD-18-03 subsample. The 3D dimensions of the box are 200 x 200 x 200 voxels (156 x 156 x 156 μm).

Figure 3.8 displays the 200 voxel (156 μm) region isolated to help illustrate the meshing complexity of a 200 voxel region. A layer of haze was added to help give depth and illustrate the complexity of the surface of the connected pore space.

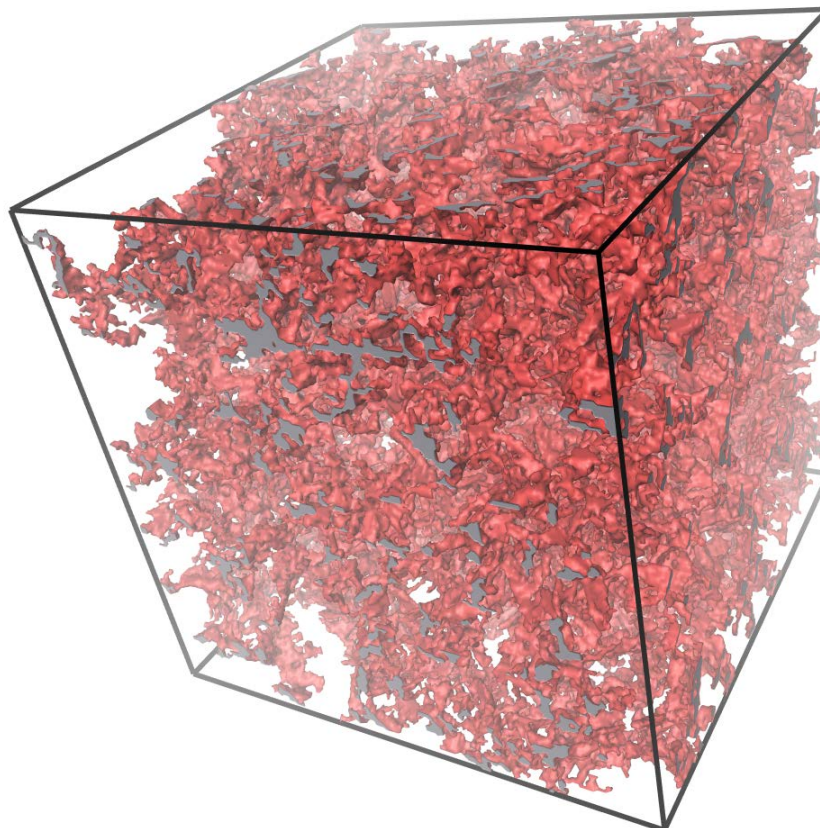


Figure 3.8 Connected pore space from a 200 voxel³ (156 μm^3) region within KD-18-03.

The red surface shows the pore walls. The grey surfaces are the boundaries touching edges of the 3D box. The surface of the pore space translates to an STL output file with over 3.3 million triangles.

Using cubic scaling of the number of equations used in simulations, it was estimated that the 200 voxel region will generate over 100 million equations to be solved. Finite computer memory limitations prevented me from calculating the permeability for a volume this large. This is partially due to the fact that high resolution CMT data was required to capture the pore resolution. Generally speaking, higher CMT resolution translated to using a smaller subsample size due to computer memory limitations. Using a volume with a complicated mesh may require

other solver solutions to be pursued. This region could potentially be completed using Lattice Boltzmann equations where the simulation could be parallelized and solved using cluster computing technology.

The REV for a carbonate rock was investigated in binarized pore space images in the paper called, "Computations of Absolute Permeability on Micro-CT Images" (Mostaghimi et al., 2013). Permeability was calculated for both consolidated and unconsolidated rock using both LMB and FVMs. The REV for porosity, permeability and specific surface area was calculated as a function of the image size. The REV for carbonate rock was higher than the sample volume, however, the paper illustrated that the REV for permeability is higher than the REV for porosity or specific surface area. The calculated permeability using the LVM was also 17% of the calculation time using LBM, which may provide useful insights into future work.

3.8 Estimating Porosity, Permeability, Formation Resistivity Factor and Cementation Exponent from Pore Scale Geometries

The equations used to calculate the porosity, permeability and electrical resistivity are summarized in Section 1.3.1. The equations below were used to calculate the mass fluid flux, porosity, permeability, formation resistivity factor and cementation exponent using COMSOL.

The mass fluid flux was calculated to determine if the subsample was in the Darcy flow regime and to calculate the permeability. The mass fluid flux was calculated using:

$$q = \frac{\iint \vec{u} \cdot \vec{n} \, ds}{S} \quad (3.18)$$

where q is the Darcy velocity, or transport velocity, and $\iint \vec{u} \cdot \vec{n} \, ds$ is the surface integral of the normal component of velocity. The integral was calculated for the inlet and outlet boundary only. S is the total cross sectional area of the box perpendicular to the flow.

If the sample was in the Darcy flow regime, as explained in the next section, the average of the inlet and outlet mass fluxes was used to calculate the permeability. The inlet and outlet mass fluxes should be identical. The mesh resolution was increased in COMSOL until the mass flux

on the inlet and outlet boundaries were essentially the same. The small difference calculated was used as a measure of the error in the calculation.

After solving the Navier-Stokes equations through the pore space, Darcy's equation was used to directly calculate the permeability using Equation 1.2.

The porosity of the sample was calculated using the formula:

$$\phi = \frac{\iiint dL^3}{L^3} \quad (3.19)$$

where $\iiint dL^3$ is the volume of connected voxels and L is the side length of the box.

The total current was calculated using:

$$I = \iint \vec{j} \cdot \vec{n} \, ds \quad (3.20)$$

where $\iint \vec{j} \cdot \vec{n} \, ds$ is the surface integral of the normal component of the electrical current density. The integral was evaluated over the inlet and outlet boundaries separately and the values were averaged.

The resistance and resistivity of the sample were calculated using equations 1.5 and 1.6, respectively. The formation resistivity factor was calculated using equation 1.4 and the cementation exponent was calculated using equation 1.8. The value of 'a' was not assumed to be equal to 1, but was calculated using data from the slope of the best fitting line through a plot of the log of the formation factor vs. the log of the effective porosity.

4 RESULTS 1, HIGH RESOLUTION MARLY SAMPLES (0.78 μm RESOLUTION)

4.1 Darcy's Flow Regime Verification

Solutions of the Navier-Stokes equations were computed with different inlet pressures for the same pore geometry in order to confirm a direct proportionality between the mass fluid flux, q , and pressure, p , as Darcy's Law specifies. Physically, the fluid flow will be in the Darcy regime if the resistance to flow is dominated by the viscous drag of the pore walls. This also means that the thickness of the viscous boundary layer must be much greater than the size of a pore throat. Laplace's equation does not contain any nonlinear terms and so the electrical current will always be proportional to the voltage difference.

The nomenclature for naming the Model is displayed as [Sub-sample number] – [direction of flow] [simulation number]. For example Model 1-x1 is [Model 1] – [flow in the x direction] [simulation 1 of 5]. A pressure gradient change between inlet and outlet sections resulted in a proportional mass fluid flux change for [Model 1-x]. The results are listed in Table 4.1.

Table 4.1 Darcy's Flow Regime Verification for [Model 1]

Model	Inlet Pressure (N/voxel ²)	Inlet Pressure (Pa)	Outlet Pressure (N/voxel ²)	Outlet Pressure (Pa)	Darcy Velocity (m/s)	Permeability (mD)	Figure
1-x5	1	6.08 e-13	0	0	1.51 e-10	3.53	4.1
1-x5	2	1.22 e-12	0	0	3.02 e-10	3.53	4.1
1-x5	4	2.43 e-12	0	0	6.03 e-10	3.53	4.1

Since the permeability remains constant for a varying pressure gradient, I conclude that the pressures are sufficiently low to be in the Darcy flow regime.

4.2 Fluid Flow and Electrical Current Density Results

Solutions to the Navier-Stokes equations and Laplace equation were calculated using the KD-18-03 pore geometry for different sample sub-volumes in three orthogonal directions. Figure 4.1 shows the flow diagrams as solutions to the Navier-Stokes equations and electrical current density diagrams as solutions to the Laplace's equation from a KD-18-03 subsample. Figure 4.1 The sample size shown in Figure 4.1 is $(30 \text{ voxel})^3$, $(23.4 \text{ } \mu\text{m})^3$ with a CMT resolution of $0.78 \text{ } \mu\text{m}$. The streamline is the velocity field and the streamline color is the velocity magnitude. The surface mesh is displayed in grey. These solutions will be discussed in greater detail in the next section.

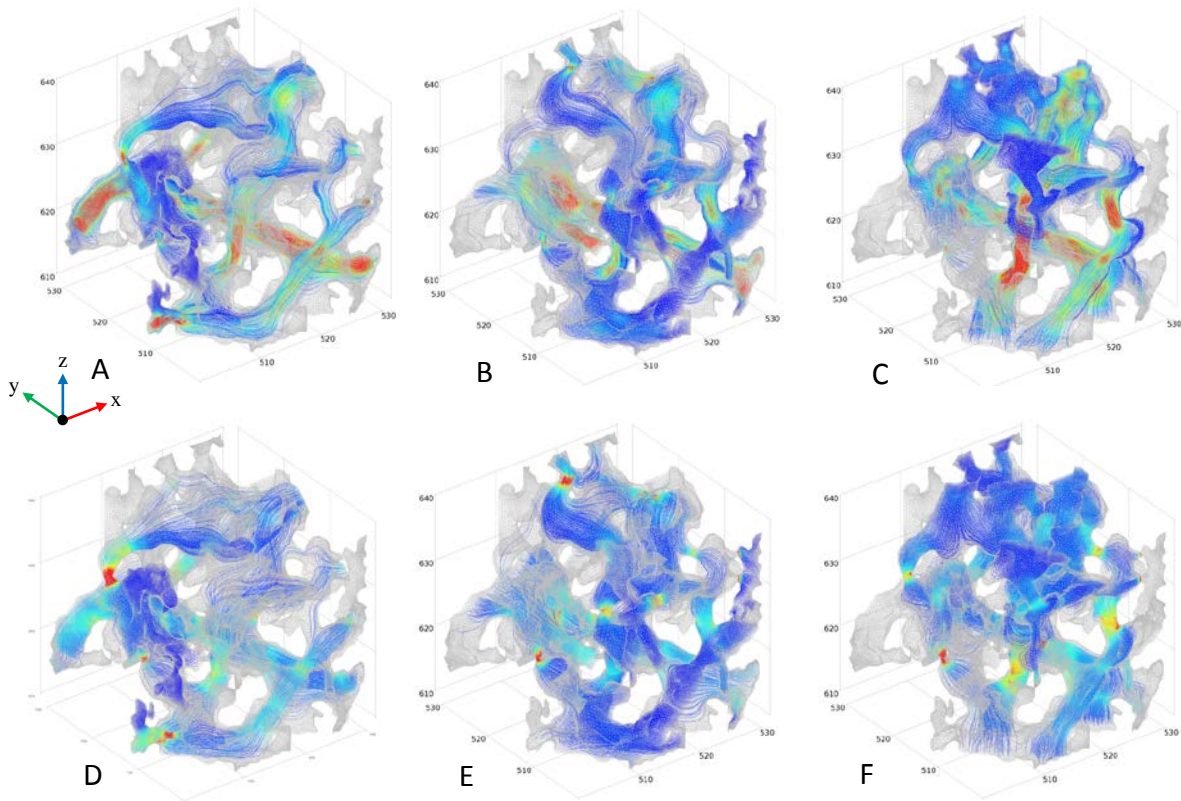


Figure 4.1 Flow diagrams and electrical current density diagrams. A, B and C, show solutions to the Navier-Stokes equations in the x-direction, y-direction and z-direction respectively. D, E and F, show solutions to Laplace's equations in the x-direction, y-direction and z-direction respectively. The sample size is 30 x 30 x 30 voxel (23.4 x 23.4 x 23.4 μm). The streamlines show the Current Density Magnitude and Velocity Magnitude. The red color represents the high values while the blue color represents the low values.

A summary of the calculated porosity, resistance, resistivity, formation factor and cementation exponent are listed in Table 4.2. Appendix B illustrates the scaling required to convert model calculated results to those for a sample with the given dimensions. The example, used in Appendix B, is Model 1-y5.

Multiple simulations were run in order to investigate the effects of varying model resolution. The difference between the inlet and outlet mass flux was used as an estimate of the model error. [Model 2] has the highest mass flux difference of 8.3%. This high mass flux difference is due to using a coarse mesh with 1,899,423 equations. A finer mesh could not be applied since

topography errors were generated in COMSOL. The majority of the models have a difference of 2.0% or less. The total porosity refers to all the porosity in the isolated subsample while the effective porosity refers to the porosity that is connected to the boundary by a pore network. The lower resolution calculations, such as [Models 1-y1] to [Model 1-y4], were used to assess whether the permeability was a function of the mesh and so only the permeability and error was recorded.

Table 4.2 Calculated Properties for the KD-18-03 Subsample

Model	Permeability (mD)	Total Porosity (%)	Effective Porosity (%)	Resistance $(\frac{\Omega \cdot m}{\text{voxel}})$	Resistivity ($\Omega \cdot m$)	Formation Factor (F)	Cementation Exponent (m)	Figures
1-y1	2.63	-	-	-	-	-	-	
1-y2	2.99	-	-	-	-	-	-	
1-y3	3.23	-	-	-	-	-	-	
1-y4	3.54	-	-	-	-	-	-	
1-y5*	3.40	19.7%	18.5%	0.98	29.3	29.3	2.00	4.5 & 4.6
1-z1	2.26	-	-	-	-	-	-	
1-z2	2.65	-	-	-	-	-	-	
1-z3	2.86	-	-	-	-	-	-	
1-z4	3.19	-	-	-	-	-	-	
1-z5*	3.27	19.7%	18.5%	1.00	30.08	30.1	2.02	4.7 & 4.8
1-x5*	3.53	19.7%	18.5%	0.94	28.36	28.4	1.98	4.9 & 4.10
2-z1	0.41	-	-	-	-	-	-	
2-z2	0.60	-	-	-	-	-	-	
2-z3	0.67	-	-	-	-	-	-	
2-z4*	0.67	17.5%	11.8%	1.75	87.26	87.26	2.09	4.11 & 4.12
2-x1*	0.67	17.5%	11.8%	1.78	89.20	89.20	2.10	4.13 & 4.14
2-y1*	0.37	17.5%	11.8%	2.70	135.06	135.06	2.29	4.15 & 4.16
3-y1*	0.10	12.2%	5.8%	6.19	309.43	309.43	2.02	4.17 & 4.18
4-y1*	0.87	14.2%	12.0%	2.27	68.00	68.00	1.99	4.19 & 4.20
4-x1*	0.22	14.2%	12.0%	2.74	82.16	82.16	2.08	4.21 & 4.22

Formation Resistivity Factor, F; Cementation Exponent, m;
*Models are plotted and further explained in the referenced Figures.

Similar permeabilities in orthogonal flow directions indicate that the Midale Marly KD-03-18 subsample is nearly isotropic.

A summary of the computational model settings used for computing the simulations is shown in Table 4.3. The times required to complete the simulations were recorded. This time does not include time allocated for mesh generation. For complex mesh cases, the 3D mesh generation computation took longer than the simulation time. All simulations were completed using COMSOL 4.3. The relative repair tolerance for the STL file was 10^{-6} for all simulations. The number of equations listed in Table 4.3 correspond to the Navier-Stokes and Laplace PDE solutions.

Table 4.3 Computational results for the KD-18-03 Subsample

Model	Equations (#)	Time (min)	RAM (GB)	Error (%)	Mesh Setting	Figures
1-y1	56,536	1.2	4.7	23.0	Boundary Layer	-
1-y2	86,176	1.2	4.6	13.8	Boundary Layer	-
1-y3	198,672	1.9	4.8	11.1	Boundary Layer	-
1-y4	772,704	6.5	7.7	3.1	Boundary Layer	-
1-y5*	4,332,920	28.7	23.8	1.7	Boundary Layer	4.5 & 4.6
1-z1	56,636	0.9	4.6	24.6	Boundary Layer	-
1-z2	86,176	1.0	4.7	14.8	Boundary Layer	-
1-z3	198,672	1.6	5.1	8.7	Boundary Layer	-
1-z4	772,704	5.5	7.3	3.4	Boundary Layer	-
1-z5*	4,332,920	28.1	23.9	2.0	Boundary Layer	4.7 & 4.8
1-x5*	4,332,920	27.3	24.0	0.9	Boundary Layer	4.9 & 4.10
2-z1	156,364	5.3	6.0	-	Boundary Layer	-
2-z2	621,152	8.0	7.0	-	Boundary Layer	-
2-z3	678,804	9.2	7.0	-	Boundary Layer	-
2-z4*	1,899,423	198.6	18.0	3.8	Boundary Layer	4.11 & 4.12
2-x1*	1,899,423	152.4	18.0	8.3	Boundary Layer	4.13 & 4.14
2-y1*	1,899,423	137.6	18.3	5.9	Boundary Layer	4.15 & 4.16
3-y1*	5,061,699	35.1	24.0	0.2	Free Tetrahedral	4.17 & 4.18
4-y1*	1,158,653	6.6	8.2	0.5	Free Tetrahedral	4.19 & 4.20
4-x1*	1,158,653	6.5	8.6	0.1	Free Tetrahedral	4.21 & 4.22

*Models are plotted and further explained in the referenced figures.

Random Access Memory, RAM;

Models 1 and 2 used a multigrid iterative solution and a coupled iterative solution

Models 3 to 4 used a coupled iterative solution

Table 4.4 shows the results for permeability, formation resistivity factor and cementation exponent. The new calculated results for the KD-03-18 Marly (M0) subsample vary by less than one order of magnitude and are similar to the experimentally derived values of Glemser (2007).

Table 4.4 Results for Permeability, Formation Resistivity Factor and Cementation Exponent

	Permeability (mD)	Formation Resistivity Factor	Cementation Exponent
Marly Dolostones*	1-150	-	-
Ruska Liquid Permeameter**	7.7	-	-
CMT**	7.73	11.71	1.87
CMT (this study)	0.1 to 3.53	29.3 to 309.43	1.99 to 2.10

*from Churcher, et al. (1994); Glemser (2007)

**from Glemser (2007)

The permeability, formation resistivity factor and cementation exponent were calculated in this study using the natural geometry of the CMT data and the 3D Navier Stokes Equations. The calculated permeability ranges from 0.1 to 3.53 mD as shown in Table 4.2. The formation resistivity factor ranges from 29.3 to 309.43 and the cementation exponent ranges from 1.99 to 2.10.

The cementation exponent can also be calculated using all of the data from the slope of the best fitting line through a plot of the log of the formation factor vs. the log of the effective porosity (Figure 4.2). This method does not require the assumption that $a=1$. All of the formation resistivity factor data and effective porosity data in Table 4.2 were used to calculate the cementation exponent. The red dot, in Figure 4.2, represents the formation resistivity factor and porosity calculated by Glemser (2007). This plot is shown in Figure 4.2.

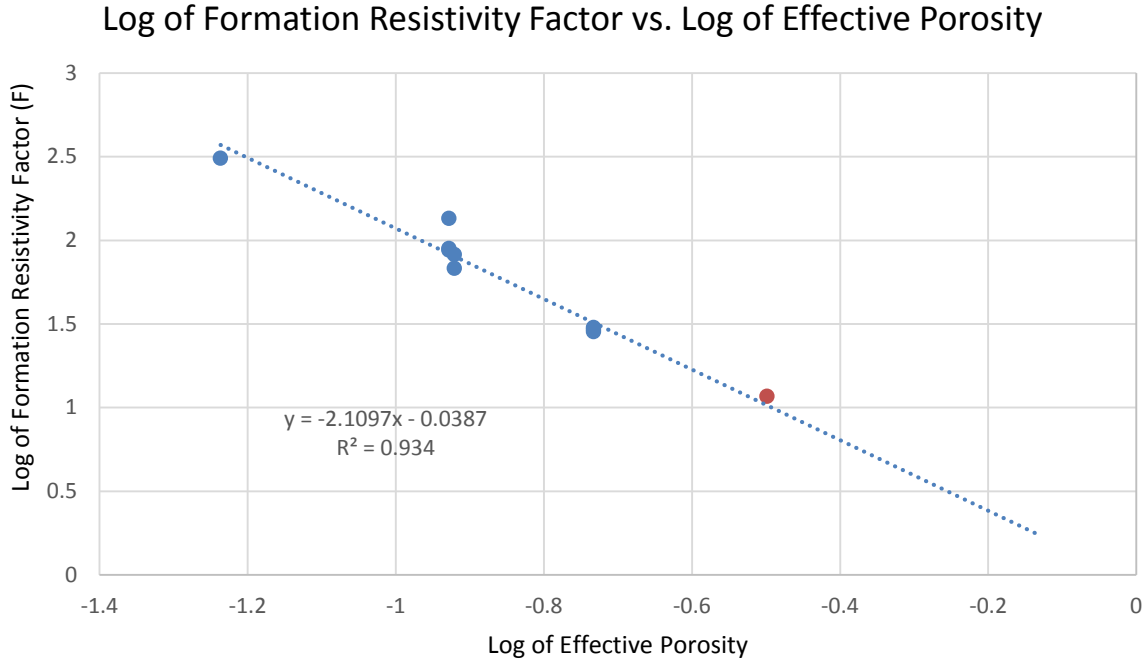


Figure 4.2 Log of Formation Resistivity Factor (F) vs. Log of Effective Porosity (%)

The cementation exponent, also the slope of the line, in Figure 4.2, is calculated to be $m = 2.11$. The cementation exponent was estimated by Glemser (2007), using equation 1.5, to be $m = 1.87$. Considering that I completed simulations on some smaller subsamples, due to finite computer memory available, comparison between the cementation exponent results are reasonably close.

The extrapolated linear trend line is close to Glemser's (2007) formation resistivity factor of 11.71. The equation of the trend line was used with an effective porosity of 31.7% to calculate a formation resistivity factor of 10.32.

The value of 'a' can be calculated using Archie's Law, as shown in Equation 1.7. Table 4.5 shows the calculated value of 'a' using the total and effective porosity.

Table 4.5 Archie's Law calculation of 'a' for the KD-18-03 Subsample

Model	Total Porosity (%)	Effective Porosity (%)	Formation Factor (F)	Cementation Exponent (m)	a_{total}	$a_{effective}$
1-y5	19.7%	18.5%	29.3	2.00	1.14	1.00
1-z5	19.7%	18.5%	30.1	2.02	1.13	1.00
1-x5	19.7%	18.5%	28.4	1.98	1.14	1.01
2-z4	17.5%	11.8%	87.26	2.09	2.28	1.00
2-x1	17.5%	11.8%	89.20	2.10	2.90	1.00
2-y1	17.5%	11.8%	135.06	2.29	2.50	1.01
3-y1	12.2%	5.8%	309.43	2.02	4.42	0.98
4-y1	14.2%	12.0%	68.00	1.99	1.40	1.00
4-x1	14.2%	12.0%	82.16	2.08	1.42	1.00

The values of a_{total} , calculated using the total porosity, ranges from 1.13 to 4.42. Using the effective porosity, the values of $a_{effective}$ ranges from 0.98 to 1.01. The values of $a_{effective}$ are close to the estimated value of 'a' = 1.00. Using the effective porosity gives a closer value to the '1' expected as the fluid flow is dominant in this region only.

A table of common values of the common cementation are provided in Table 4.6 (Doveton, 1999).

Table 4.6 Common cementation exponent 'm' values

Rock Type	Cementation Exponent (m)
Intergranular/intercrystalline	2.0
Fractures	1.4
Vugs	2.3
Moldic	3+

From (Doveton, 1999)

The Marly is characterized by intercrystalline porosity with a fairly uniform pore space (Wegelin, 1984). The calculated cementation exponent ranges from 1.98 to 2.29 as provided in Table 4.5.

The log of permeability vs. the log of porosity is shown in Figure 4.3.

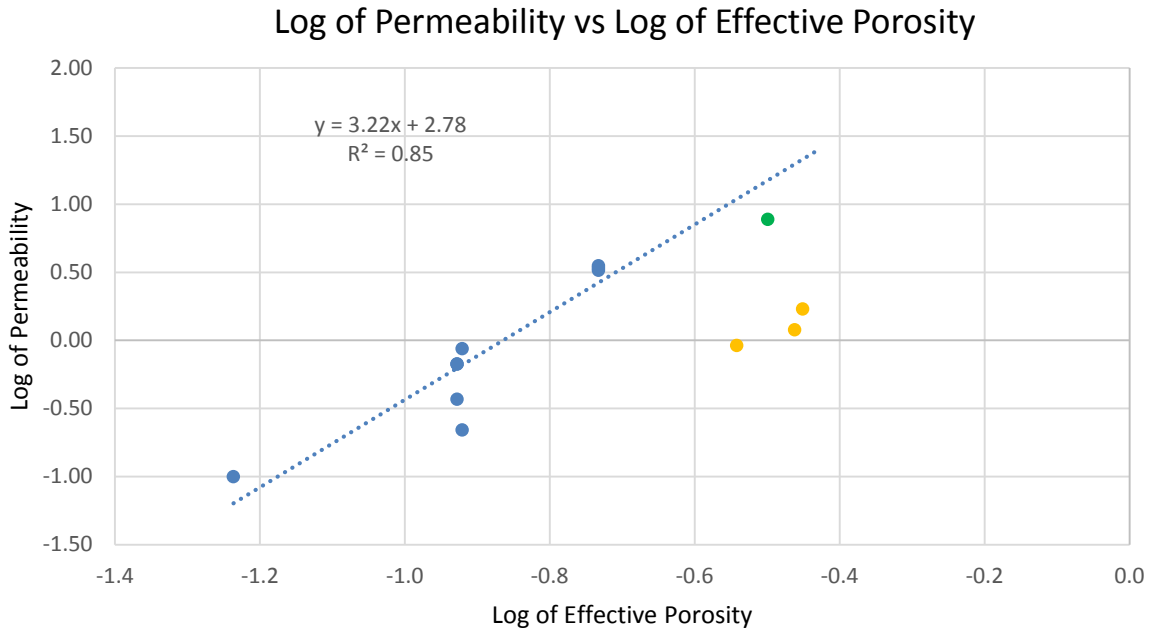


Figure 4.3 Log of Permeability (mD) vs. Log of Porosity (%)

The KD-18-03 Marly sample gives a slope of 3.22. The extrapolated linear trend line is close to Glemser’s (2007) permeability of 7.77 mD. This permeability is shown as a green dot in Figure 4.3. The equation of the trend line was used with an effective porosity of 31.7% to calculate a permeability of 15.0 mD. The yellow dots represent permeability and porosity results using a Marly (M3) rock (Carroll et al., 2011). This rock will be discussed in section 4.3. The equation of the trend line is a power law as predicted by the Kozeny-Carmen equation. The slope value of ‘3’ is reasonable for permeability-porosity relations as the typical predicted slope ranges from 1 to 3, although higher values have been suggested (Wark et al., 1998). I have captured the statistical nature of the sample as the trend line fit with the results completed by Glemser (2007).

A visual indication of the how the fluid flow and current density diagrams are displayed is represented in Figure 4.4. The flow is viewed from outside to inside the box with the colors showing the 3D isotropic view relative to the 2D views.

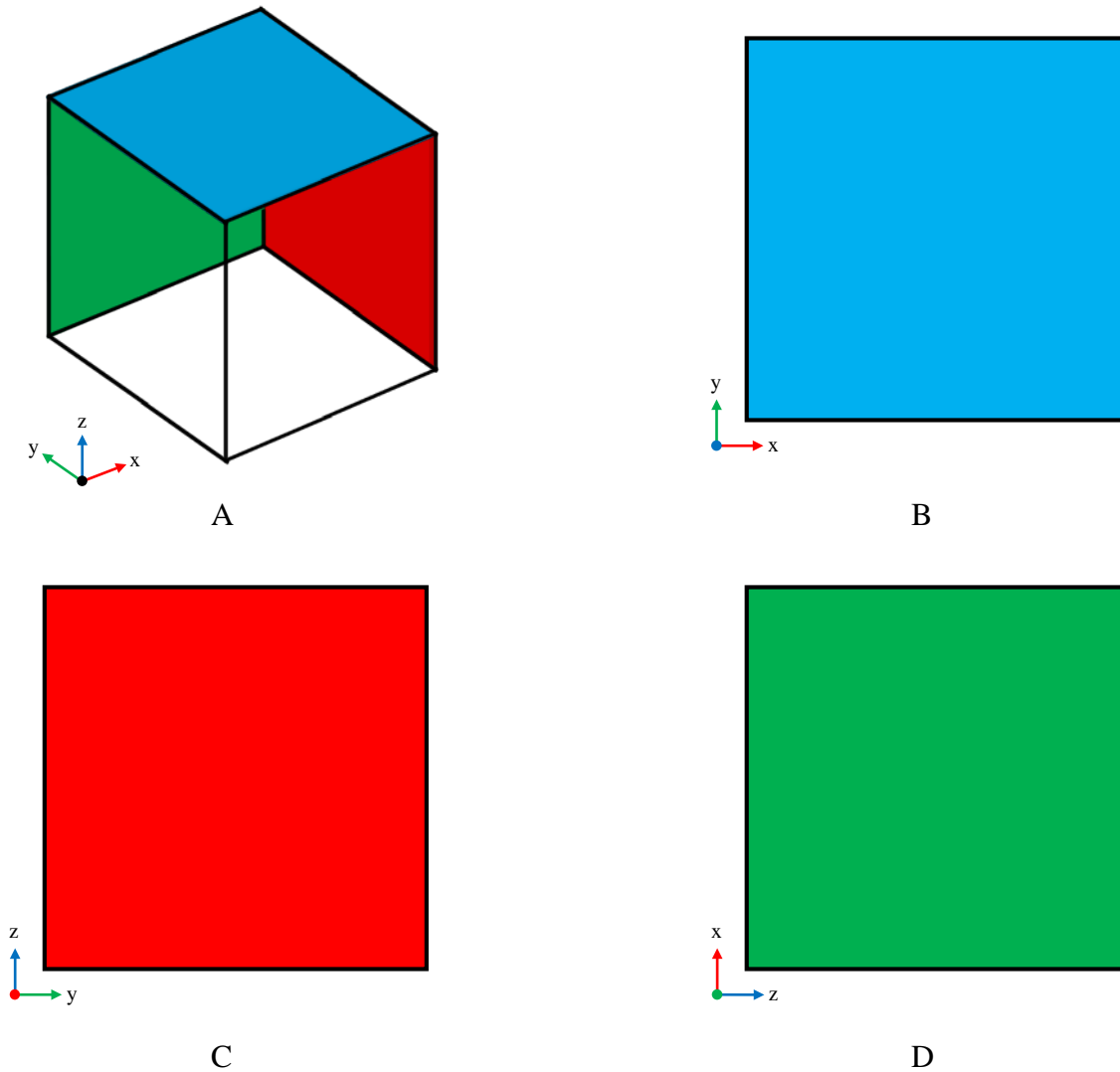


Figure 4.4 Reference figure used to display the representative views of Figures 4.5 to 4.22 (A) 3D orthographic view (B) 2D view looking in the z- direction (view of outside face looking inside). (C) 2D view looking in the x- direction (view of outside face looking inside). (D) 2D view looking in the y- direction (view of outside face looking inside). (B,C,D) All views show 2D a view looking from outside the 2D face to inside the 3D cube.

[Model 1] to [Model 4] used 0.78 μm CMT resolution data. For the flow diagrams, streamlines of the velocity field were used with the streamline color representing the velocity magnitude. The surface mesh, representing the boundary of the pore space and rock matrix, is displayed in grey to highlight the fluid flow and electrical current density patterns. For the electrical current density diagrams, streamlines represent the electrical current density and the color is the electrical current density magnitude.

To help visualize the velocity magnitude changes within the same Model, the range on the color bar was kept constant for the figures presented. All samples were verified to be nearly isotropic as the permeability was within the same order of magnitude for three orthogonal fluid flow directions.

The solutions quantitatively determine that the fluid pathways that produce the greatest fluid velocities are located in the smallest connected voxel regions. It is expected that the fluid velocities are the greatest in the smallest pore throats.

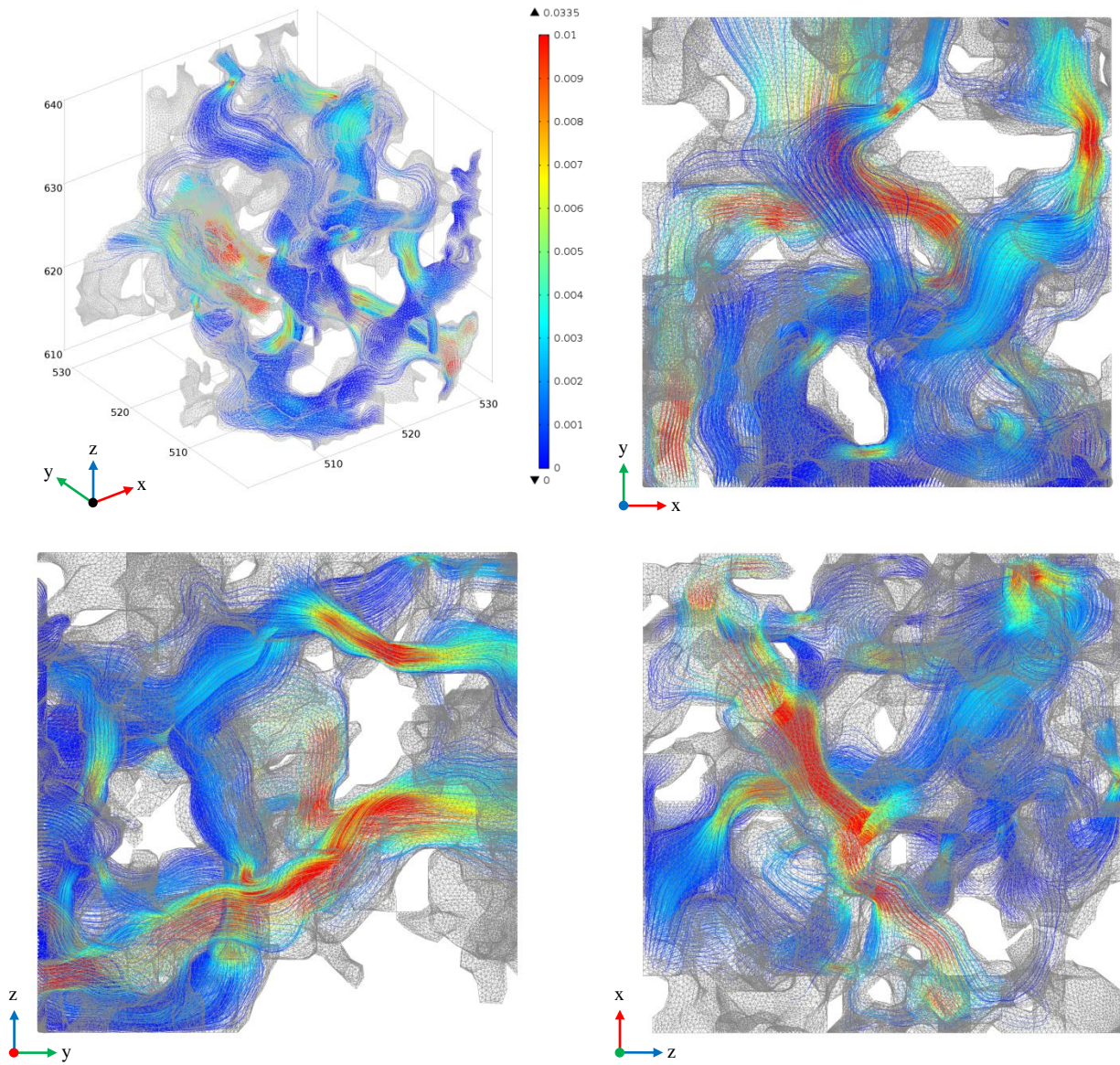


Figure 4.5 Flow diagrams from KD-18-03 subsample (Model 1-y5).

Image parameters for Model 1-y5 are as follows:

CMT Resolution: $0.78 \mu\text{m}$

Subsample size: $(30 \text{ voxel})^3$, $(23.4 \mu\text{m})^3$ (x,y,z crop coordinates are: 500:530; 500:530; 0:30).

Streamline: Velocity field (used 5,000 points, inlet controlled).

Streamline color: Velocity Magnitude, normalized from blue (min. ~ 0) to red (0.01 voxel/s).

Mesh: Surface mesh displayed in grey.

Flow: Entering from the front xz face and flowing in the y+ direction.

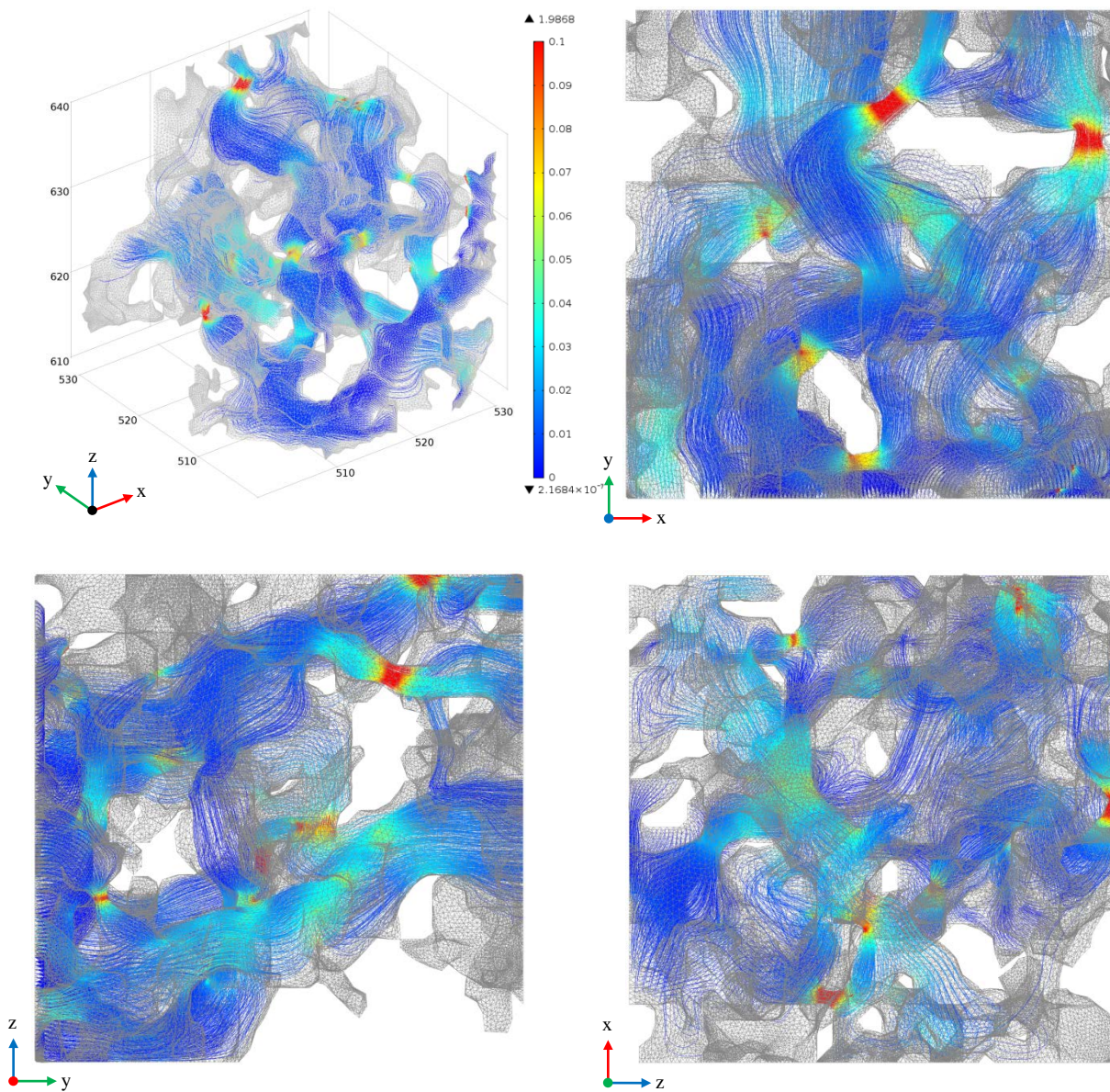


Figure 4.6 Electrical current density diagrams from KD-18-03 subsample (Model 1-y5).

Image parameters for Model 1-y5 are as follows:

CMT Resolution: $0.78 \mu\text{m}$

Subsample size: $(30 \text{ voxel})^3$, $(23.4 \mu\text{m})^3$ (x,y,z crop coordinates are: 500:530; 500:530; 0:30).

Streamline: Current density (used 5,000 points, inlet controlled).

Streamline color: Current Density Magnitude, normalized from blue (min. ~ 0) to red (0.01 A/vox^2).

Mesh: Surface mesh displayed in grey.

Voltage: Entering from the front xz face and flowing in the y+ direction.

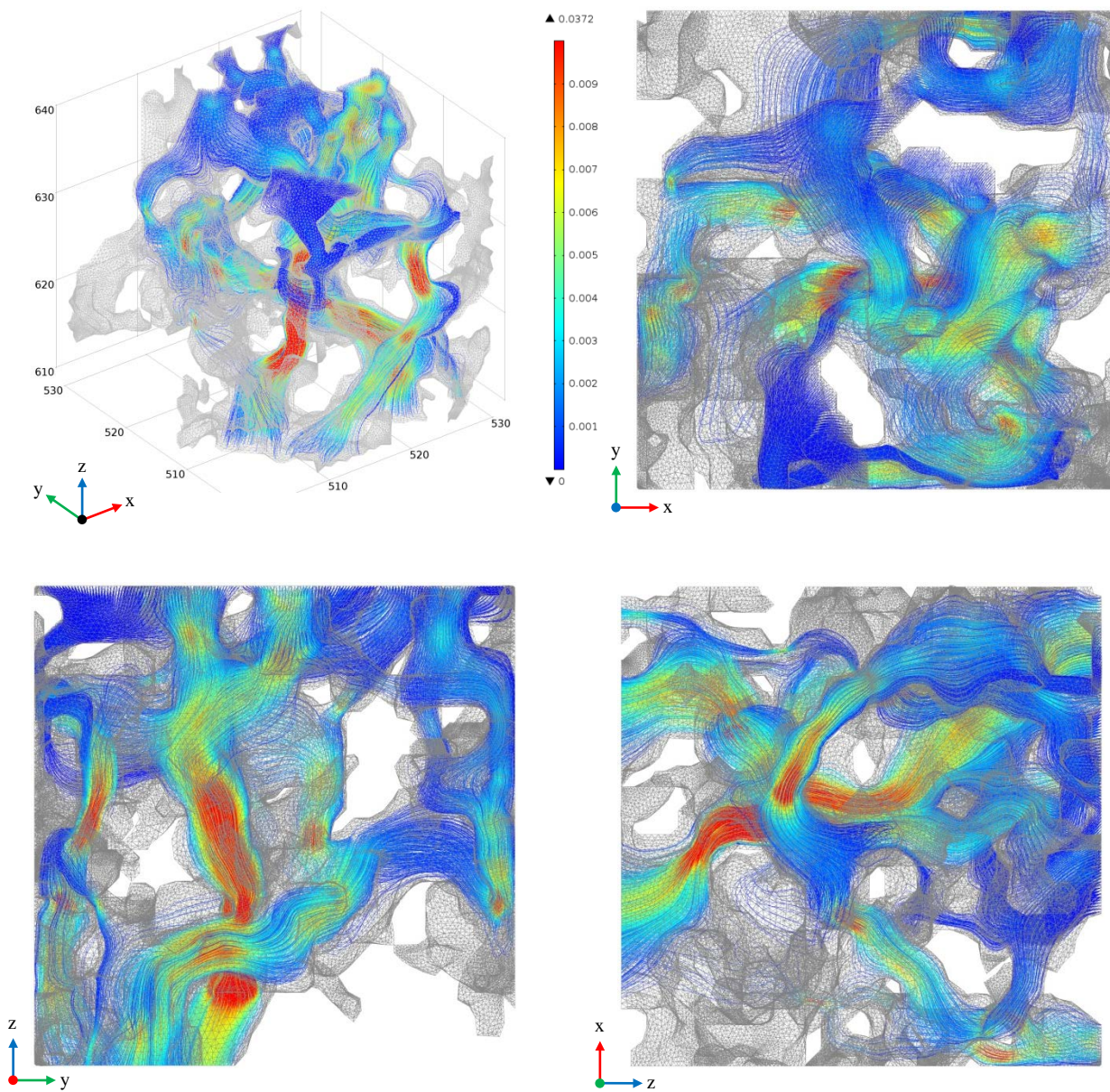


Figure 4.7 Flow diagrams from KD-18-03 subsample (Model 1-z5).

Image parameters for Model 1-z5 are as follows:

CMT Resolution: $0.78 \mu\text{m}$

Subsample size: $(30 \text{ voxel})^3$, $(23.4 \mu\text{m})^3$ (x,y,z crop coordinates are: 500:530; 500:530; 0:30).

Streamline: Velocity field (used 5,000 points, inlet controlled).

Streamline color: Velocity Magnitude, normalized from blue (min. ~ 0) to red (0.01 voxel/s).

Mesh: Surface mesh displayed in grey.

Flow: Entering from the top xy face and flowing in the z- direction.

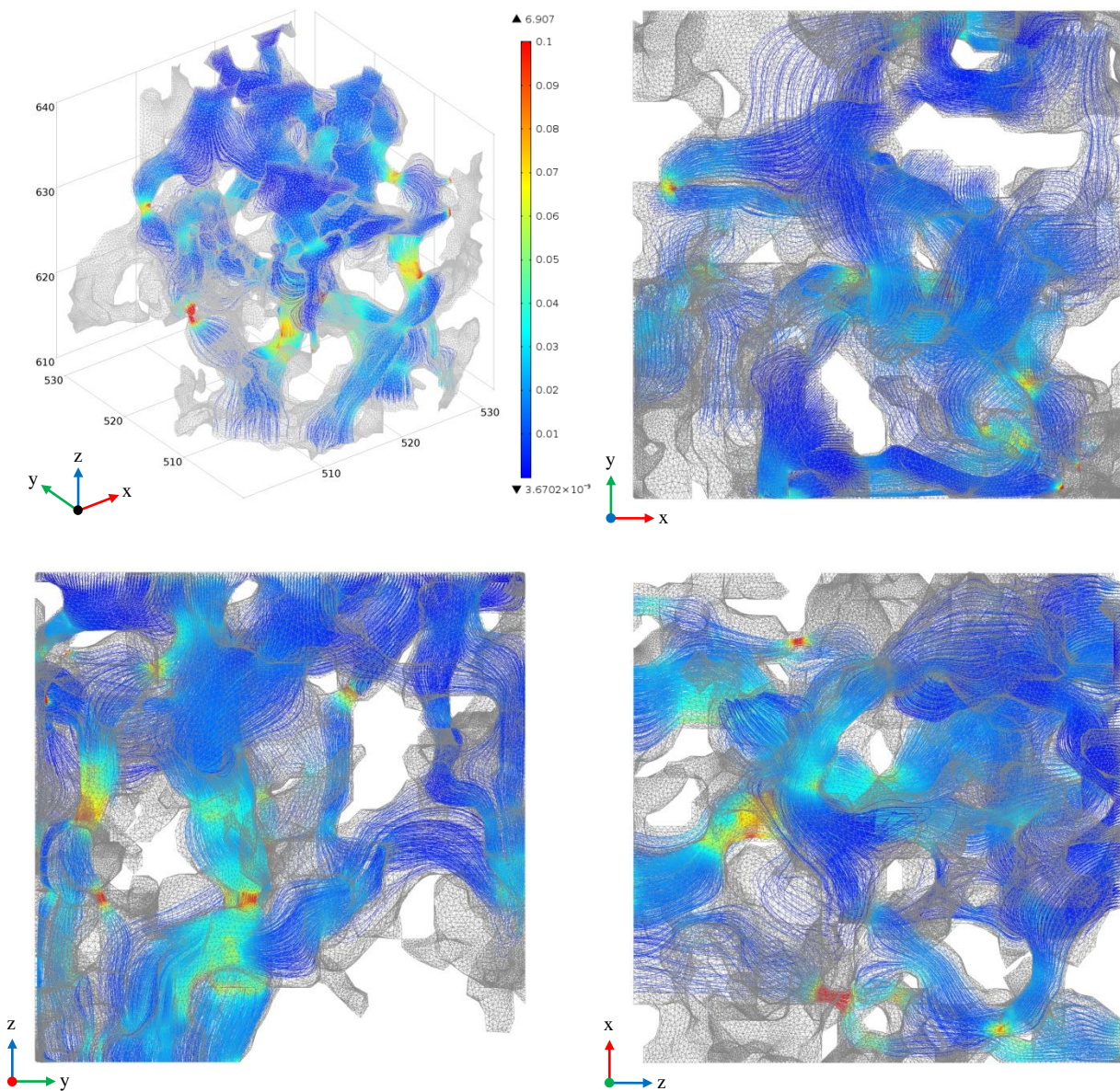


Figure 4.8 Electrical current density diagrams from KD-18-03 subsample (Model 1-z5).

Image parameters for Model 1-z5 are as follows:

CMT Resolution: $0.78 \mu\text{m}$

Subsample size: $(30 \text{ voxel})^3$, $(23.4 \mu\text{m})^3$ (x,y,z crop coordinates are: 500:530; 500:530; 0:30).

Streamline: Current density (used 5,000 points, inlet controlled).

Streamline color: Current Density Magnitude, normalized from blue (min. ~ 0) to red (0.01 A/vox^2).

Mesh: Surface mesh displayed in grey.

Voltage: Entering from the top xy face and flowing in the z- direction.

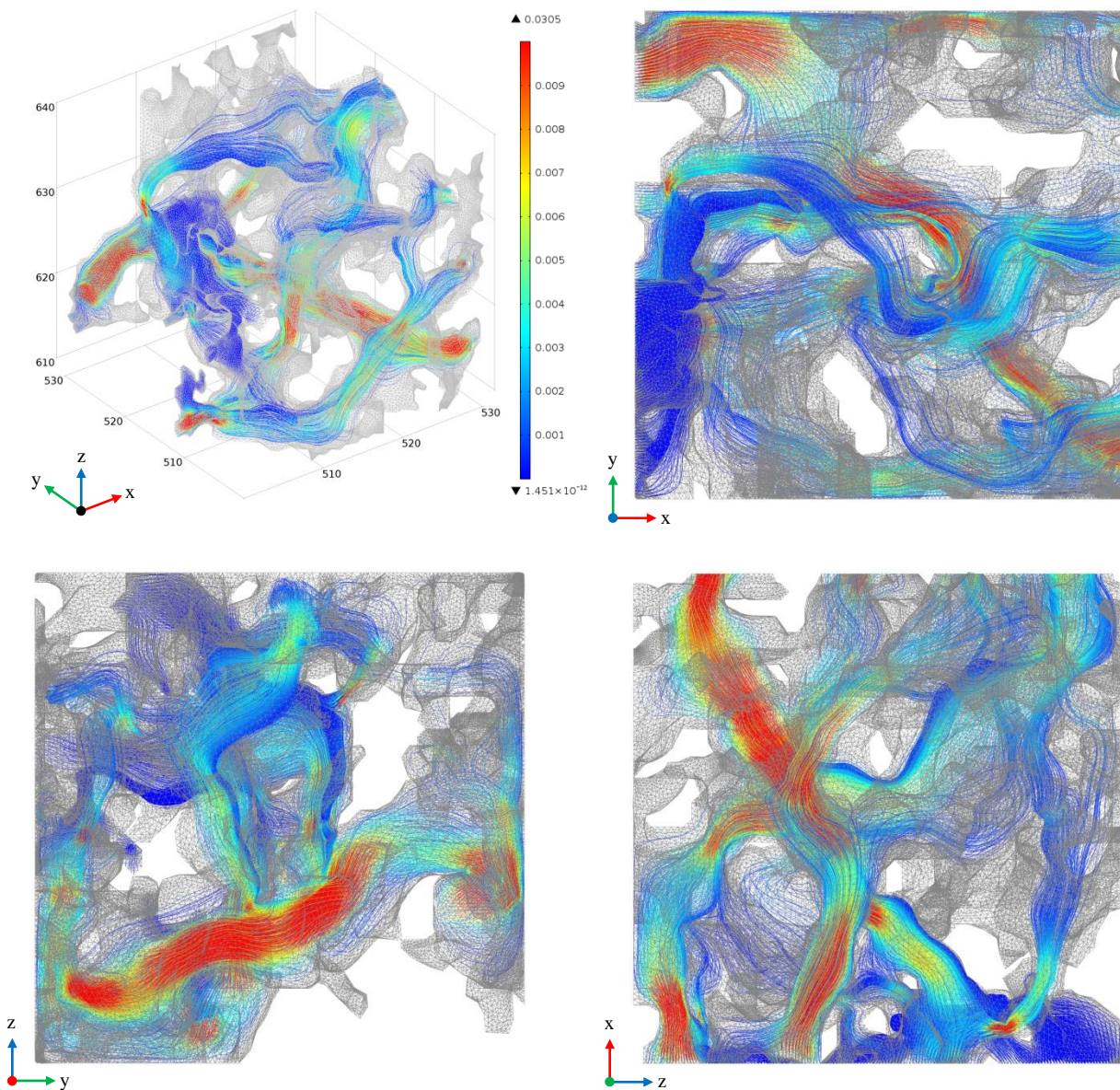


Figure 4.9 Flow diagrams from KD-18-03 subsample (Model 1-x5).

CMT Resolution: $0.78 \mu\text{m}$

Subsample size: $(30 \text{ voxel})^3$, $(23.4 \mu\text{m})^3$ (x,y,z crop coordinates are: 500:530; 500:530; 0:30).

Streamline: Velocity field (used 5,000 points, inlet controlled).

Streamline color: Velocity Magnitude, normalized from blue (min. ~ 0) to red (0.01 voxel/s).

Mesh: Surface mesh displayed in grey.

Flow: Entering from the left yz face and exiting in the x+ direction.

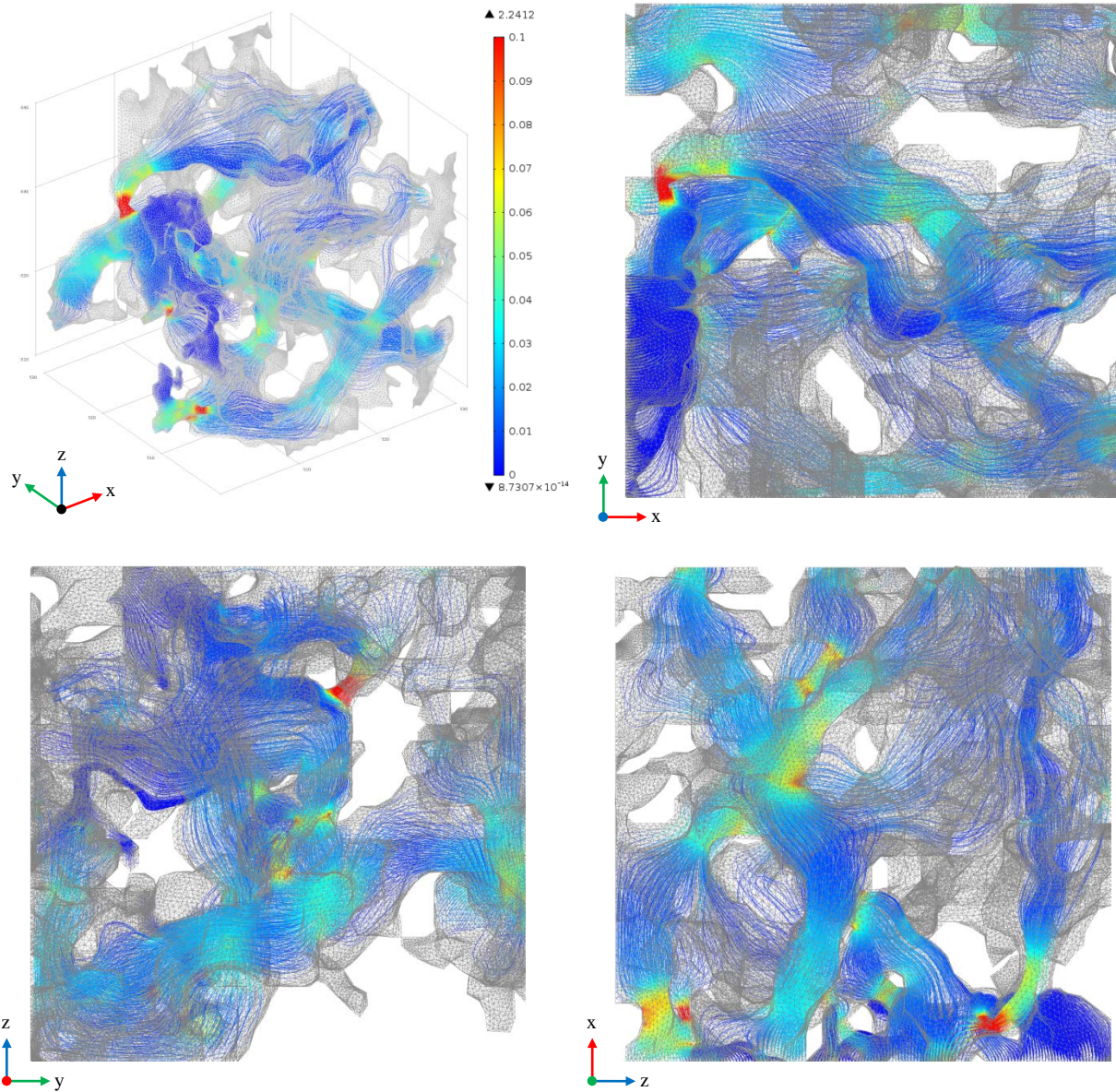


Figure 4.10 Electrical current density diagrams from KD-18-03 subsample (Model 1-x5).

Image parameters for Model 1-x5 are as follows:

CMT Resolution: $0.78 \mu\text{m}$

Subsample size: $(30 \text{ voxel})^3$, $(23.4 \mu\text{m})^3$ (x,y,z crop coordinates are: 500:530; 500:530; 0:30).

Streamline: Current density (used 5,000 points, inlet controlled).

Streamline color: Current Density Magnitude, normalized from blue (min. ~ 0) to red (0.01 A/vox^2).

Mesh: Surface mesh displayed in grey.

Voltage: Entering from the left yz face and flowing in the x+ direction.

[Model 1] utilized a sub-volume sample size $23.4^3 \mu\text{m}^3$ (30^3 voxel^3) as shown in Figure 4.5 through Figure 4.10. The streamlines of the velocity field are illustrations of fluid flow for the steady state incompressible Navier Stokes equations using a no slip boundary condition. The gradient of the velocity across a pore is an indication of the viscous drag along the walls of the rock pore matrix. The streamlines of the current density are illustrations of electrical current flow direction for Laplace's equation using electrical insulation on the walls. The solution to Laplace's equation, for electrical current density, doesn't exhibit the drag effect on the wall, so the pore gradients of current density are greatly reduced compared with flow velocity. For regions of smaller pore constrictions, and subsequent higher velocity regions, the comparison between the fluid flow and electrical current density diagrams illustrate this phenomenon.

As listed in Table 4.2, flow in all orthogonal directions resulted in permeabilities of 3.53 mD, 3.27 mD, and 3.40 mD for the x-direction, y-direction and z-direction. The sample is nearly isotropic. The total porosity is 19.7% with an effective porosity of 18.5%. This indicated that most of the pore space is connected in this subsample for the $0.78 \mu\text{m}$ CMT resolution. The formation factor and cementation exponent ranged from 28.4 to 29.3 and from 1.98 to 2.02 respectively. The velocity magnitude color scale was restricted from ~ 0 to 0.01 voxel/s and the electrical current density magnitude color scale was restricted from ~ 0 to 0.01 A/vox².

Geometry modifications, using manual face partitioning in COMSOL, were also completed for [Model 1] simulations. This included adjusting the maximum angle in the face, maximum face neighbor angle, minimum relative area and removal of small faces. After completing manual fixes, COMSOL was able to import the STL triangular surface representation and generate a 3D mesh without internal geometry errors. This process typically took several hours for most samples; however, this process took approximately two weeks for [Model 1].

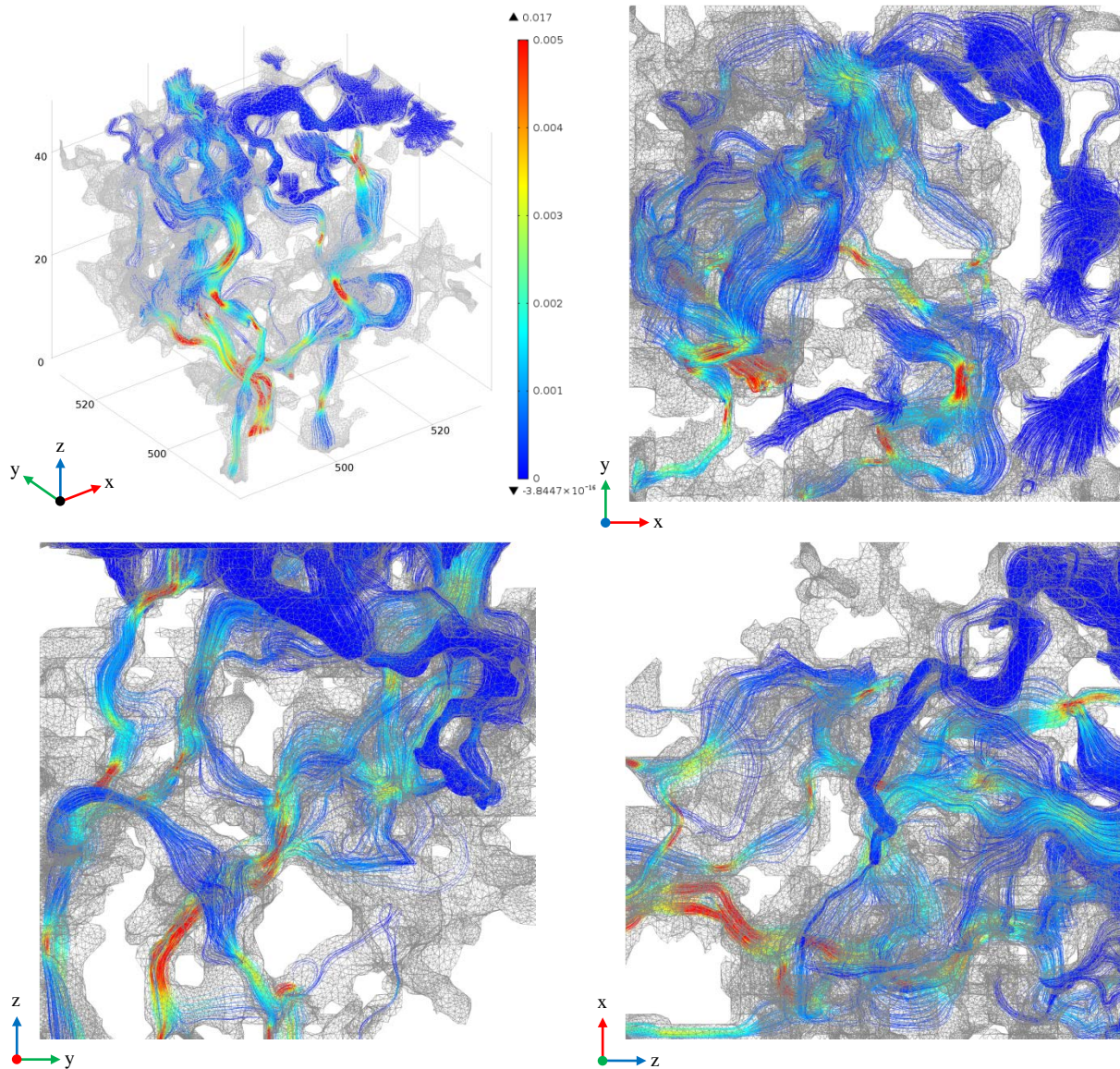


Figure 4.11 Flow diagrams from KD-18-03 subsample (Model 2-z4).

Image parameters for Model 2-z4 are as follows:

CMT Resolution: 0.78 μm

Subsample size: (50 voxel)³, (39.0 μm)³ (x,y,z crop coordinates are: 480:530; 480:530; 0:50).

Streamline: Velocity field (used 5,000 points, inlet controlled).

Streamline color: Velocity Magnitude, normalized from blue (min. ~ 0) to red (0.01 voxel/s).

Mesh: Surface mesh displayed in grey.

Flow: Entering from the top xy face and exiting in the z- direction.

Note: 18 GB of RAM used plus 39 GB of virtual memory used in simulation.

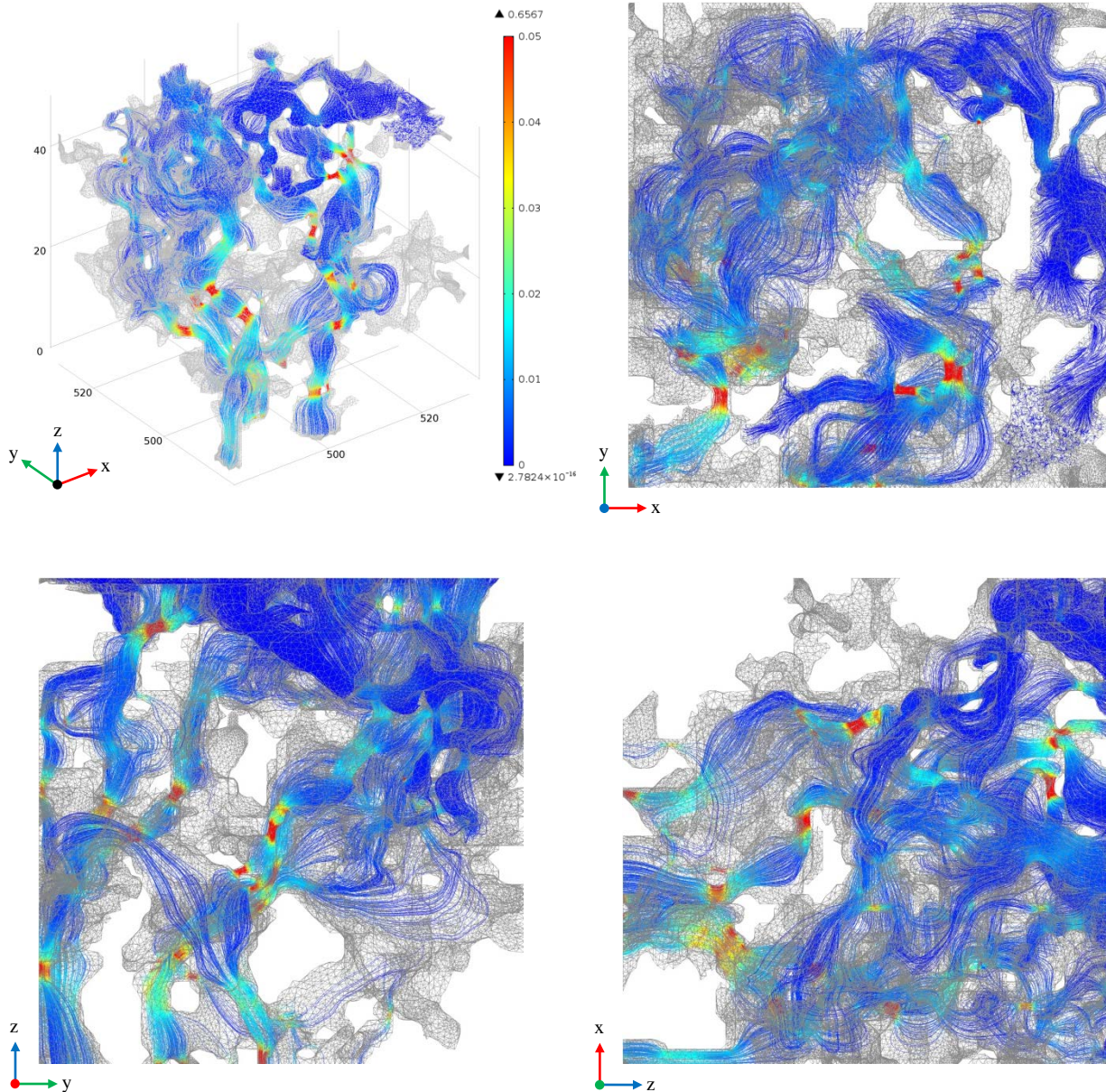


Figure 4.12 Electrical current density diagrams from KD-18-03 subsample (Model 2-z4).

Image parameters for Model 2-z4 are as follows:

CMT Resolution: $0.78 \mu\text{m}$

Subsample size: $(50 \text{ voxel})^3$, $(39.0 \mu\text{m})^3$ (x,y,z crop coordinates are: 480:530; 480:530; 0:50).

Streamline: Current density (used 5,000 points, inlet controlled).

Streamline color: Current Density Magnitude, normalized from blue (min. ~ 0) to red (0.01 A/vox^2).

Mesh: Surface mesh displayed in grey.

Voltage: Entering from the top xy face and exiting in the z- direction.

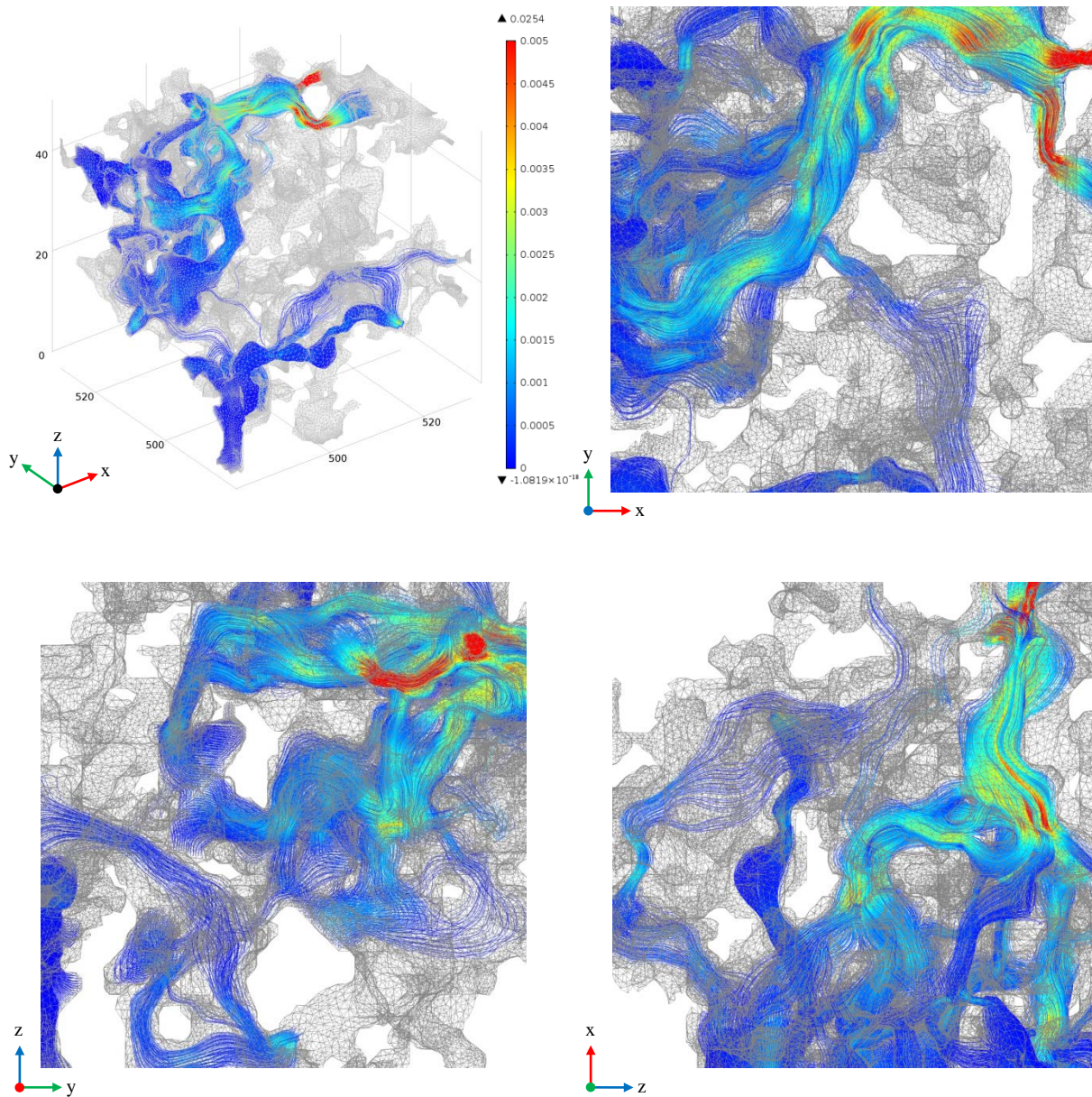


Figure 4.13 Flow diagrams from KD-18-03 subsample (Model 2-x1).

Image parameters for Model 2-x1 are as follows:

CMT Resolution: $0.78 \mu\text{m}$

Subsample size: $(50 \text{ voxel})^3$, $(39.0 \mu\text{m})^3$ (x,y,z crop coordinates are: 480:530; 480:530; 0:50).

Streamline: Velocity field (used 5,000 points, inlet controlled).

Streamline color: Velocity Magnitude, normalized from blue (min. ~ 0) to red (0.01 voxel/s).

Mesh: Surface mesh displayed in grey.

Flow: Entering from the left yz face and exiting in the x+ direction.

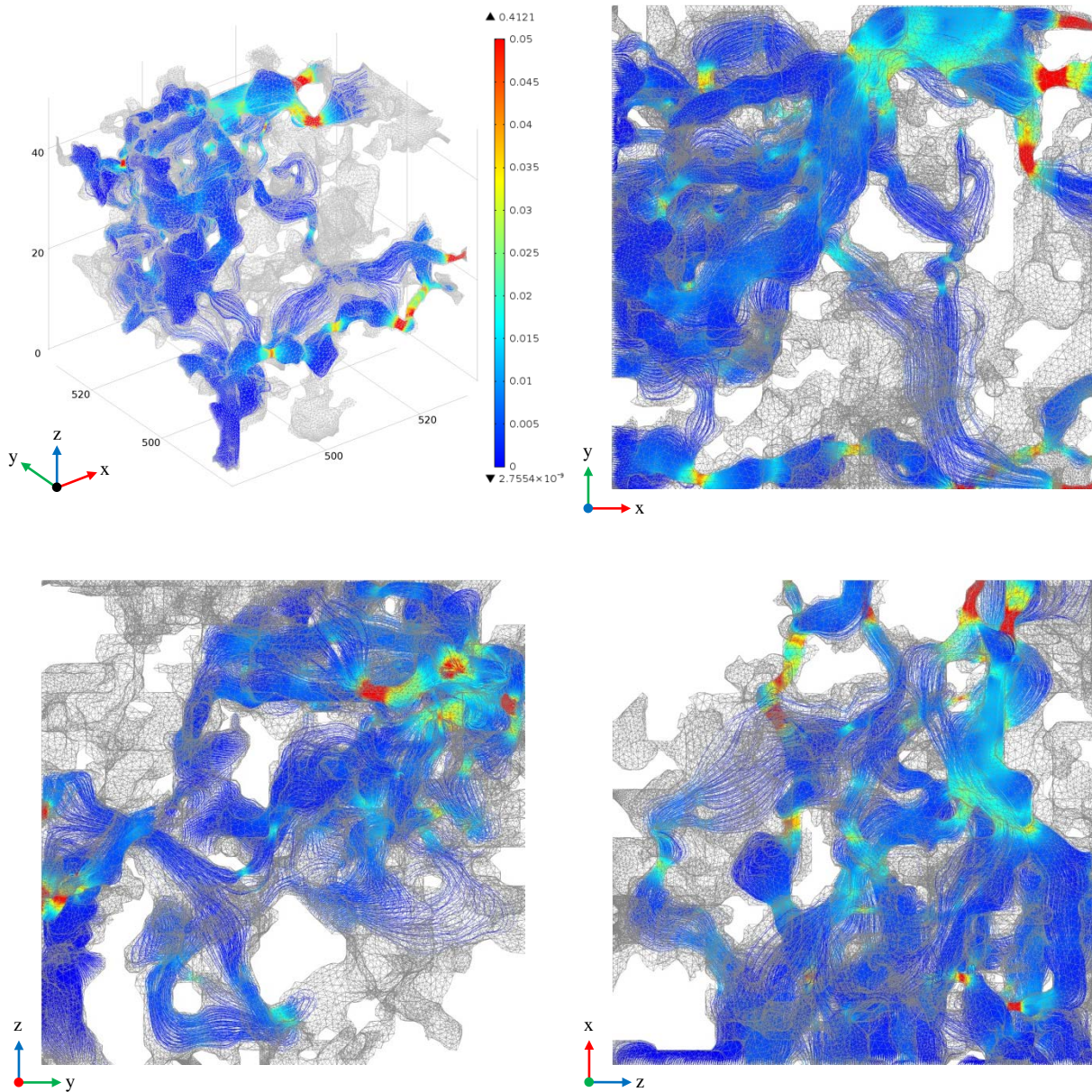


Figure 4.14 Electrical current diagrams from KD-18-03 subsample (Model 2-x1).

Image parameters for Model 2-x1 are as follows:

CMT Resolution: $0.78 \mu\text{m}$

Subsample size: $(50 \text{ voxel})^3$, $(39.0 \mu\text{m})^3$ (x,y,z crop coordinates are: 480:530; 480:530; 0:50).

Streamline: Current density (used 5,000 points, inlet controlled).

Streamline color: Current Density Magnitude, normalized from blue (min. ~ 0) to red (0.01 A/vox²).

Mesh: Surface mesh displayed in grey.

Voltage: Entering from the top xy face and exiting in the z- direction.

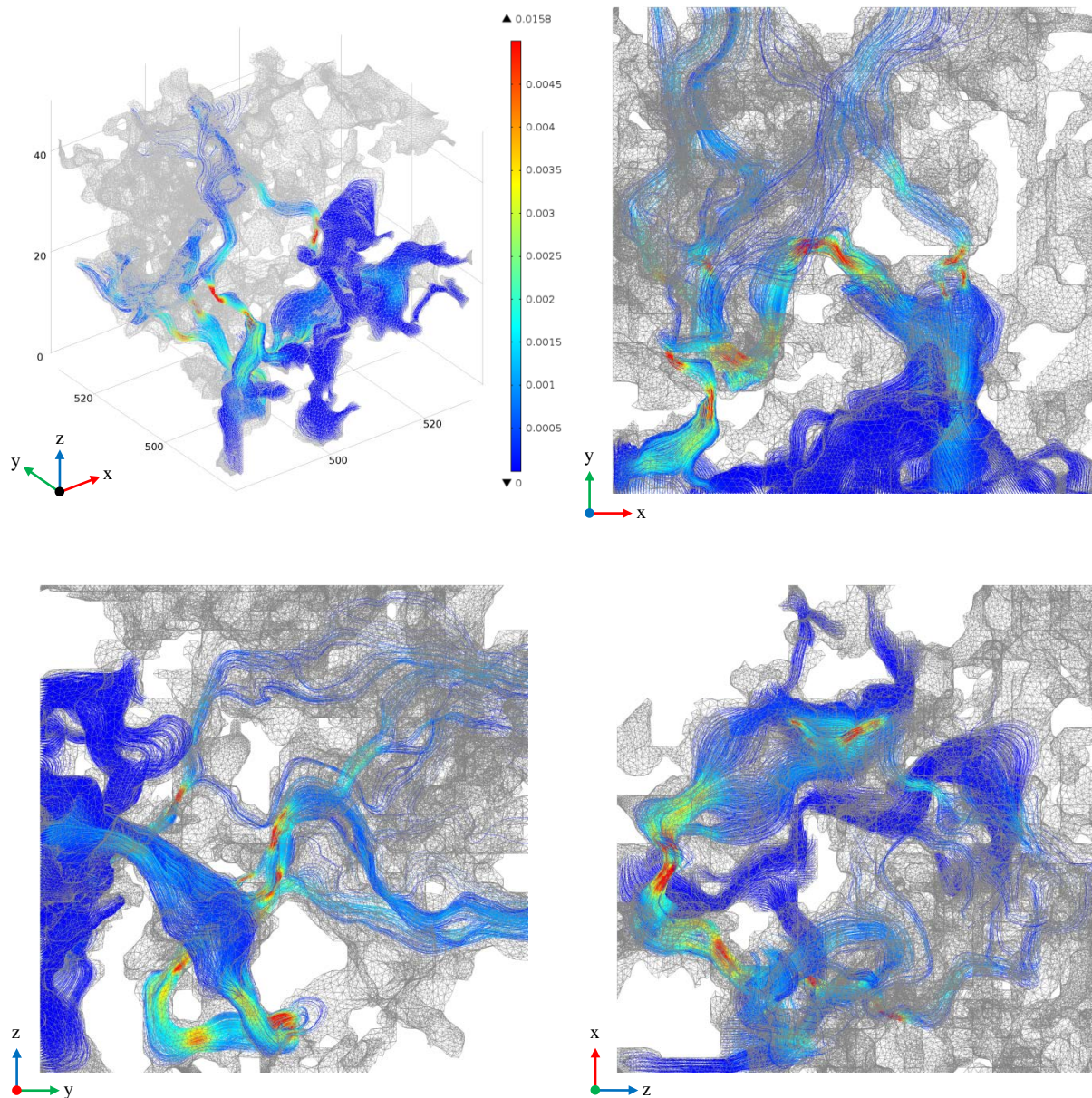


Figure 4.15 Flow diagrams from KD-18-03 subsample (Model 2-y1).

Image parameters for Model 2-y1 are as follows:

CMT Resolution: $0.78 \mu\text{m}$

Subsample size: $(50 \text{ voxel})^3$, $(39.0 \mu\text{m})^3$ (x,y,z crop coordinates are: 480:530; 480:530; 0:50).

Streamline: Velocity field (used 5,000 points, inlet controlled).

Streamline color: Velocity Magnitude, normalized from blue (min. ~ 0) to red (0.01 voxel/s).

Mesh: Surface mesh displayed in grey.

Flow: Entering from the front xz face and exiting in the y+ direction.

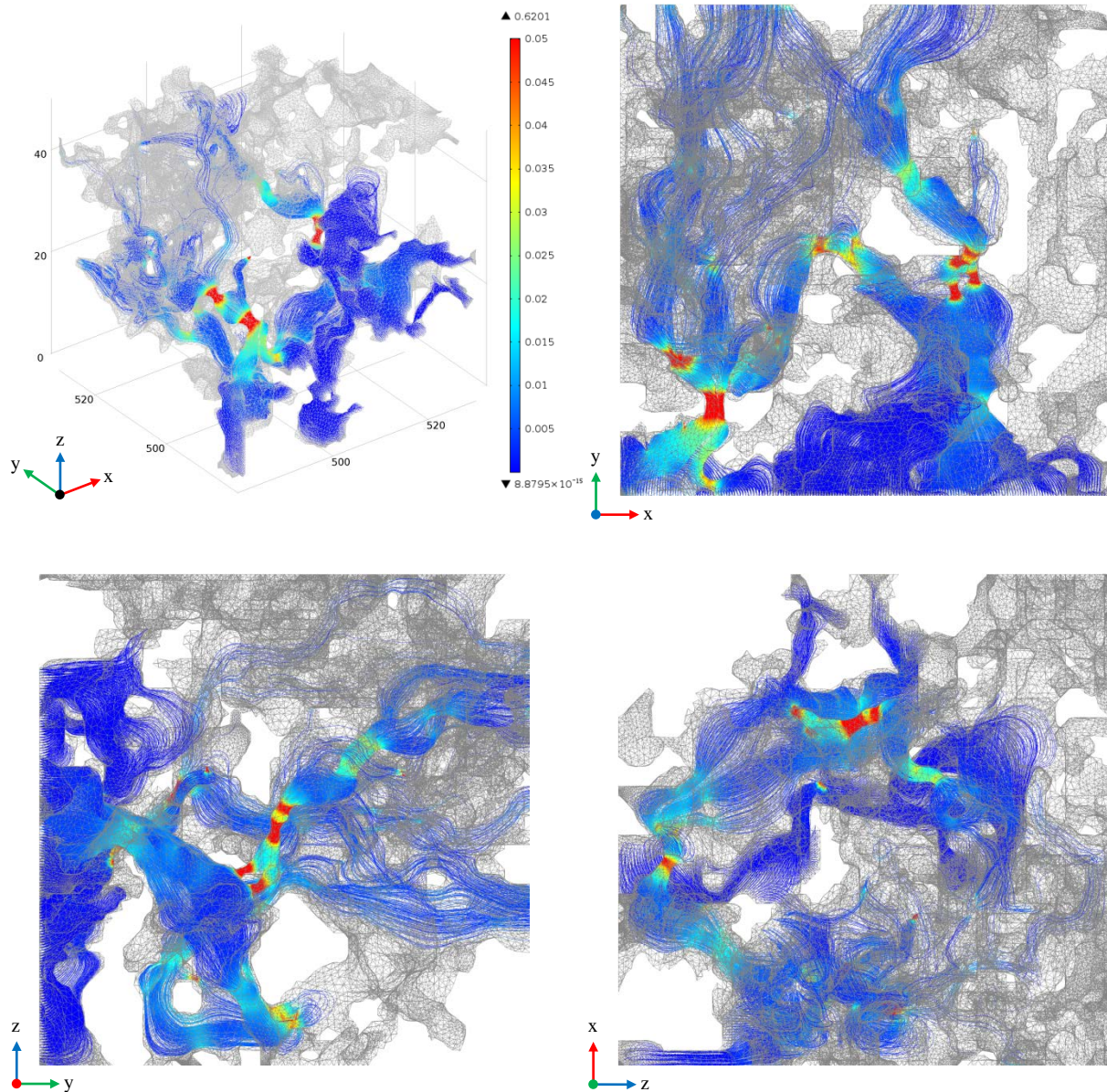


Figure 4.16 Electrical current density diagrams from KD-18-03 subsample (Model 2-y1).

Image parameters for Model 2-y1 are as follows:

CMT Resolution: $0.78 \mu\text{m}$

Subsample size: $(50 \text{ voxel})^3$, $(39.0 \mu\text{m})^3$ (x,y,z crop coordinates are: 480:530; 480:530; 0:50).

Streamline: Current density (used 5,000 points, inlet controlled).

Streamline color: Current Density Magnitude, normalized from blue (min. ~ 0) to red (0.01 A/vox^2).

Mesh: Surface mesh displayed in grey.

Voltage: Entering from the front xz face and exiting in the y+ direction.

[Model 2] is a $39.0^3 \mu\text{m}^3$ (50^3 voxel^3) sub-volume sample that is a larger sub-volume of [Model 1] which has a sub-volume sample size of $23.4^3 \mu\text{m}^3$ (30^3 voxel^3). The location of the cropped regions for the subsample are shown in Table 4.7.

In Figures 4.11 to 4.16, the pore drag on the walls for fluid flow can be easily compared to zero drag on walls for the electrical current density diagrams. [Model 2] appears to be similar in the x and z directions only. The calculated permeability was 0.67 mD in the x and z directions. The permeability is 0.37 mD in the y direction. The lower permeability can be visually observed in the y direction for Figure 4.15 and Figure 4.16. For the x-direction and z-direction, the formation factor varied from 87.26 to 89.20 and the cementation exponent varied from 2.09 to 2.10. The y-direction formation factor is 135.06 and the cementation exponent is 2.29. The flow and electrical current density plots for the y-direction, as illustrated in Figures 4.15 and 4.16, are useful to visualize the difference observed in the calculated properties. In these figures, the fluid flow and electrical current density enter from the front xz face and exited in the y+ direction. There are a small number of very small pore constrictions that are limiting the flow in the y direction and so reducing the permeability and increasing the formation factor. The calculated transport properties are still of the same order of magnitude for all orthogonal directions; and the sample is close to isotropic. The velocity magnitude color scale was restricted from ~ 0 to 0.01 voxel/s and the electrical current density magnitude color scale was restricted from \sim to 0.01 A/vox^2 . Each simulation used roughly 18 GB of RAM plus 39 GB of virtual memory.

The RemeshSurface tool was only used on [Model 2]. It was used to remesh [Model 2] to 85% of the original mesh size. [Model 2] used automatic face partitioning for the STL file importation process and a segregated solver was used to solve the PDEs.

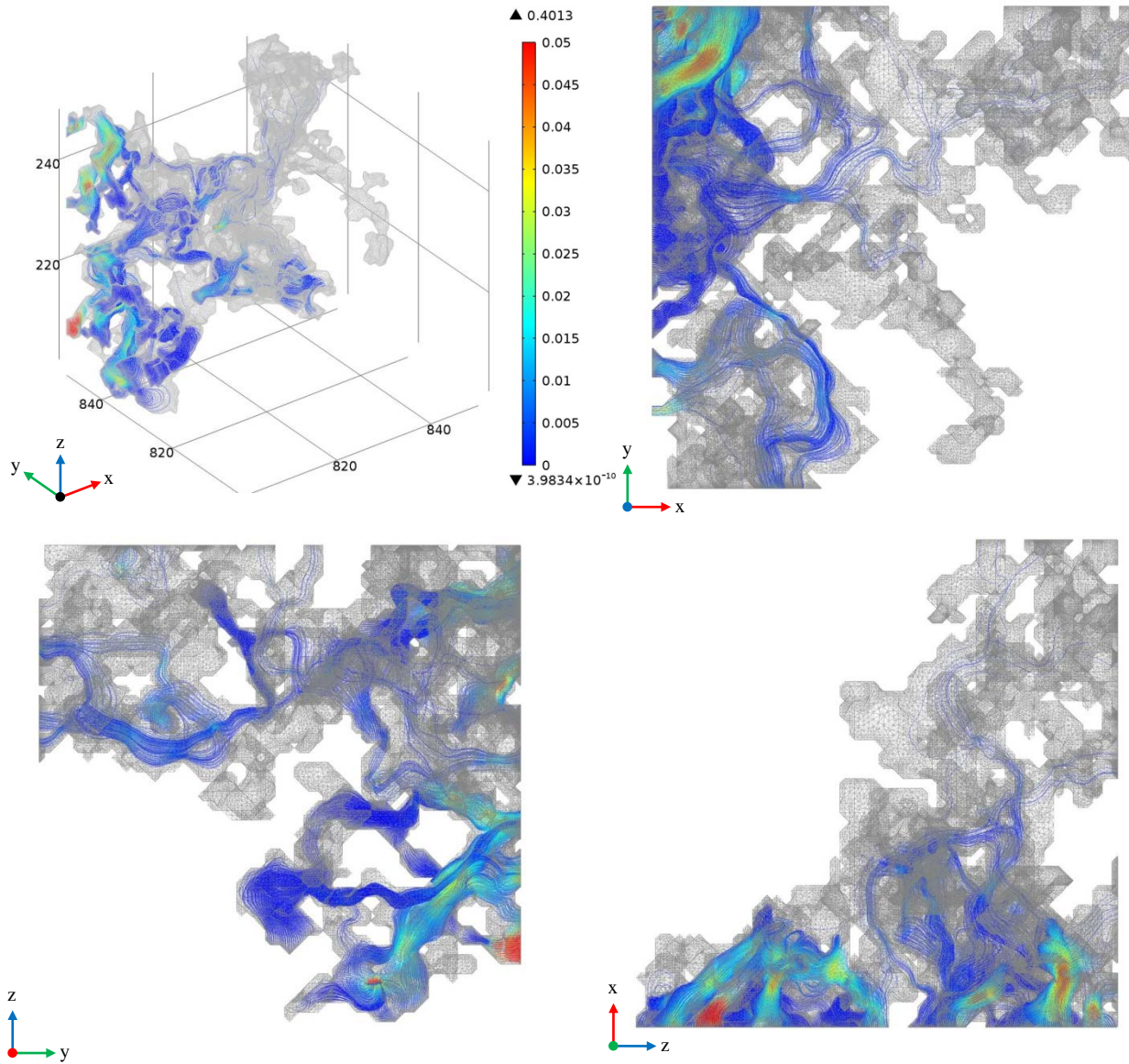


Figure 4.17 Flow diagrams from KD-18-03 subsample (Model 3-y1).

Image parameters for Model 3-y1 are as follows:

CMT Resolution: 0.78 μm

Subsample size: $(50 \text{ voxel})^3$, $(39.0 \mu\text{m})^3$ (x,y,z coordinates are: 800:850; 800:850; 200:250).

Streamline: Velocity field (used 5,000 points, inlet controlled).

Streamline color: Velocity Magnitude, normalized from blue (min. ~ 0) to red (0.01 voxel/s).

Mesh: Surface mesh displayed in grey.

Flow: Entering from the left yz face and exiting in the x+ direction.

Note: Mesh transparency was set to 50% in order to view the streamlines.

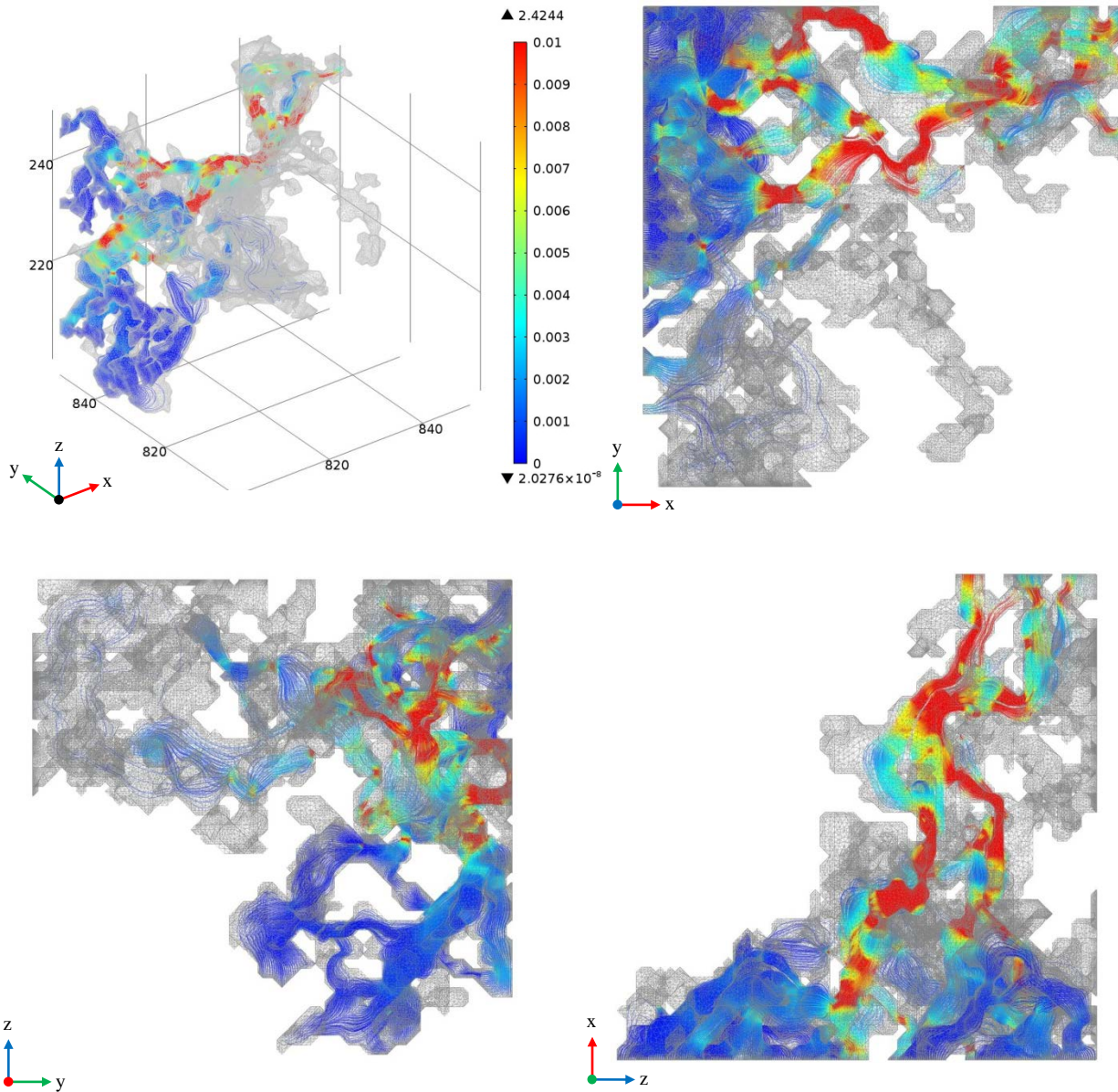


Figure 4.18 Electrical current density diagrams from KD-18-03 subsample (Model 3-y1).

Image parameters for Model 3-y1 are as follows:

CMT Resolution: 0.78 μm

Subsample size: $(50 \text{ voxel})^3$, $(39.0 \mu\text{m})^3$ (x,y,z coordinates are: 800:850; 800:850; 200:250).

Streamline: Current density (used 5,000 points, inlet controlled).

Streamline color: Current Density Magnitude, normalized from blue (min. ~ 0) to red (0.01 A/vox^2).

Mesh: Surface mesh displayed in grey.

Flow: Entering from the left yz face and exiting in the x+ direction.

Note: Mesh transparency was set to 50% in order to view the streamlines.

[Model 3] is a $39.0^3 \mu\text{m}^3$ (50^3 voxel^3) sub-volume sample. As listed in Table 4.1, the total porosity is 12.2% and the effective porosity is 5.8%. The subsample volume is roughly twice the size of the region with connected pore space as shown in Figures 4.17 and 4.18. The illustrated connected pore space is located near the edge of the positive y-axis and proceeds along the x-axis. Fluid flow and electrical current density enters from the left yz face and exits in the x+ direction. The calculated permeability is 0.10 mD with a formation factor of 309.43 and a cementation exponent of 2.02. The boundaries of the connected pore space only touch the zy plane, therefore, the transport properties in one of the orthogonal directions have been calculated. The velocity magnitude color scale was restricted from ~ 0 to 0.01 voxel/s and the electrical current density color scale was restricted from \sim to 0.01 A/vox².

[Model 3] STL file was imported using the composite object transformation in COMSOL 3.5a.

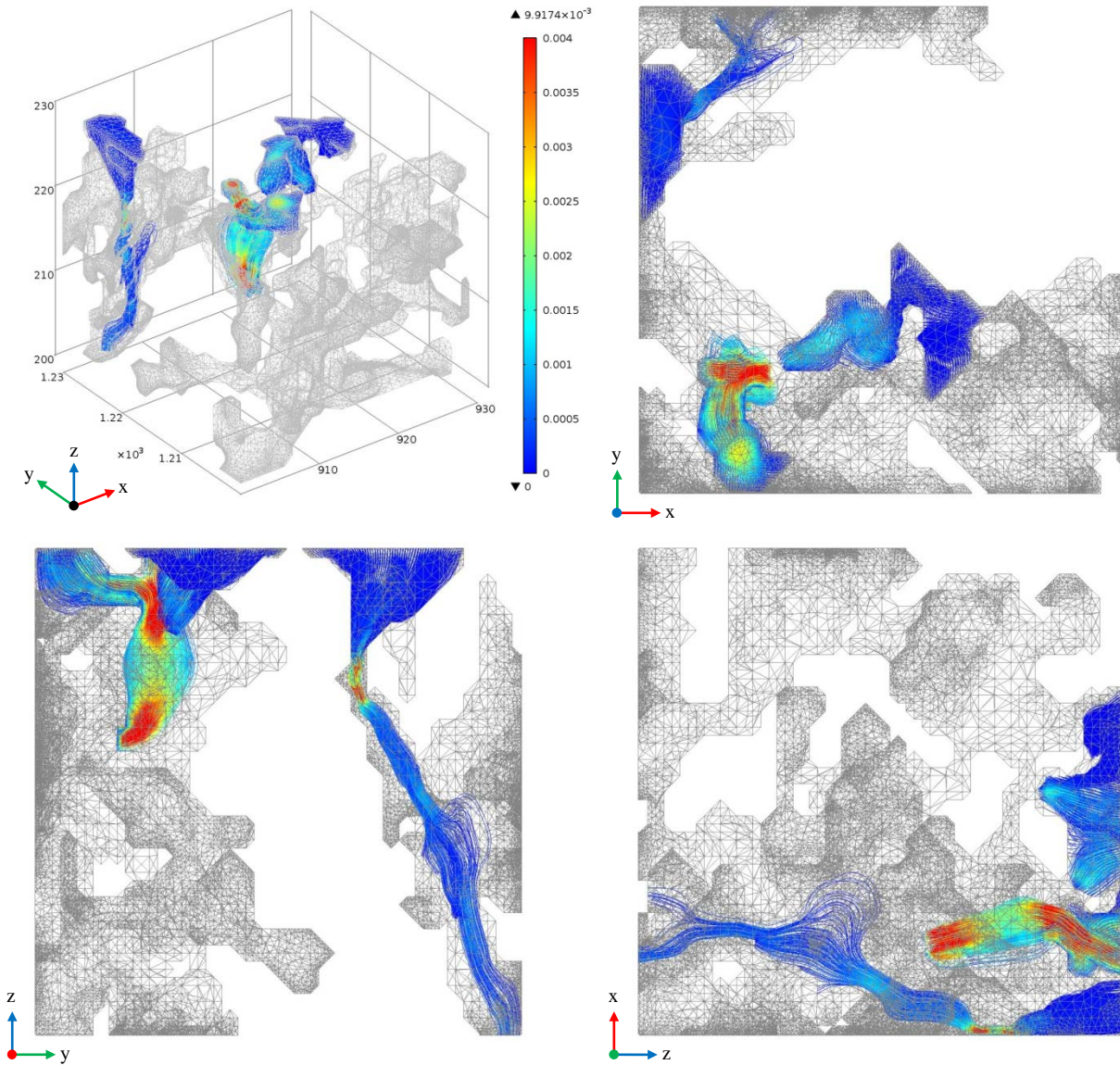


Figure 4.19 Flow diagrams from KD-18-03 subsample (Model 4-y1).

Image parameters for Model 4-y1 are as follows:

CMT Resolution: $0.78 \mu\text{m}$

Subsample size: $(30 \text{ voxel})^3, (23.4 \mu\text{m})^3$ (x,y,z coordinates are: 900:930; 1200:1230; 200:230).

Streamline: Velocity field (used 5,000 points, inlet controlled).

Streamline color: Velocity Magnitude, normalized from blue (min. ~ 0) to red (0.004 voxel/s).

Mesh: Surface mesh displayed in grey.

Flow: Entering from the top xy face and exiting in the z- direction.

Note: The flow is not connected in the y direction. Flow occupies two independent areas throughout the sample.

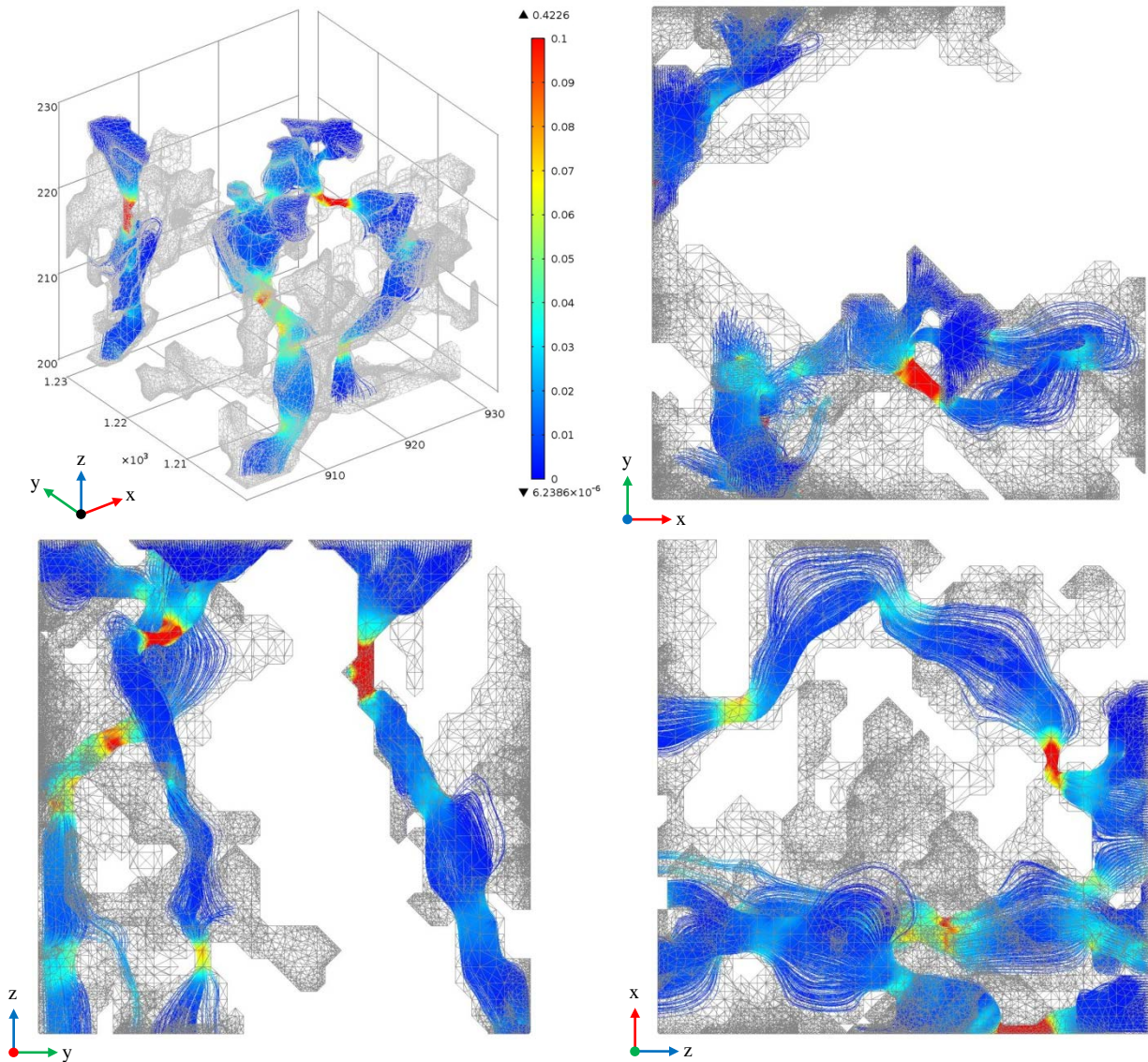


Figure 4.20 Electrical current density diagrams from KD-18-03 subsample (Model 4-y1).

Image parameters for Model 4-y1 are as follows:

CMT Resolution: $0.78 \mu\text{m}$

Subsample size: $(30 \text{ voxel})^3, (23.4 \mu\text{m})^3$ (x,y,z coordinates are: 900:930; 1200:1230; 200:230).

Streamline: Current density (used 3,000 points, inlet controlled).

Streamline color: Current Density Magnitude, normalized from blue (min. ~ 0) to red (0.1 A/vox²).

Mesh: Surface mesh displayed in grey.

Voltage: Entering from the top xy face and exiting in the z- direction.

Note: The flow is not connected in the y direction. Flow occupies two independent areas throughout the sample.

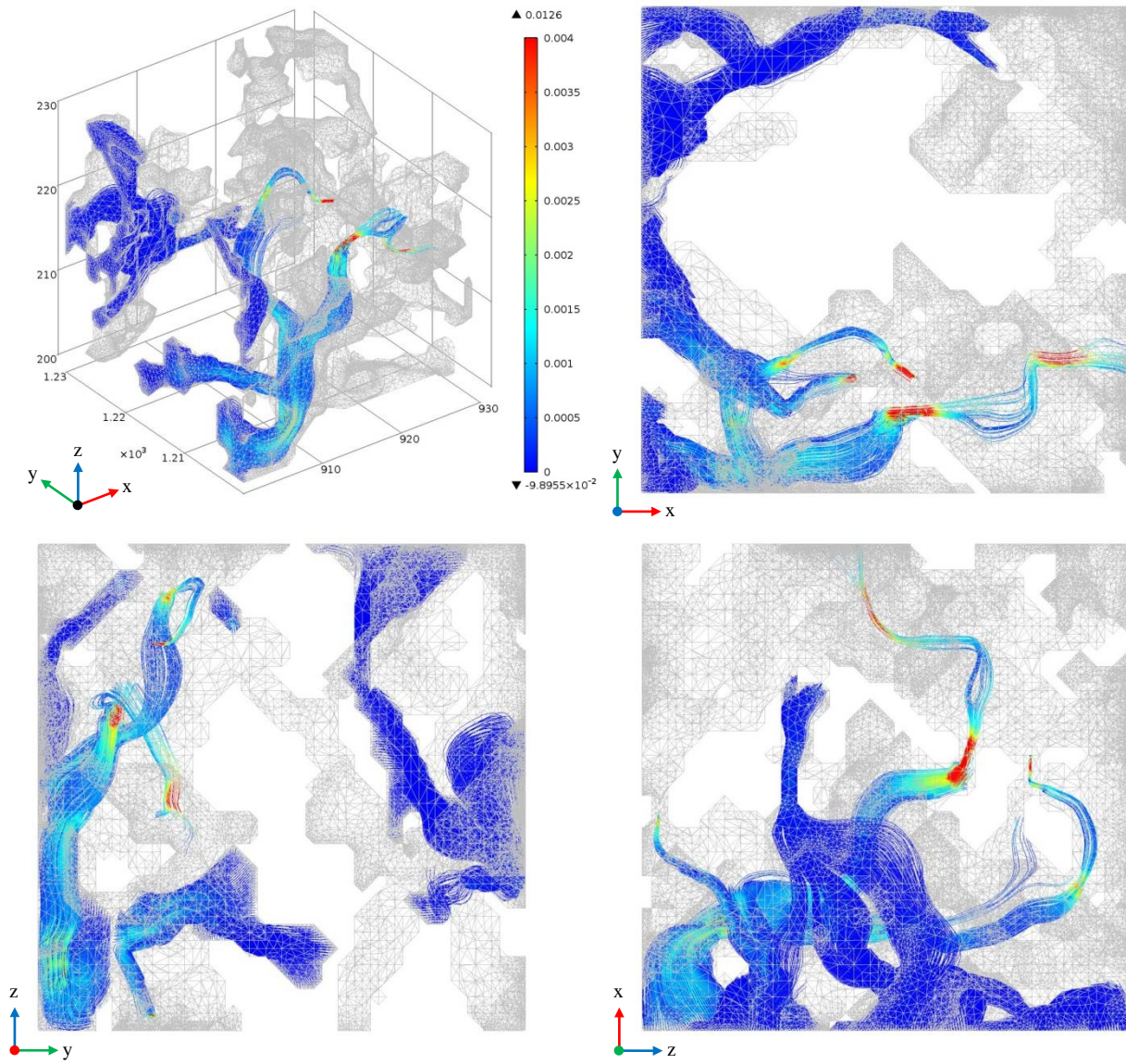


Figure 4.21 Flow diagrams from KD-18-03 subsample (Model 4-x1).

Image parameters for Model 4-x1 are as follows:

CMT Resolution: $0.78 \mu\text{m}$

Subsample size: $(30 \text{ voxel})^3, (23.4 \mu\text{m})^3$ (x,y,z coordinates are: 900:930; 1200:1230; 200:230).

Streamline: Velocity field (used 5,000 points, inlet controlled).

Streamline color: Velocity Magnitude, normalized from blue (min. ~ 0) to red (0.004 voxel/s).

Mesh: Surface mesh displayed in grey.

Flow: Entering from the left yz face and exiting in the x+ direction.

Note: The flow is not connected in the y direction. Flow occupies two independent areas throughout the sample.

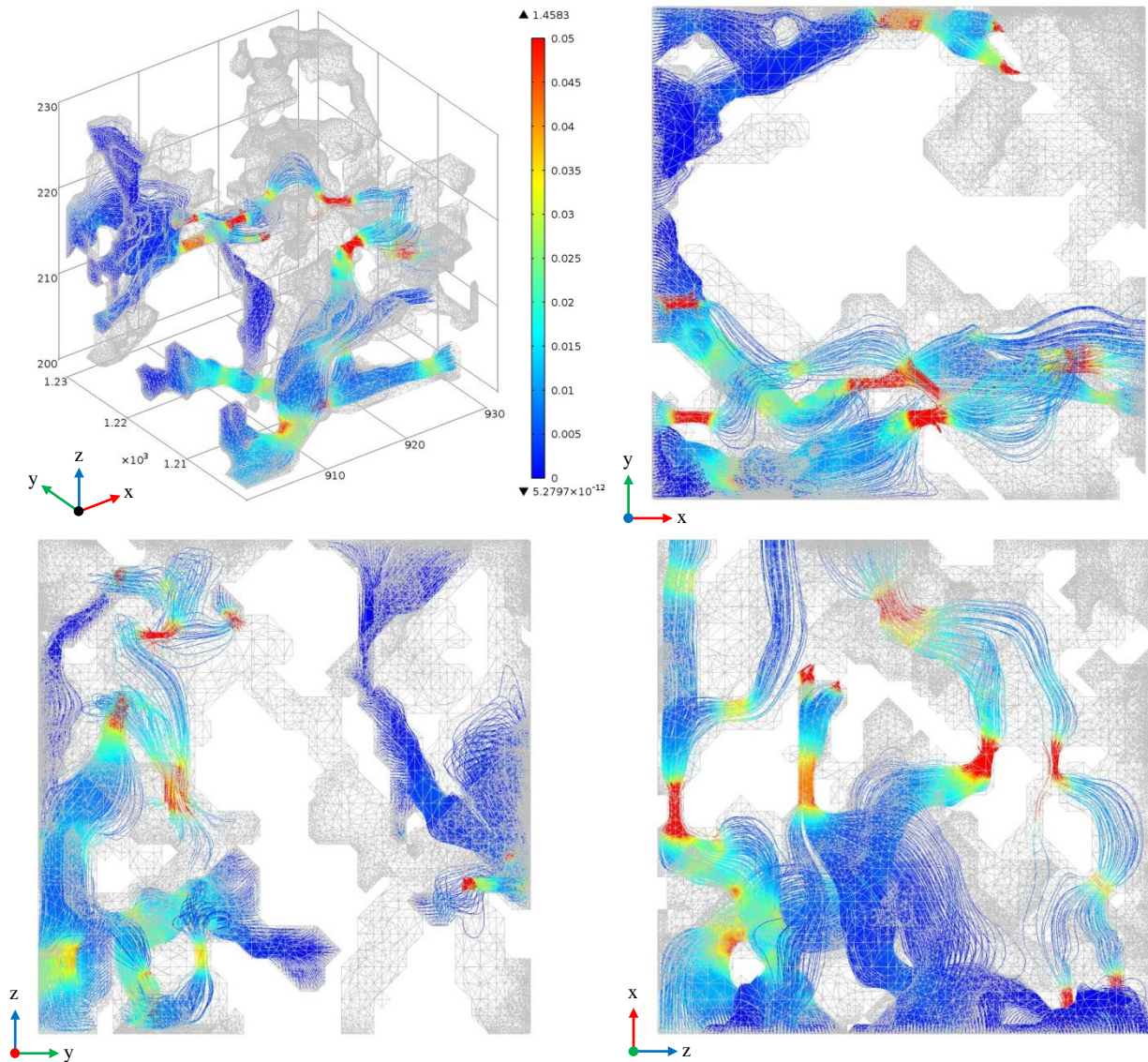


Figure 4.22 Electrical current density diagrams from KD-18-03 subsample (Model 4-x1).

Image parameters for Model 4-x1 are as follows:

CMT Resolution: $0.78 \mu\text{m}$

Subsample size: $(30 \text{ voxel})^3, (23.4 \mu\text{m})^3$ (x,y,z coordinates are: 900:930; 1200:1230; 200:230).

Streamline: Current density (used 3,000 points, inlet controlled).

Streamline color: Current Density Magnitude, normalized from blue (min. ~ 0) to red (0.05 A/vox^2).

Mesh: Surface mesh displayed in grey.

Flow: Entering from the left yz face and exiting in the x+ direction.

Note: The flow is not connected in the y direction. Flow occupies two independent areas throughout the sample.

[Model 4] is a $23.4^3 \mu\text{m}^3$ (30^3 voxel^3) sub-volume sample. This model is unique to the sub-samples observed since the connected pore space is split throughout the isolated sub-volume. The connected pore space is not joined in the y-direction with independent flow occurring in two separate regions. The connected pore space is evident only on the left side of the box. Figures 4.19 to 4.20 show flow and electrical current density flowing from the top xy face in the z- direction. The mass and current flows through the left regions are visually similar. Visualization of flow through the left xy face in the x+ direction is quite different. The fluid flow doesn't appear to flow through the entire volume, while the current density does. The velocity magnitude color scale was restricted from ~ 0 to 0.004 voxel/s and the electrical current density magnitude color scale was restricted from ~ 0 to 0.1 A/vox^2 .

[Model 4] STL file was imported using the composite object transformation in COMSOL 3.5a. The subsample regions where the pore space was extracted from the $0.78 \mu\text{m}$ CMT data from KD-18-03 Midale Marly, subsection 3 is shown in Table 4.7.

Table 4.7 Cropped Regions used inside KD-18-03, subsection 3

Model	Sample Volume (voxels ³)	x-direction region	y-direction region	z-direction region
1-y	30	500 to 530	500 to 530	0 to 30
1-z	30	500 to 530	500 to 530	0 to 30
1-x	30	500 to 530	500 to 530	0 to 30
2-z	50	480 to 530	480 to 530	0 to 50
2-x	50	480 to 530	480 to 530	0 to 50
2-y	50	480 to 530	480 to 530	0 to 50
3-y	50	800 to 850	800 to 850	200 to 250
4-y	30	900 to 930	1200 to 1230	200 to 230
4-x	30	900 to 930	1200 to 1230	200 to 230

4.3 Darcy Velocity Scaling to Reservoir Conditions

Previous work on a Marly (M3) core was completed at the Lawrence Livermore National Laboratory to quantify the relationship between fluid flow, heterogeneity, and chemical reaction rate specific to carbon storage at the Weyburn-Midale field (Carroll et al., 2011). The Marly (M3) core was obtained within the Weyburn reservoir and imaged at the ESRF on the same beamline used for the Marly (M0) CMT core. As listed in Table 1.2, the Marly (M0) core well sample depth was 1394 m obtained at well location 8-20-6-13W2. The Marly (M3) cores were obtained at well location 21/6-8-6-13W2 with sample depths of 1447, 1460 and 1446 m for samples 1 to 3 respectively (Carroll et al., 2011). The distance between the Marly (M0) and the Marly (M3) well locations is approximately 3.3 km.

A comparison of the calculated Darcy velocity between the Marly (M0) rock and the Marly (M3) rock was completed. The Marly (M3) Darcy velocity is representative of in-situ conditions at an injection well (Carroll et al., 2011). The cores for the Marly (M0) and Marly (M3) were taken at different locations, and the sample sizes vary.

Table 4.8 shows the Darcy velocity comparison so that the Darcy velocity of the Marly (M0) data can be scaled to represent reservoir conditions. The pressure gradient is the initial differential pressure across each Marly rock core. The Marly (M3) rock has a sample diameter of 15 mm, a sample length of 30 mm and a flow rate of 0.05 ml/min ($8.33 \times 10^{-10} \text{ m}^3/\text{s}$) (Carroll et al., 2011). The Darcy velocity was calculated as the volumetric fluid flow rate divided by the sample area. The Darcy velocity range for the Marly (M0) core was calculated using Equation 3.18 and the permeability range of 0.10 to 3.53 mD, as given in Table 4.2. To estimate representative in-situ conditions, the pressure gradient for the Marly (M3) samples was used with a viscosity of $9.00 \times 10^{-4} \text{ Pa}\cdot\text{s}$ (C. Glemser, 2007). The scale factor is the ratio of the Marly (M3) and Marly (M0) Darcy velocities.

Table 4.8 Darcy Velocity Comparison of Marly (M3) and Marly (M0) Core Samples

Marly (M3) (Sample #)	Pressure Gradient* (kPa/m)	Total Porosity* (%)	Darcy Velocity* (m/s)	Darcy Velocity Range Marly (M0) (m/s)	Scale Factor (Marly M3/M0)
1	2526.3	28.7%	4.72 e-6	2.81 e-7 to 9.91 e-6	0.06 to 2.10
2	1837.3	34.5	4.72 e-6	2.04 e-7 to 7.21 e-6	0.04 to 1.53
3	1607.7	35.4%	4.72 e-6	1.79 e-7 to 6.31 e-6	0.04 to 1.34

* Marly (M3) data (Carroll et al., 2011)

The permeability of the Marly (M0) ranges from 0.10 mD to 3.53 mD, as listed in Table 4.2. The laboratory measured permeability for the Marly (M3) samples are 0.9, 1.2 and 1.7 mD for samples 1 to 3 respectively. The permeability ranges are similar for both the Marly (M0) and the Marly (M3).

4.4 Summary for Results 1, High Resolution Marly Samples (0.78 μm)

A high resolution 0.78 μm CMT image of a Midale Marly (M0) rock was analyzed. Previous work, completed by Glemser (2007), analyzed the same Midale Marly KD-18-03 CMT rock core to calculate the porosity, permeability, formation resistivity factor and cementation exponent. A smaller subsection of the same sample as used by Glemser (2007) was used to allow the data to fit into the available computer memory.

Based on statistical analysis of the porosity, the side length for a cubic REV for porosity is estimated to be roughly between 78 and 156 μm (100 and 200 voxels). Due to computer memory constraints, we could only analyze a 24 μm (50 voxel) subsample. The 156 μm (200 voxel) region is estimated to generate over 100 million equations to solve.

The calculated porosity, permeability, formation resistivity factor and cementation exponent were compared to Glemser's (2007) results. As completed by Glemser (2007), the permeability for the KD-18-03 CMT rock core, using a Ruska Liquid Permeameter, was 7.7 mD. The simulated Katz-Thompson permeability was calculated to be 7.73 mD. The formation resistivity factor and cementation exponent were calculated to be 11.71 and 1.87 respectively (Glemser,

2007). Glemser's (2007) results were used to compare my calculated properties using the Navier-Stokes equations and Laplace's equation to determine if the workflow methodology was valid.

The calculated permeability ranged from 0.1 to 3.53 mD. The formation factor resistivity ranged from 29.3 to 309.4 and the cementation exponent ranged from 1.99 to 2.10. All calculated results are roughly within the same order of magnitude in comparison to the larger laboratory samples completed by Glemser (2007). The workflow methodology appears to be valid since the results are similar. All of the subsamples I used have porosity that is less than those of the whole sample. Using a subsample that has higher porosity may bring my permeabilities and formation factors closer to Glemser's (2007).

The value of 'a' was not assumed to be '1'. It was calculated using Archie's Law, as shown in Equation 1.7. If the total porosity is used, the values of 'a' range from 4.42 to 1.13. The calculated value of 'a' ranges from 1.01 to 0.98 using the effective porosity. Using the effective porosity gives a closer value to the '1' expected as the electrical flow is non-zero in this region only.

A comparison of the calculated Darcy velocity between the Marly (M0) rock and the Marly (M3) rock was completed so that the Darcy velocity of the Marly (M0) data can be scaled to represent reservoir conditions. Previous work on a Marly (M3) core was completed where the Darcy velocity is representative of in-situ conditions at an injection well as investigated at the Lawrence Livermore National Laboratory. (Carroll et al., 2011). The scale factor for Darcy velocity ranges from 0.04 to 2.10. These values can be used to multiply the Marly (M0) Darcy velocity and give a quasi-representative Darcy velocity of in-situ reservoir conditions at an injection well.

5 RESULTS 2, POST CO₂ FLOOD SAMPLE (7.45 μm RESOLUTION)

5.1 Core Sample Used in Results 2

A Vuggy (V6) core sample, called sample 1E, was investigated by (Kotzer et al., 2012). The remainder of section 5.1 is summarized their report.

The rock core is a vuggy limestone, with localized zones of crystalline dolomite growth which likely serve as the preferential locations of CO₂ dissolution. General fabric and composition suggests that these samples consist of limestone mudstone to wackestone. Effective porosity mainly consists of vuggy porosity. Small matrix intercrystalline porosity is also locally present in this sample. Moderately high to high volumes of non-effective microporosity may characterize these limestone mudstone to wackestone samples.

This core was taken from well 21/06-08-006-13W2, at a depth of 1462.65 m. This sampling point was selected because it is found within the V6 flow unit of the Midale Beds. The Vuggy (V6) unit is relevant to the study of CO₂ flooding in the Weyburn Field, as a significant fraction of the injected CO₂ is expected to flow through this unit. This particular sample was drilled prior to the commencement of CO₂ flooding for pre-CO₂ flooding CMT analysis. Sample 1E had then been exposed to CO₂ in a laboratory experiment that was designed to investigate the magnitude of permeability change (and to characterize the nature of mineral dissolution processes) upon exposure to CO₂-bearing brine at representative in-situ conditions (T = 60°C, pore pressure = 12.4 MPa, partial pressure of CO₂ = 0.5 MPa).

After the sample had been exposed to CO₂, and dissolution within the rock matrix occurred, CMT analysis was completed on a sub-volume of the original core. All work, including Post-CO₂ flooding from sample 1E was analyzed at the ESRF with a CMT resolution of 7.45 μm.

A similar workflow was used for pore extraction, as listed in section 2, and for calculating the physics solutions, as listed in section 3. Any modifications to the workflow is annotated in the following sections.

5.2 Smooth CMT data by resampling

In Sample 1E, CO₂ dissolution of the rock matrix resulted in large visible pore spaces. The largest dissolution region was isolated to calculate the maximum permeability. The permeability for the large region could not initially be calculated with full resolution due to computer memory limitations. Resampling the CMT data can be a way of smoothing the surface of the rock pore matrix to allow for a simplified mesh to fit into the available computer memory. Smoothing the surface is not anticipated to significantly change the permeability as laminar flows are weakly affected by surface roughness (Piller et al., 2009).

Various smoothing algorithms were investigated before the surface mesh was generated. In Results 1, the RemeshSurface module in Avizo Fire was successfully used to smooth the triangular surface and generate the desired result, however, this process was complicated to implement as the STL file format changes lead to topography errors. Considering the time involved for manual corrections, the RemeshSurface module was not used for the subsamples in Results 2, and a better method was investigated.

A downsampling filter was used to smooth the surface and generate a similar result as the RemeshSurface module without the requirement for manual mesh tweaking. Downsampling removed data points. Depending on the placement of the downsampling filter in the workflow, this resulted in varying amounts of smoothing.

During the downsampling investigation, a new computer with more memory became available. This computer had 131 GB of RAM, dual 8 core Zeon processors (32 cores hyper-threaded) and a NIVIDIA Quadro 6000 video card. This computer was used for all calculations in Results 2. A summary of the computer specifications are listed in Appendix C.

5.3 Import and Crop data

The objective was to capture an isolated section of CO₂ dissolution within the rock matrix and calculate the permeability. Whereas the subsample volumes used in Results 1 were randomly selected, in Results 2, the largest dissolution region with the smoothest wall surface was isolated so that the resulting surface mesh would have a less complex surface and the resultant 3D mesh

would be easier to solve numerically. The calculated permeabilities will not be representative of the sample as a whole and the permeability results will not be typical for this Vuggy rock. I expect the actual rock permeability will be substantially less than the permeability I calculate for this large pore.

The isolated 100 voxel region (1250:1350, 1450:1550, 0:100) is shown in Figure 5.1. As can be seen in Figure 5.1 B, the left edge of the pore space was made part of the model since it is a smooth surface and easier to calculate. The right edge of the pore space was 'clipped' so that the domain wall makes the side of the pore.

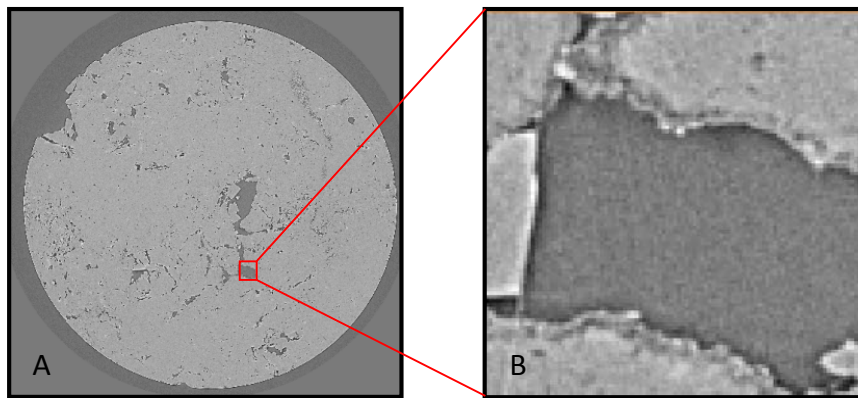


Figure 5.1 A large pore was selected that had observable CO₂ dissolution. (A) The orthoslice view displayed shows image 50 out of 100 images. (B) The region of dissolution was isolated to a 100 x 100 voxel region using the coordinates 1250:1350, 1450:1550, 0:100. The physical subsample size is 745 x 745 μm .

5.4 Threshold and binarize data

The porosity threshold was chosen by comparing CMT images of the observed pore space calculated with various thresholding values. The images shown in Figure 5.2 A-C result from using threshold values of 130, 160 and 143.

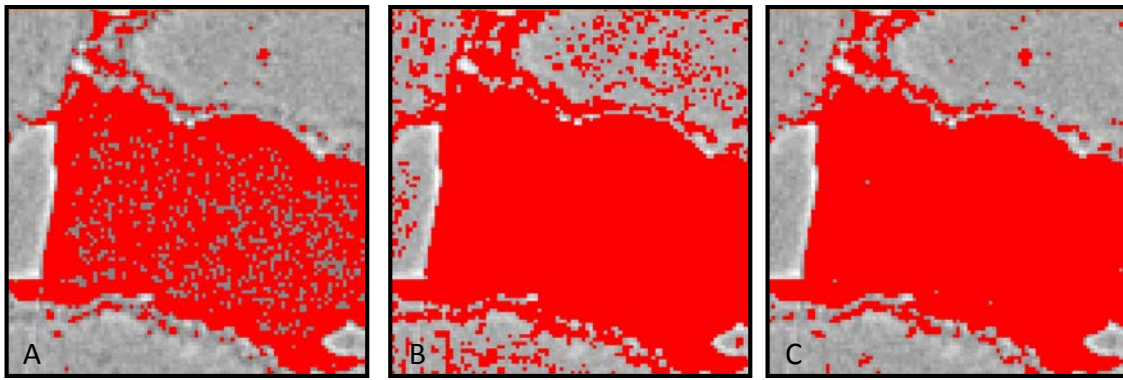


Figure 5.2 Thresholding the 100 voxel region of segment 2, slice 4. (A) Image thresholding value of 130. (B) Image thresholding value of 160. (C) Image thresholding value of 143. The thresholding region was isolated to a 100 x 100 voxel region. The physical subsample size is 745 x 745 μm .

Figure 5.2 A shows that thresholding the image at 130 doesn't appear to capture enough of the pore space while Figure 5.2 B shows that thresholding the image at 160 captures the pore space but also includes a significant amount of the rock. Figure 5.2 C shows a thresholded value of 143 which visually appears to be a good compromise between occupying the pore space and neglecting the rock.

The air gap located at the interface of the rock surface was investigated for thresholding the whole pore space. The thresholding values using the air gap ranged from roughly 80 to 120 which are smaller than the thresholded isolated Vuggy pore value of 143 shown in Figure 5.2 C. I have more confidence in the pore image-based threshold value, however, the air gap method is worth investigating in future studies. The thresholded value for this isolated pore was considered to be acceptable for permeability calculations on a single pore.

5.5 Resample test (0.78 μm CMT data)

The higher the resolution of the sample, the less physical size it can have and still be stored within the finite computer memory available. Resampling of the data was used to smooth the surface mesh, therefore making more simulation space available in the computer memory. With additional space, the permeability of larger volumes can be calculated.

Resampling refers to changing the spatial resolution of the data. Increasing or decreasing the spatial resolution is generally referred to as upsampling or downsampling respectively. If resampling of '1' was used in Avizo, the data remained exactly the same as before. If resampling was less than '1', the data was interpolated, or upsampled. If the resampling was greater than '1', the data was downsampled. Although downsampling resulted in a loss of image data, if the surface was sufficiently smooth, the resultant surface mesh should be adequately represented. The term, resampling, is used in the remaining discussion, but can be interchanged with downsampling.

With more complex geometry, it is anticipated that the pore throat volume would significantly change during the resampling process and therefore may significantly alter the calculated permeability depending on the type of rock being investigated. In order to test the permeability change with resampling, [Model 1], as used in Results 1, was considered.

The higher resolution 0.78 μm data of the Marly (MO) was resampled after filtering the data and before isolating the connected voxels. The modified Avizo workflow is shown below, with 'resample data' in bold to highlight the modified workflow:

- import data
- crop data
- threshold and binarize data
- filter data
- **resample data**
- voxel connections
- generate surface

The 0.78 μm resolution CMT data was resampled using the Lanczos filter in Avizo. The Lanczos filter is the product of two sinc functions.

$$L(x) = \begin{cases} \text{sinc}(x) \cdot \text{sinc}\left(\frac{x}{a}\right) & -a < x < a \\ 0 & \text{otherwise} \end{cases} \quad (6.1)$$

where x is the x-direction of Cartesian coordinate and a is the positive value of the kernel size.

The Lanczos filter was applied in three dimensions, so six sinc functions were required as shown in equation 6.2.

$$L(x, y, z) = L(x) \cdot L(y) \cdot L(z) \quad (6.2)$$

where $L(x)$, $L(y)$ and $L(z)$ are the respective sinc functions used in the x, y and z directions.

Permeability results for the non-resampled and resampled data are listed in Table 5.1 with the corresponding flow diagrams shown in Figure 5.3. The resampled data was calculated using the same subsection used for Model 1-y. To minimize potential confusion, the resampled data is referred to as Model 5.

Table 5.1 Calculated Permeability using Resampled Data on Model 5

Model	Resample (# times)	Permeability (mD)	Effective Porosity (%)	Equations (#)	Time (min)	RAM (GB)
5-y1	1.0	3.40	18.5	4,332,920	14.6	27.3
5-y2	1.5	2.96	18.5	505,412	1.27	4.1
5-y3	2.0	5.50	18.6	396,652	1.10	3.5
5-y4	3.0	2.30	8.00	23,532	0.08	1.0
5-y4	4.0	-	0.00	-	-	-

The porosity can increase or decrease as a function of resampling since the pore space, or pore wall, information is lost. Permeability can also increase or decrease since pore throats can either shrink or expand. Overall, the region of large pore throats became smoothly connected for resampling from 1.0x to 3.0x. Figure 5.3 A-C show the results of flow simulations with varying levels of resampling.

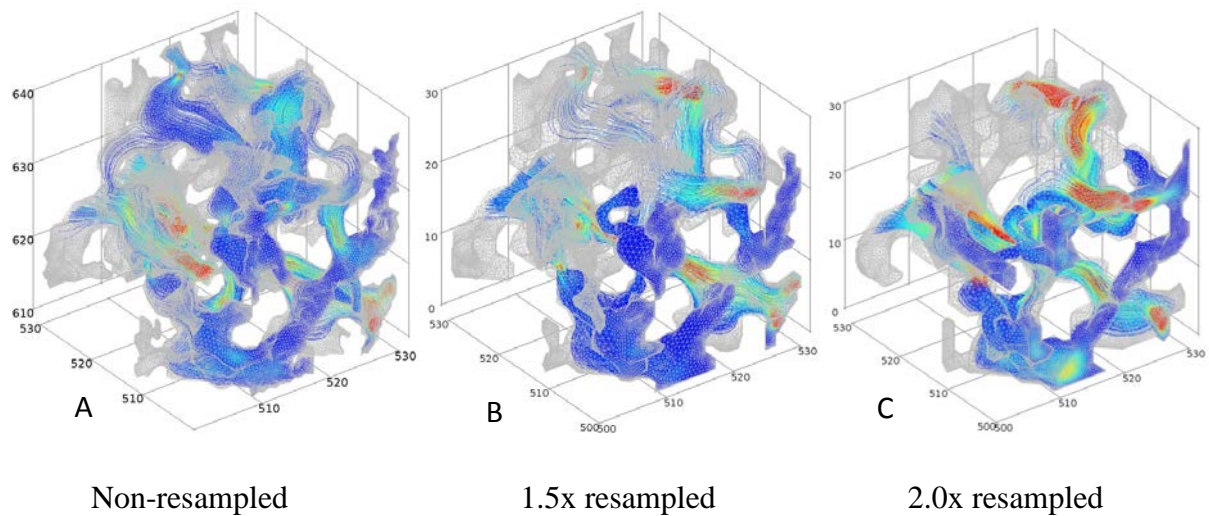
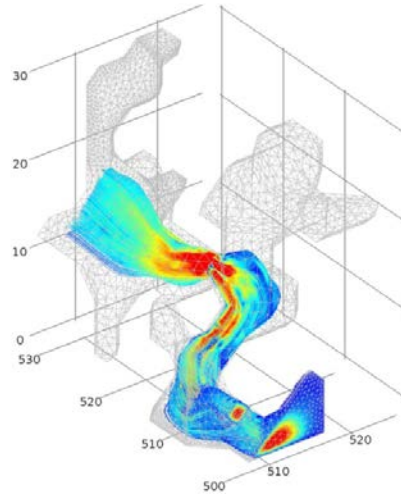


Figure 5.3 Flow diagrams to compare resampling on KD-18-01 subsample. (A) Image is the non-resampled image (1.0x resampled). (B) Image is 1.5x resampled. (C) Image is 2.0x resampled. (D) Image is 3.0x resampled. All image sizes are 30 x 30 x 30 voxels (23.4 x 23.4 x 23.4 μm).

The surface mesh was displayed in grey. The streamfunction represents the velocity magnitude normalized from ~ 0 to 0.01 (voxel/s) and is displayed with 5,000 streamlines. Fluid flow entered from the front xz face and exited the y+ direction.

The images for Figure 5.3 A-C are visually different as the surface became smoother. However, most of the geometry was preserved in the main fluid flow path. The permeability results are also similar for all three calculations.

A calculation performed after resampling the data 3.0x is shown in Figure 5.3.



3.0x resampled

Figure 5.4 Flow diagram with image 3.0x resampled. Image size is 30 x 30 x 30 voxels (23.4 x 23.4 x 23.4 μm).

Resampling the data 3.0x resulted in significant loss of pore space with a lower permeability of 2.30 mD and a lower porosity of 8%.

All permeabilities are within an order of magnitude indicating that most of the fluid flow is carried by the largest pore. For 4.0x resampling, the pore space was not connected so the permeability and effective porosity were both zero.

Care should be taken as the dominant flow will change based on resampling the surface. The amount of resampling should be chosen to preserve the rock matrix geometry and the fluid flow space. My results suggest that permeabilities calculated for downsampled volumes are similar to those calculated without resampling provided that the porosity does not change significantly.

5.6 Darcy's Flow Regime Verification

All models, using Sample 1E, have been verified for flow in the Darcy flow regime as shown in Table 5.2. [Model 6] is a cherry picked, resampled 100 voxel region of CO_2 dissolution. [Model 7] is [Model 6] expanded by 50 voxels from each face (200 voxel region). [Model 8] is a 200 voxel region of randomly isolated CO_2 dissolution. The Darcy velocity can be easily scaled if a different pressure gradient is used. The Darcy velocity can be calculated for any

pressure gradient by multiplying the calculated permeability by the desired pressure gradient and dividing by the fluid viscosity.

Table 5.2 Darcy's Flow Regime Verification

Model	Inlet Pressure (N/voxel ²)	Inlet Pressure (Pa)	Outlet Pressure (N/voxel ²)	Outlet Pressure (Pa)	Darcy Velocity (m/s)	Permeability (mD)
6-z1	1.00 e-3	5.57 e-14	0	0	3.00 e-9	2.24 e6
6-z2	5.00 e-4	2.78 e-14	0	0	1.50 e-9	2.24 e6
6-z3	2.00 e-4	1.11 e-14	0	0	6.01 e-10	2.24 e6
7-z6	1.00 e-3	5.57 e-14	0	0	1.78 e-11	2.66 e5
7-z7	5.00 e-4	2.78 e-14	0	0	8.91 e-12	2.66 e5
7-z8	2.00 e-4	1.11 e-14	0	0	3.57 e-12	2.66 e5
8-x1	1.00 e-3	5.57 e-14	0	0	4.60 e-13	343.26
8-x2	5.00 e-4	2.78 e-14	0	0	2.30 e-13	343.26
8-x3	2.00 e-4	1.11 e-14	0	0	9.20 e-14	343.26

The permeability remains constant with varying pressure gradient, therefore, we are in the Darcy flow regime and Darcy's equation was used to calculate the permeability. We used an inlet pressure of 10^{-3} [N/voxel²] for these calculations because the flow was not in the Darcy flow regime for an inlet pressure of 1 [N/voxel²].

5.7 Resample data (7.45 μm CMT data)

In order to provide a comparison, a cylinder was used to estimate the permeability for [Model 6]. The diameter of the cylinder was estimated to be the same as the dimension of the box at 745 μm.

For a cylinder, the permeability can be calculated using equation 6.3 (Turcotte et al., 2001):

$$Q = \frac{\pi R^4 dp}{8\mu dx} \quad (6.3)$$

Where R is the radius of the cylinder and Q is the total volume of the fluid.

The Darcy velocity is calculated using:

$$u = \frac{Q}{A} = \frac{\frac{\pi R^4 dp}{8\mu dx}}{\frac{\pi \cdot R^2}{\phi}} = \frac{\phi R^2 dp}{8\mu dx} \quad (6.4)$$

Where A is the area of the cylinder enclosing the cube and ϕ is the porosity.

We can solve for the permeability using Equation 1.2:

$$k = \frac{\phi R^2}{8} = \frac{0.588 \cdot \left(\frac{745 \times 10^{-6}}{2}\right)^2}{8} = 1.02 \times 10^{-7} mD \quad (6.5)$$

The simple permeability calculation is approximately one order of magnitude higher than the calculated permeability using CMT data. This simplified permeability calculation was based on smooth cylinder tube walls while the calculated permeability is based on real data with rougher pore walls which are likely to decrease the permeability.

The workflow, as used in Results 1, was modified to include resampling after importing the data in [Model 6]. Thresholding a 100 voxel (745 μ m) subsection of a Vuggy (V6) core sample was completed using a visible connected pore region on the resampled CMT data.

Table 5.3 lists the calculated permeability results. The data was resampled from 1.0x (non-resampled) to 8.0x to determine the permeability change associated with resampling. All permeability results are within the same order of magnitude, with a total permeability change of 29%. The number of equations, time and RAM usage drops rapidly for increasing resampling.

Table 5.3 Calculated Properties for [Model 6] with Resampling

Model	Resample (#)	Permeability (mD)	Effective Porosity (%)	Equations (#)	Time (min)	RAM (GB)	Error (%)	Figure
6-z4	1.0x	2.27 e6	58.8	4,598,992	27.7	60.0	0.3	5.4 A
6-z5	2.0x	2.23 e6	58.6	416,672	1.10	2.3	0.5	5.4 B
6-z6	3.0x	2.22 e6	57.9	153,448	0.40	2.1	0.5	5.4 C
6-z7	4.0x	2.64 e6	59.3	133,204	0.35	1.6	0.3	5.4 D
6-z8	6.0x	3.11 e6	55.4	33,628	0.10	0.9	1.5	5.4 E
6-z9	8.0x	3.20 e6	56.1	23,688	0.10	0.7	1.6	5.4 F

The simulation time used to compute the permeability for the 8.0x resampled data was approximately 277 times shorter than the simulation time used to compute the permeability for the 1.0x resampled data. The 1.0 x resampled and 2.0x resampled model took a long time to create the mesh and effectively run the permeability simulation. The COMSOL solver first uses virtual memory, or hard drive space, to create the mesh before running the simulation. For the non-resampled simulation, the total amount of memory used is 60 GB of RAM compared to 2.3 GB of RAM for the 2.0x resampled simulation.

Figure 5.5 gives the fluid flow images for simulations of [Model 6]. The flow images A through F are resampled 1x, 2x, 3x, 4x, 6x and 8x respectively. Flow entered from the top xy face and flowed in the z- direction. The images show streamlines of the velocity field originating from the inlet. The streamline color is the velocity magnitude. The mesh, representing the connected pore space within the subsample, is shown in black to highlight the decreasing pore complexity. The subsample size is 10^6 voxels³ with a CMT resolution of 7.45 μm .

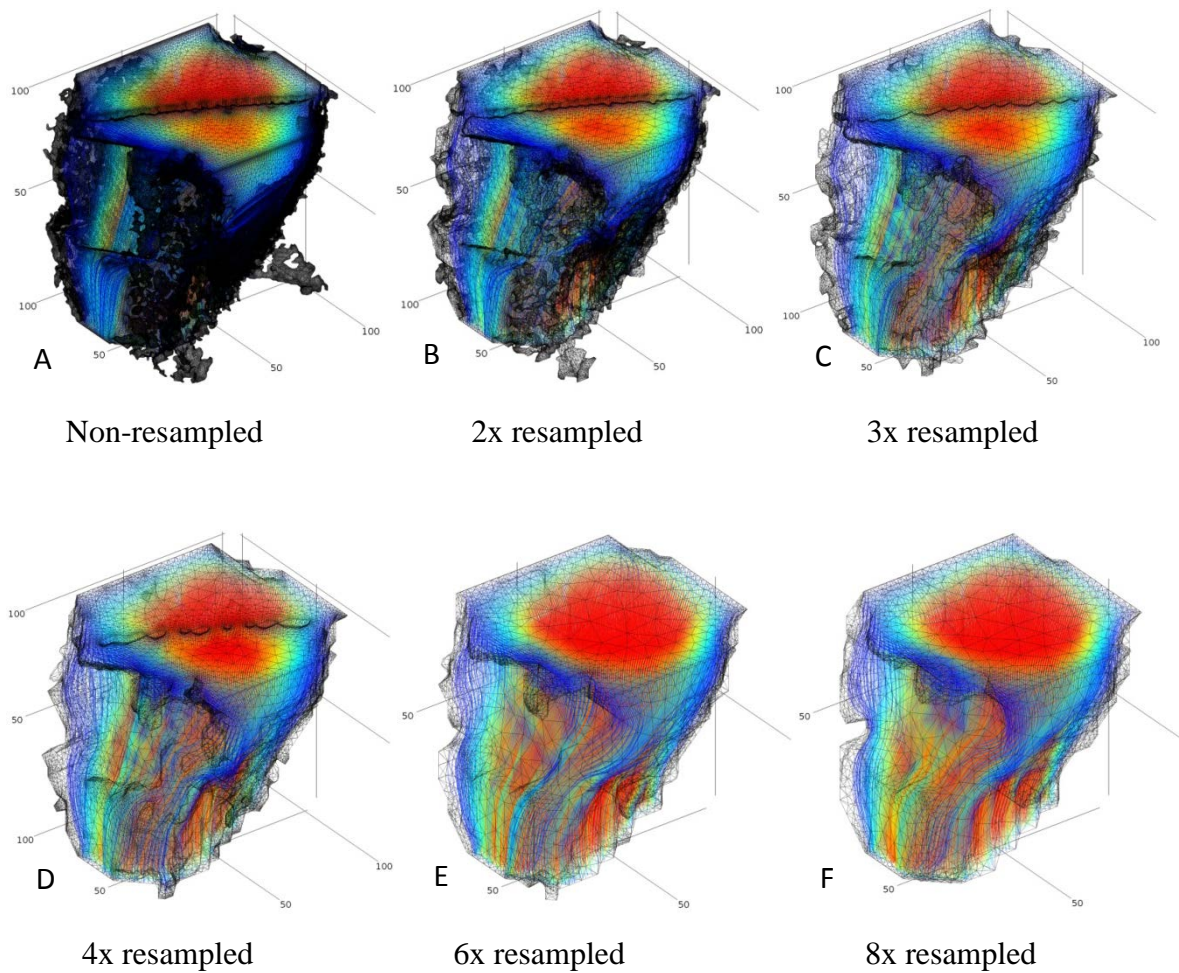


Figure 5.5 Connected pore space of resampled images A through F. The images were resampled 1x (non resampled), 2x, 3x, 4x, 6x and 8x resampled respectively. The figure displays 5,000 streamlines of the velocity field originating from the inlet at the top surface. The streamline color is the pressure (red = high; blue = low). The inlet boundary condition is a pressure of '1' [N/voxel²] and the bottom outlet boundary condition is a pressure of '0' [N/voxel²]. The surface mesh is shown in black to indicate how the mesh complexity is reduced with increased resampling. The subsample size is 100^3 voxels³ (745^3 μm^3) with a CMT resolution of 7.45 μm .

Visual comparison between the images shows that the resampling smooths the surface data without significantly changing the overall geometry. The streamfunction of the velocity magnitude is shown with 5,000 streamlines with the velocity magnitude normalized from ~ 0 to 0.002 (voxel/s). A transparency of 50% was used.

In Figure 5.6 I display the results of simulation [Model 6-z4] plotted in the same manner as those in Results 1. The surface mesh is displayed in grey. The velocity field is shown with 5,000 streamlines with the velocity magnitude normalized from ~0 to 0.001 (voxel/s).

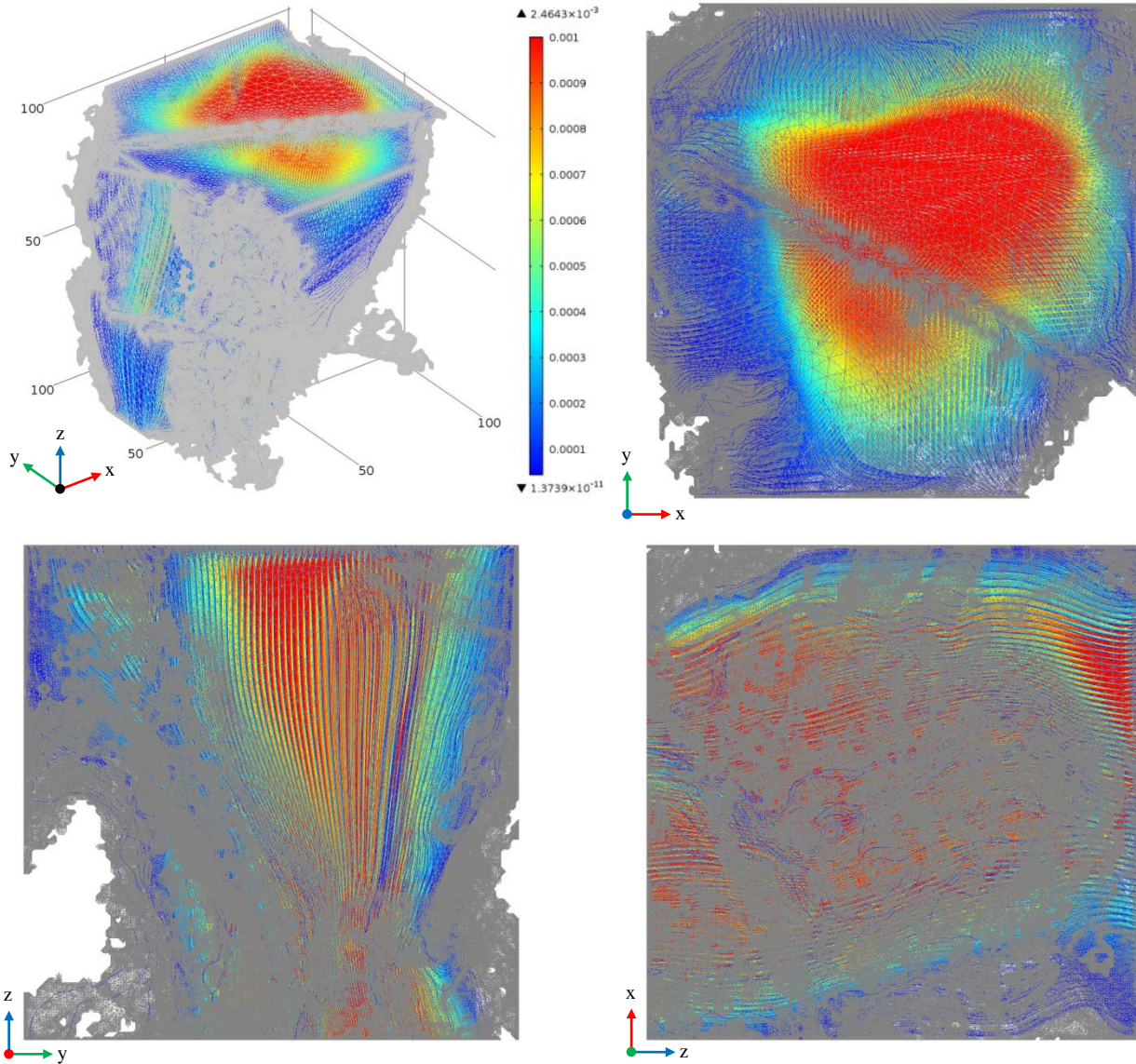


Figure 5.6 Flow diagrams from Model 6-z4 (non resampled). The subsample size is 100^3 voxels³ ($745^3 \mu\text{m}^3$) with a CMT resolution of $7.45 \mu\text{m}$.

All of the simulations used in [Model 6], used Sample 1E, section 4, with the default STL relative tolerance of 10^{-6} . Manual face partitioning was used for images resampled 1.0x and 2.0x. Automatic face partitioning was used for images resampled 3.0x, 4.0x, 6.0x and 8.0x. A

free tetrahedral mesh was used for the 1.0x resampled image. All other resampled images used boundary layer meshing. A direct solver was used for all simulations.

In order to determine the change associated with resampling the data before the image is cropped, the workflow was revised again for a 200 x 200 x 200 voxel (1490 x 1490 x 1490 μm) subsample. In this case, the right edge of the pore space was not 'clipped'. The 200 voxel region is a larger version of the 100 voxel subsection used in [Model 6]. The side lengths in [Model 6] were increased by 50 voxels from each surface to obtain the 200 voxel region in [Model 7]. The resampling was completed after importing the data and before cropping the data. The modified workflow for the 7.45 μm CMT data is:

- import data
- **resample data**
- crop data
- threshold and binarize data
- filter data
- voxel connections
- generate surface

A table of calculated permeability results for [Model 7] are listed in Table 5.4. The resampling was completed from 2.0x to 10.0x. Similar to the results in [Model 6], the permeability results for [Model 7] are within an order of magnitude for all degrees of resampling with a total permeability change of 69% and the porosity barely changes. The number of equations, time and RAM usage drops rapidly for increasing resampling. The time listed in Table 5.4 is the calculation time for obtaining the permeability and does not include time to complete the 3D meshing.

Table 5.4 Calculated Permeability with Resampling for [Model 7]

Model	Resample (#)	Permeability (mD)	Effective Porosity (%)	Equations (#)	Time (min)	RAM (GB)	Error (%)	Figure
7-z1	2.0x	8.57 e5	34.8	7,714,420	68.2	131	0.1	5.6 A
7-z2	3.0x	4.58 e5	32.6	1,622,648	7.80	21.3	0.2	5.6 B
7-z3	4.0x	5.42 e5	36.3	2,133,584	11.1	30.5	0.2	5.6 C
7-z4	6.0x	3.94 e5	35.7	900,744	5.95	9.10	0.03	5.6 D
7-z5	8.0x	2.99 e5	36.7	522,888	2.03	4.80	0.2	5.6 E
7-z6	10.0x	2.65 e5	37.9	362,808	1.40	4.80	0.2	5.6 F

Comparison of the simulated flow is shown in Figure 5.7. The flow images A through F are resampled 2x, 3x, 4x, 6x, 8x and 10x respectively. Flow entered from the top xy face and flowed in the z- direction. The mesh is shown in black to highlight the decreasing pore complexity. The subsample size is 200^3 voxels³ (1490^3 μm^3) with a CMT resolution of 7.45 μm .

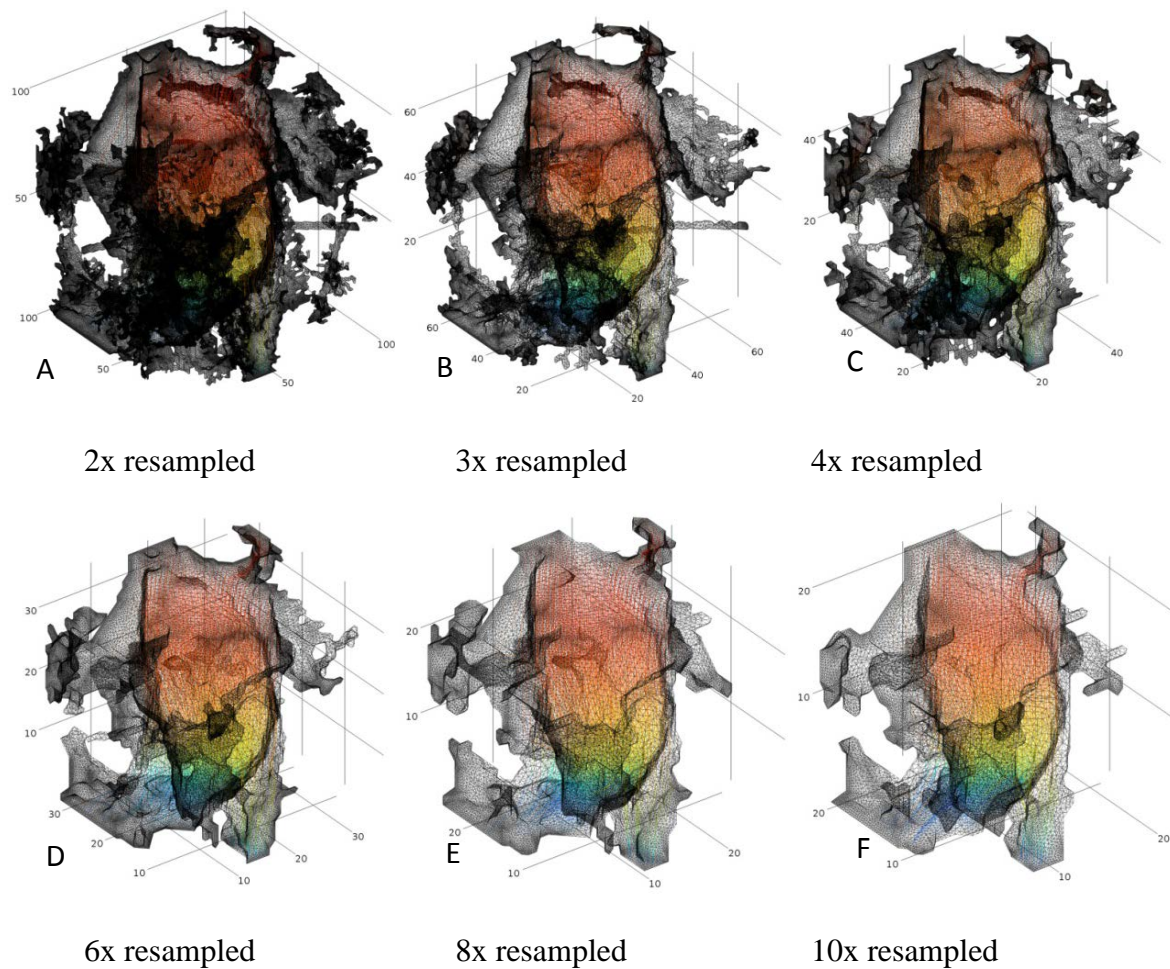


Figure 5.7 Connected pore space of resampled images A through F. The images were resampled 2x, 3x, 4x, 6x, 8x and 10x respectively. The figure displays 1,000 streamlines of the velocity field originating from the inlet at the top surface. The streamline color is the velocity magnitude. The inlet boundary condition is a pressure of '1' [N/voxel²] and the bottom outlet boundary condition is a pressure of '0' [N/voxel²]. The surface mesh is shown in black to indicate how the mesh complexity is reduced with increased resampling. The subsample size is 200³ voxels³ (1490³ μm³) with a CMT resolution of 7.45 μm.

There are thresholding variations associated with resampling the data before thresholding it. When the data was resampled immediately after cropping the data, the porosity is no longer isolated with a thresholding value of 143. The threshold value for each of the resampled images had to be visually compared to the previous images and a threshold was chosen so that the geometry was as similar as possible to the non-resampled case. We would expect to lose small

pores as we resample even without changing the threshold level. There is a circular region of connected pore space protruding from the right side of Figure 5.7 B. Figure 5.7 A also shows this connected pore space along with additional connections while Figure 5.7 C doesn't show the circular pore space connection. The fluctuation between the connected pore space, and the resultant permeability is also observed in Table 5.4. This fluctuation could be due to losing small pores from resampling, or due to variation in thresholding level.

In Figure 5.8, the surface mesh is displayed in grey to highlight the flow area. The velocity field is shown with 5,000 streamlines with the velocity magnitude normalized from ~ 0 to 0.001 (voxel/s). Flow entered from the top xy face and exited the z-direction. The 100 voxel (745 μm) region, as used in [Model 6] and Figure 5.6, is shown with a broken black outline in the xy coordinate plot for visual comparison. Dead-end pore space can be observed at the top of the xy face in the 3D orthographic view.

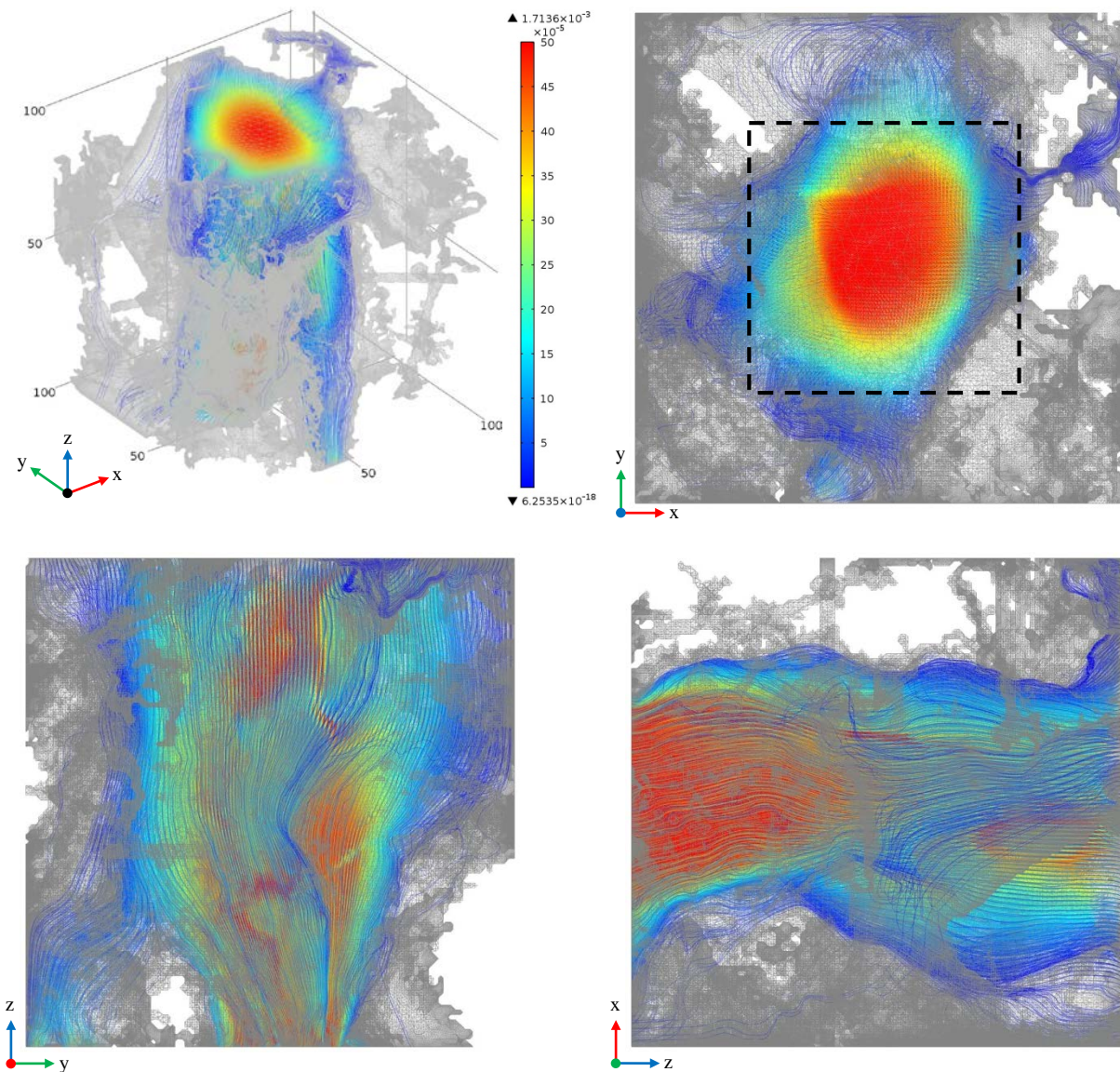


Figure 5.8 Flow diagrams from Model 7-x1 (2.0 x resampled). The subsample size is 200^3 voxels³ (1490^3 μm^3) with a CMT resolution of 7.45 μm .

Using the 200^3 voxel volume, the Darcy velocity is anticipated to decrease as most of the flow is located in the 100 voxel subsample. The 100 voxel subsample area, displayed in Figure 5.6, is shown with a black outline in the xy direction of Figure 5.8. The main fluid flow travels through the 100 voxel section. Since both [Model 6-z5] and [Model 7z-1] used 2.0x resampled data, they were used to compare the permeability. The permeabilities are $2.23 \cdot 10^6$ mD and $8.57 \cdot 10^5$ mD respectively. If the permeability for [Model 7z-1] was calculated by integrating

the mass flux over the 200 voxel region, but then dividing by the area of a 100 voxel region, the permeability would be $1.72 \cdot 10^6$ mD. This permeability result is close to the $2.23 \cdot 10^6$ mD permeability calculated for [Model 6-z5]. The permeability result was anticipated to be higher since a small portion of fluid flow occurs outside the 100 voxel region. This permeability difference is likely due to the thresholding values estimated as the data was resampled before the thresholding was used. In short, the thresholding values for [Model 6] and [Model 7] are different. Future thresholding should be completed with an Avizo workflow where resampling is completed after thresholding, as in the workflow used for Results 1, [Model 5], and [Model 6].

The 2.0x resampled model took a long time to create the mesh and effectively run the permeability simulation. This was partially due to the fact that the computer used in Results 1 was initially used. Virtual memory, or hard drive swap space, was being used to start the 3D mesh generation. The total time required to export the mesh correctly and successfully start the permeability calculation was roughly one week. The simulation was terminated after roughly 4 days. When the new computer was available, the simulation was successfully completed. For the 2.0x resampled simulation, the total amount of memory used was 128 GB of RAM, plus 139.3 GB of virtual memory, compared to 4.80 GB of RAM for the 10.0x resampled simulation.

The 3.0x resampled model took roughly one day to complete the simulation starting with the pore extraction using Avizo and ending with the analysis completed using COMSOL. The 4.0x resampled model took about 30 minutes to complete since automatic face partitioning, a direct solver, and a boundary layer mesh could be used in COMSOL.

All of the simulations used the default STL relative tolerance of 10^6 with automatic face partitioning. A direct solver with a free tetrahedral mesh was used for all simulations except that [Model 7-z3] (resampled 4.0x) used a boundary layer mesh and [Model 7-z4] (resampled 6.0x) used an iterative multigrid solver.

A randomly isolated subsection, called [Model 8], was used to calculate the permeability, porosity, formation resistivity factor and cementation exponent. The data was not resampled. This is the same workflow as used for Results 1.

- import data
- crop data
- threshold and binarize data
- filter data
- voxel connections
- generate surface

Table 5.5 displays the calculated transport properties for [Model 8]. The pore space is only connected in the x-direction for [Model 8]. The isolated sub-volume, located in Sample 1E, section 3, has a single connected component located near the bottom of the 3D sub-sample. Calculation of the transport properties were completed for both the 100 x 100 x 100 voxel (745 x 745 x 745 μm) region, [Model 8-x1] and the region of connected pore space that was isolated to a 100 x 60 x 60 voxel (745 x 447 x 447 μm) region, [Model 8-x2].

Table 5.5 Calculated Properties for [Model 8]

Model	Permeability (mD)	Total Porosity (%)	Effective Porosity (%)	Resistance $(\frac{\Omega \cdot m}{\text{voxel}})$	Resistivity ($\Omega \cdot m$)	Formation Factor (F)	Cementation Exponent (m)	Figures
8-x1	343.26	13.1	2.6	1.17	116.51	116.51	1.30	5.9
8-x2*	953.49	36.4**	7.2	1.17	41.94	41.94	1.42	5.10

Formation Resistivity Factor, F; Cementation Exponent, m;

*Model 8-x2 used Model 8-x1 data that was re-calculated using a 60 x 60 x 100 voxel (447 x 447 x 745 μm) box

**Total porosity for Model 8-x2 was not recorded. It was estimated by scaling the total porosity from Model 8-x1.

The calculated permeability of [Model 8-x1] is 342.34 mD. The formation factor is 116.51 and the cementation exponent is 1.30. As most of the connected pore space exists in only one side of the cube volume, the properties were calculated using the smaller rectangular region in [Model 8-x2]. The calculated permeability is 950.93 mD with a formation resistivity factor and cementation exponent of 41.09 and 1.42 respectively.

The calculated permeability range for [Model 8], is smaller than the previously calculated permeabilities in [Model 6] and [Model 7]. [Model 6] and [Model 7] used visually selected subsections to estimate the maximum permeability of the pore space after CO₂ dissolution. [Model 8] was randomly selected to provide a permeability estimate that is more representative of the rock matrix. This permeability for [Model 8] was also completed using non-resampled CMT data. This permeability could be used as an initial approximation of the actual reservoir permeability after CO₂ dissolution. This permeability might be expected to be less than the permeability of the whole rock since the majority of fluid flow is anticipated to flow through the largest pores isolated in [Model 6] and [Model 7], however, it may still be greater than the permeability for the total rock if this randomly chosen sample had an unusually large pore. An estimate of the permeability range could be further refined by investigating additional randomly isolated subsamples and obtaining a larger sub-volume for the permeability of visually isolated pores. In order to accelerate this process, resampling could be used to generate the larger subsamples with minimized computer resources.

In Figure 5.9, the surface mesh is displayed in grey. The velocity field is shown with 5,000 streamlines with the velocity magnitude normalized from ~ 0 to 10^{-5} (voxel/s). Flow entered from the left yz face and exited the x+ direction.

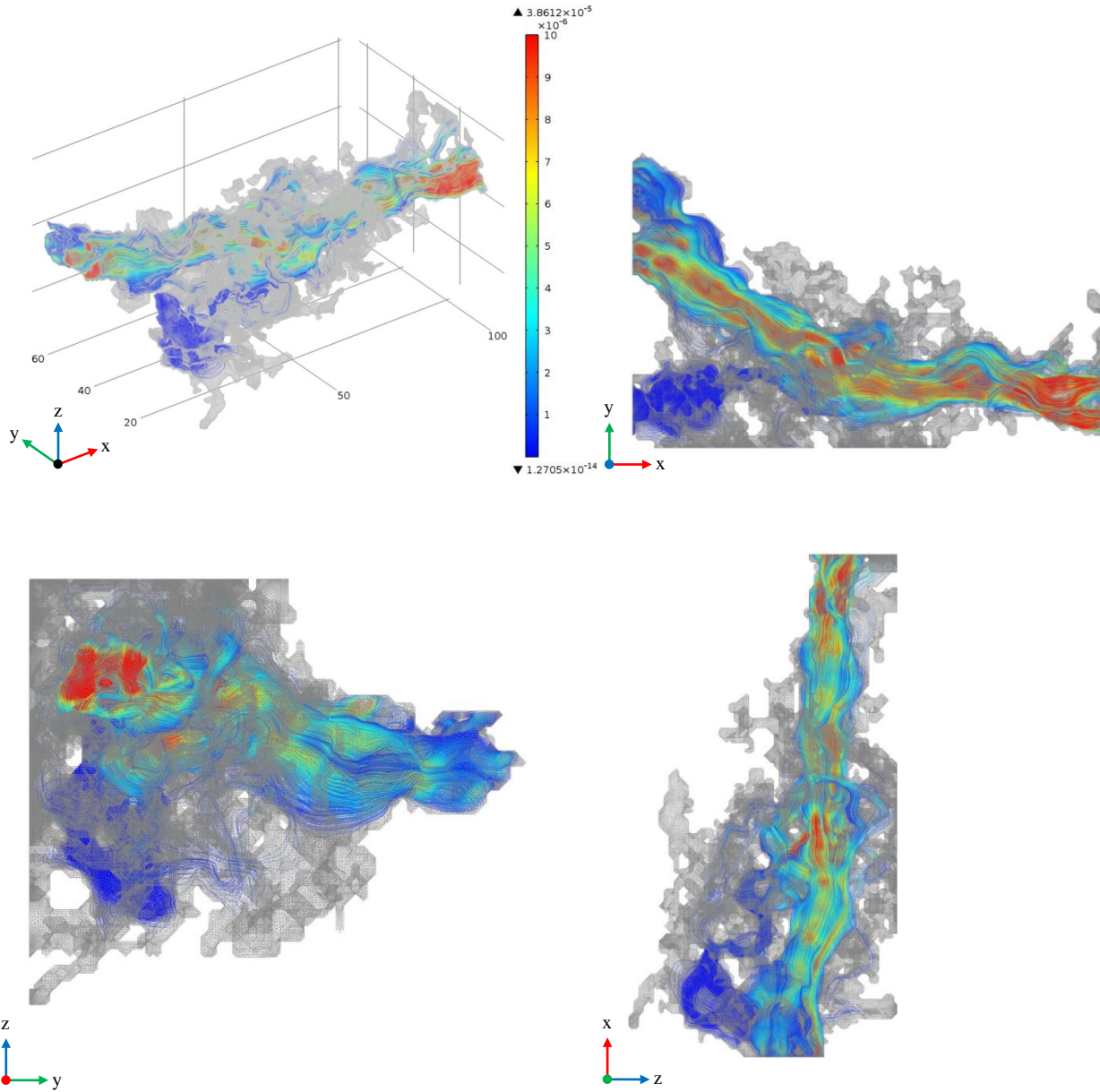


Figure 5.9 Flow diagrams from Model 8-x1 (non resampled). The subsample size is 100^3 voxels³ ($745^3 \mu\text{m}^3$) with a CMT resolution of $7.45 \mu\text{m}$.

In Figure 5.10, the electrical current density field is shown with 5,000 streamlines with the color representing the current density normalized from ~ 0 to 0.02 (A/voxel^2). Current entered from the left yz face and exited the x+ direction.

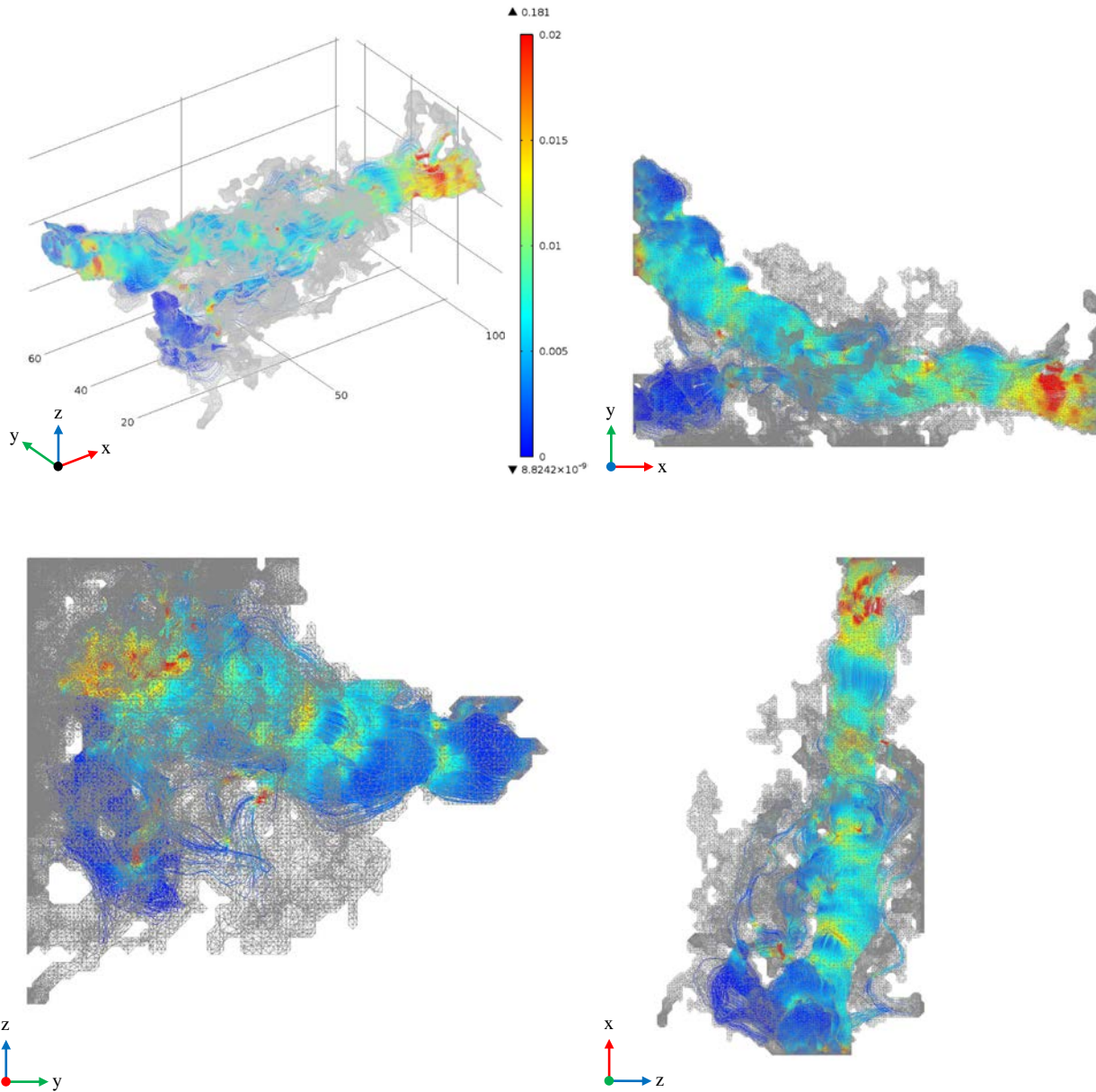


Figure 5.10 Electrical current density diagrams from Model 8-x1 (non resampled). The subsample size is 100^3 voxels³ ($745^3 \mu\text{m}^3$) with a CMT resolution of $7.45 \mu\text{m}$.

The current density simulation used in [Model 8] used the default STL relative tolerance of 10^{-6} with automatic face partitioning. An iterative multigrid solver with a free tetrahedral mesh was used. The fluid flow simulation used in [Model 8] used the default STL relative tolerance of 10^{-6} with automatic face partitioning. A direct solver with a free tetrahedral mesh was used. The simulation used 31.5 GB of RAM including 36 GB of virtual memory. The time to complete the fluid simulation was 13.8 minutes. The number of equations solved was 3,147,436 and the error was 0.2% for all simulations.

A summary of the cropped subsample locations, used in Results 2, are listed in Table 5.6. The regions can be used by future researchers for additional permeability investigations within the Weyburn reservoir.

Table 5.6 Subsample Volumes used in Results 2

Model	Sample Volume (voxels ³)	x-direction region	y-direction region	z-direction region
5	30	500 to 530	500 to 530	0 to 30
6	100	1250 to 1350	1450 to 1550	0 to 100
7	200	1200 to 1400	1400 to 1600	20 to 220
8	100	1100 to 1200	700 to 800	0 to 100
8*	71	1100 to 1200	700 to 760	45 to 105

5.8 Darcy Velocity Scaling to Reservoir Conditions

Similar to the Darcy velocity scaling used in Section 4.3, a comparison of the calculated Darcy velocity and the Darcy velocity at representative in-situ conditions at an injection well was completed for the Vuggy (V6) rock (Carroll et al., 2011). Calculations of the Darcy velocity were completed using the same Vuggy (V6) core as listed in section 5.1. Hereafter, the term Vuggy will refer to the calculated sample, and the term Vuggy (V6) will refer to the laboratory measured sample.

Table 5.7 shows the Darcy velocity comparison so that the Darcy velocity of the Vuggy data can be scaled to represent reservoir conditions. The Vuggy (V6) rock has a sample diameter of

15 mm, a sample length of 30 mm and a flow rate of 0.05 ml/min ($8.33 \times 10^{-10} \text{ m}^3/\text{s}$). The Darcy velocity was calculated as the fluid flow rate divided by the sample area. To estimate representative in-situ conditions, the pressure gradient for the Vuggy (V6) sample was used with a viscosity of $9.00 \times 10^{-4} \text{ Pa}\cdot\text{s}$ (Glemser, 2007). The Darcy velocity range listed was calculated using the data from [Model 8]. The scale factor is the ratio of the calculated Vuggy and Vuggy (V6) Darcy velocities.

Table 5.7 Darcy Velocity Comparison for Vuggy (V6) Core Sample

Vuggy (V6) (Sample #)	Pressure Gradient* (kPa/m)	Total Porosity* (%)	Darcy Velocity* (m/s)	Darcy Velocity Range Vuggy (m/s)	Scale Factor (Vuggy / Vuggy (V6))
1	2526.3	15.3%	4.72 e-6	2.56 e-2 to 7.10 e-2	5,424 to 15,066

* Vuggy (V6) data (Carroll et al., 2011)

The scale factor for the Darcy velocity ranges from 5,424 to 15,066. This scale factor can be used to multiply the Vuggy Darcy velocity and give a quasi-representative Darcy velocity of in-situ reservoir conditions at an injection well.

The permeability of the Vuggy ranges from 343.26 mD to 953.49 mD, as listed in Table 5.5. The laboratory measured permeability for the Vuggy (V6) sample was initially 0.26 mD. The sample was run until CO_2 dissolution reduced the differential pressure across the core unit to 10% of its initial value with a final permeability of 2.60 mD.

The subsample chosen for the calculations may not be representative as only a single calculation was completed. This subsample also had connected porosity, and permeability in the x+ direction. The y direction and z direction were not connected. It is also possible that the CMT resolution of $7.45 \mu\text{m}$ was not small enough to resolve the pore structure. The permeability is also known to vary substantially between subsections for Vuggy rock. Considering the above, and that my subsample was randomly isolated from a larger subsample volume, it is understandable that the permeability values vary.

Regions within Sample 1E may not be valid for the Darcy approximation under reservoir conditions. Other models, such as Stokes or Darcy-Brinkman may better suite represent the transport properties because the pore spaces are very large (Carroll et al., 2011). The Darcy

approximation was only valid for the small pressure difference used in my calculations. Depending on the laboratory equipment, the calculated results may not be possible to achieve in a laboratory setting as a small pressure gradient is required.

5.9 Resampling Observations

From the resampling investigation, several observations were made. The observations are included as they may be helpful for future research involving resampling data.

1. The resampled images should be compared to non-resampled images to ensure the permeability remains essentially the same.
2. The resampling process can be used to smooth the surface of the pore space and rock matrix boundary to make the calculation of transport properties easier to solve on a computer. To help save time, before calculating the permeability, the porosity could easily be calculated for the non-resampled and resampled images to determine a porosity change. Consideration of the amount of resampling required should be based on the type of rock used, complexity of the mesh geometry and amount of computer memory available.
3. Resampling should be completed after thresholding the image. If the image is thresholded after resampling, the images cannot be directly compared for permeability changes.
4. Higher values of resampling should be limited to larger sub-volumes with larger pores as the intent is to smooth the surface while preserving the main fluid pathways inside the pore space geometry. Higher resampling for smaller sub-volumes can change the pore-throat and significantly modify the CMT data and associated transport properties.

5.10 Summary for Results 2, Post CO₂ Flood Sample (7.45 μm)

For Results 2, a 7.45 μm resolution CMT data sample was used for a Vuggy (V6) rock that had been exposed to CO₂. The CO₂ dissolution of the rock matrix resulted in large visible pore spaces. The largest pore was isolated to calculate the maximum permeability. The permeability for the large pore could not be calculated due to computer memory limitations. To calculate the permeability, resampling the CMT data was used to smooth the surface of the rock pore matrix to allow for a simplified mesh to fit into the finite computer memory.

The resampling process was investigated using the 0.78 μm CMT resolution data for Marly rock, used in Results 1. The permeability values following the resampling process from 1.0x to 3.0x are all within one order of magnitude. The pore space changed, but the main fluid pathways inside the pore space geometry was preserved. For 4.0x resampling, the pore space was not connected.

The workflow, as used in Results 1, was modified to include resampling after importing the data in [Model 6]. Thresholding a 100 voxel (745 μm) subsection was completed using a visible connected pore region on the resampled CMT data. The data was resampled from 1.0x (non-resampled) to 8.0x to determine the permeability change associated with resampling. All permeability results are within the same order of magnitude, with a total permeability change of 29%. The number of mesh elements and the simulation time were significantly reduced when using resampled data. The simulation time used to compute the permeability for the 8.0x resampled data was approximately 277 times shorter than the simulation time used to compute the permeability for the 1.0x resampled data.

The workflow used in [Model 6] was modified to include resampling after thresholding and filtering the data for [Model 7]. The resampling was completed for a 200 voxel (1490 μm) region. This was the same region used in [Model 6], but expanded by 50 voxels in each direction. The resampling was then completed from 2.0x to 10.0x. All permeability results are within the same order of magnitude, with a total permeability change of 69%. As the main fluid flow is located within the 100 voxel region, the calculated permeability results are similar for both, with differences associated with thresholding values estimated. Future thresholding should be completed with an Avizo workflow with resampling completed after thresholding.

A randomly isolated subsample was used to provide a permeability estimate that is more representative of the rock matrix. The calculated permeability for the non-resampled 100 voxel (7.45 μm) subsample ranged from 343.26 to 953.49 mD. A comparison of the calculated Darcy velocity and the Darcy velocity at representative in-situ conditions at an injection well was completed for the Vuggy (V6) rock (Carroll et al., 2011). The scale factor the Darcy velocity ranges from 5,424 to 15,066. The laboratory measured permeability for the Vuggy (V6) sample was run until CO₂ dissolution reduced the differential pressure across the core unit with a final permeability of 2.60 mD. The subsample chosen for the calculations is likely not representative as only a single calculation was completed.

6 OVERALL SUMMARY

The objective of this thesis was to develop a workflow in order to determine the transport properties and visualize the fluid flow and electrical current density in a reservoir drill core of a Midale Marly and a Vuggy Shoal rock. The workflow started by using CMT data that provided us with high resolution three-dimensional images of the reservoir rocks taken from drill cores in the Weyburn oil field. The workflow included thresholding, binarizing, filtering, and extracting the porous network from the Synchrotron X-ray Computed Microtomography (CMT) data using Avizo Fire. A three-dimensional finite element mesh, representing the pore spaces, was then used to obtain the solution of the Navier-Stokes equations for an incompressible fluid and Laplace's equation for electrical current flow using COMSOL.

The combination of synchrotron CMT data, Avizo Fire and COMSOL Multiphysics is a powerful toolset that was used to estimate the transport properties of rocks. The transport properties of Midale Marly (MO) and Vuggy Shoal (V6) rock core samples were completed using laboratory measurements of transport properties. These samples were later imaged using synchrotron X-ray computed microtomography. The laboratory measured transport properties were compared with calculated transport properties on a smaller sub-volume of the same rock core imaged using the CMT data.

In the work completed by Glemser (2007), laboratory measurements of porosity, permeability, resistivity and formation resistivity factor were completed using a large diameter core. A smaller CMT core sample, taken from inside the large diameter core, was imaged using CMT data. The CMT data enabled the porosity to be calculated using the greyscale image. The permeability was estimated by using mercury injection porosimetry to find the critical pore diameter and the Katz-Thomson equation, equation 1.3, was used to estimate the permeability (Glemser 2007). In the workflow I created, the porosity, permeability, resistivity and formation resistivity factor were directly calculated using commercially available software. Minor changes to the workflow can also be applied to investigate physical properties that cannot be obtained using the large diameter laboratory rock core. Such simulations could include investigating hydrodynamic dispersion and the transport of chemical species, as well as the reactions of the chemical species. Multiphase flow could also be considered to simulate the CO₂

and brine used in the Weyburn oilfield. The rock could also be meshed to simulate thermal conductivity and elastic properties.

Based on statistical analysis of the porosity for this study, the side length for a cubic REV for porosity is estimated to be roughly between 78 and 156 μm (100 and 200 voxels). Due to computer memory constraints, we could only analyze a 24 μm (50 voxel) subsample. The 156 μm (200 voxel) region is estimated to generate over 100 million equations to solve for a flow simulation and was beyond current computer memory limitations.

The steady state incompressible fluid flow through the porous network was first verified to be in the Darcy flow regime. Solutions of the Navier-Stokes equations were computed with different inlet pressures for the same pore geometry in order to confirm a direct proportionality between the mass fluid flux, q , and pressure, p , as Darcy's Law specifies. A pressure gradient change between inlet and outlet sections resulted in a proportional mass fluid flux change for all samples used. The computed macroscopic results were then compared with laboratory measurements to check the validity of the developed workflow created using imaged synchrotron CMT data.

Laboratory measurements and calculations were completed by Glemser (2007) for the Midale rock core. The measured permeability was obtained using a Ruska Liquid Permeameter, with a permeability of 7.7 mD. The formation resistivity factor and cementation exponent were found to be 11.71 and 1.87 respectively.

Using Avizo Fire, I extracted the pore space and used COMSOL Multiphysics to solve the Navier-Stokes equations for the fluid flow and Laplace's equation for the electrical current density.

For Results 1 (i.e., 0.78 μm resolution Marly), the calculations were completed using a smaller sub-volume of the same core sample that Glemser (2007) used. The permeability ranged from 0.1 to 3.5 mD for [Model 1] to [Model 4]. The samples were verified to be nearly isotropic as the permeability was similar for three orthogonal fluid flow directions. The calculated formation resistivity factor ranged from 29.3 to 309. The cementation exponent was calculated to range between 1.99 to 2.10. The laboratory measured properties are roughly within one order of

magnitude compared to previously completed laboratory analysis completed by Glemser (2007). The previously completed laboratory analysis and my calculated permeability both follow the same power law trend line as predicted by the Kozeny-Carmen equation.

A comparison of the calculated Darcy velocity between the Marly (M0) rock and the Marly (M3) rock was completed. The Marly (M3) Darcy velocity is representative of in-situ conditions at an injection well (Carroll et al., 2011). The scale factor of the Darcy velocity ranges from 0.04 to 2.10.

The developed workflow, using Avizo Fire and COMSOL Multiphysics, results in calculated porosity, permeability, formation resistivity factor and cementation exponent that are within one order of magnitude of the measured properties completed on the larger laboratory samples by Glemser (2007). The workflow developed appears to be an acceptable combination for determining the transport properties of rocks.

For Results 2 (i.e, 7.45 μm resolution Vuggy), a Vuggy Shoal sample was investigated after the sample had been exposed to CO_2 , and dissolution within the rock matrix resulted in large visible pore spaces. CMT analysis was completed on a sub-volume of the original core to capture the largest visible pore. The permeability for the large pore could not be calculated using the previous workflow due to computer memory limitations. To fit the sample within the available computer memory, resampling of the data was investigated which included a modified workflow to include smoothing the surface of the pore space and rock matrix boundary. The modified workflow was completed using [Model 4] in Results 1. The permeability values following the resampling process from 1.0x to 3.0x are all within one order of magnitude. The permeabilities ranged from 3.40 mD to 2.30 mD. A 100 voxel (745 μm) region, [Model 6], was then isolated to estimate the largest permeability after the CO_2 dissolution. The permeability values following the resampling process from 1.0x to 8.0x ranged from $2.28 \cdot 10^6$ to $3.21 \cdot 10^6$ mD.

The workflow was then modified to include resampling a 200 x 200 x 200 voxel (1490 x 1490 x 1490 μm) region before thresholding the data. The permeability values ranged from $8.57 \cdot 10^5$ to $2.65 \cdot 10^5$ mD for resampling from 2.0x to 10.0x. This modified workflow, used only for the 200 voxel region, was not recommended due to variations in thresholding.

A randomly isolated 100 x 100 x 100 voxel (745 x 745 x 745 μm) region was then investigated with a calculated permeability of 343.26 to 953.49 mD. The formation resistivity factor ranged from 41.94 to 116.51 and the cementation exponent ranged from 1.30 to 1.42. The modified workflow, including resampling, was successfully used to smooth the surface between the pore space and rock matrix. This enabled the data to fit into the available computer memory with calculated permeabilities within the same order of magnitude as non-resampled images.

A comparison of the calculated Darcy velocity and the Darcy velocity at representative in-situ conditions at an injection well was completed for the Vuggy (V6) rock (Carroll et al., 2011). The scale factor for the Darcy velocity ranges from 5,424 to 15,066. The laboratory measurements for the Vuggy (V6) sample were run until CO_2 dissolution reduced the differential pressure across the core unit with a final permeability of 2.60 mD. The subsample chosen for the calculations may not be representative as only a single calculation was completed. This subsample also had connected porosity, and permeability only in the x+ direction. The y direction and z direction were not connected. It is also possible that the CMT resolution of 7.45 μm was not small enough to resolve the pore structure. The permeability is also known to vary substantially between subsections for Vuggy rock.

6.1 Recommendations for Future Research

From this study, the following recommendations can be made for future research. These recommendations should be used in conjunction with Glemser's (2007) thesis recommendations.

1. When importing the geometry into a simulation package, such as COMSOL, it is beneficial to scale the units appropriately to generate the desired output units. The units used in this work were scaled after simulations, but could have easily been completed during the initial program setup. The units cannot be easily changed after the simulations have completed since the 3D mesh representing the pore space has to be regenerated. The meshes took a long time to generate correctly and were likely the most challenging task in this work.
2. The future workflow can be refined to include additional thresholding investigation. The thresholding used for this work was previously completed using thin sections viewed under cross polarized light, EPMA on carbonate thin sections and BSE imaging to resolve the mineral composition as completed by Glemser (2007). Thresholding ambiguity of the pore space could be checked by investigating the grey scale value at the outside edge of the CMT data. The grey scale value between the rock and the air interface could be used as a calibration for the pore space grey scale range. Thresholding research should include additional thresholding tools, such as the watershed segmentation within Avizo Fire. Watershed segmentation is a technique for simulating flooding on labeled 3D regions in an image. The grey level of the voxel can be observed as the topographic relief. Local minimum areas are calculated to give basins where water will flow. The watershed algorithm should be investigated before calculating the transport properties.
3. Thresholding can be used to isolate minerals along with the pore space. If minerals are included in the workflow, the minerals could be meshed separately and chemical reactions could be applied to simulate CO₂ dissolution of the rock matrix.
4. Minor changes to the workflow can also be applied to investigate multiphase flow to simulate the CO₂ and brine used in the Weyburn oilfield. Hydrodynamic dispersion and

the transport of chemical species, as well as the reactions of the chemical species could be investigated. The rock could also be meshed to simulate thermal conductivity and elastic properties. Gas flow could also be completed by incorporating different boundary conditions somewhere between a no slip and full slip boundary.

5. The magnitude of permeability change can be investigated by expanding/contracting all subsample voxels to simulate potential dissolution/precipitation respectively while comparing results prepared by Susan Carroll and her collaborators at Livermore.
6. New randomly isolated sub-samples can be investigated using the existing data. The location of the data could be completed by using a random number generator to isolate the subsection volume so that a representative sample is calculated. A representative sample should have a similar porosity to the whole sample. Calculated properties for these subsamples could be compared to these thesis results.
7. As my work progressed, newer versions of Avizo and COMSOL were used that incorporated new features for handling the complex 3D mesh generation. Additional output files for Avizo and input files for COMSOL should be investigated to help generate 3D volume meshes without having to the implement manual mesh fixes. Third party STL file format repair software is available. This repair software could be useful for saving time and improving the workflow to account for manual mesh fixes.
8. Investigate new capabilities of Avizo Fire. Newer Avizo versions include new modules, called XLAB HYDRO to calculate absolute permeability and XLAB ELECTRO to calculate the electrical resistivity and formation factor. There is also a module called XLAB THERMO to calculate the thermal conductivity and XLAB DIFFUSION to calculate the molecular diffusivity. XLAB modules also incorporate GPU technology, so the computation speed is greatly increased. Avizo also has additional filters, such as a filter for removing beam hardening from CMT data.
9. Alternative software to COMSOL Multiphysics is ANSYS Fluent. Fluent is capable of modeling multiphase flows and chemical reactions (ANSYS Fluent, 2013). Fluent also can use CAD software where new file formats to represent the pore space may be available.

10. Investigate larger samples and calculate the permeability for an REV. Computer power and RAM availability has significantly increased since this work was started. Using a new computer combined with the latest software may enable larger subsamples to be calculated and a REV permeability to be calculated directly.
11. For future CMT imaging, the use of a marker, such as a magnet, on the core sample will enable the user to correlate the permeability core sample and the CMT core sample. This will also allow for sections of the CMT data to be correlated to determine sections of overlap.
12. Investigate other solver methods, such as LBM and FDM.
13. See Appendix C - Computer Specifications for potential hardware and software necessary to complete simulations. Also check the software websites for up to date recommended system specifications.

REFERENCES

- Al-Mjeni, R., Arora, S., Cherukupalli, P., van Wunnik, J., Edwards, J., Felber, B., . . .
Ramamoorthy, R. (2011). Has the time come for EOR? *Oilfield Review (Winter 2010/2011)*, 22(4)
- Al-Raoush, R. I., & Willson, C. S. (2005). Extraction of physically realistic pore network properties from three-dimensional synchrotron X-ray microtomography images of unconsolidated porous media systems. *Journal of Hydrology*, 300(1–4), 44-64. doi: 10.1016/j.jhydrol.2004.05.005
- ANSYS Fluent. (2013). Retrieved November 19, 2013, from
<http://www.ansys.com/Products/Simulation+Technology/Fluid+Dynamics/Fluid+Dynamics+Products/ANSYS+Fluent>
- Archie, G. E. (1942). The electrical resistivity log as an aid in determining some reservoir characteristics. *Transactions of the AIME*, 146, 54-62.
- Baveye, P. C., Laba, M., Otten, W., Bouckaert, L., Dello Sterpaio, P., Goswami, R. R., . . .
. Sezgin, M. (2010). Observer-dependent variability of the thresholding step in the quantitative analysis of soil images and X-ray microtomography data. *Geoderma*, 157(1–2), 51-63. doi: 10.1016/j.geoderma.2010.03.015
- Blunt M.J., B. Bijeljic, H. Dong, O. Gharbi, S. Iglauer, P. Mostaghimi, A. Paluszny, C. Pentland, Pore-scale imaging and modelling, *Advances in Water Resources*, 51, 197-216, <http://dx.doi.org/10.1016/j.advwatres.2012.03.003>, 2013

- Bogner, A., Jouneau, P. H., Thollet, G., Basset, D., & Gauthier, C. (2007). A history of scanning electron microscopy developments: Towards “wet-STEM” imaging. *Micron*, 38(4), 390-401. doi: 10.1016/j.micron.2006.06.008
- Carroll, S., Smith, M., Sholokhova, Y., & Hao, Y. (2011). An experimental and modeling study. enhanced porosity in carbonate rocks for the Weyburn CO2 storage project.
- Churcher, P. L., & Edmunds, A. C. (1994). Reservoir characterization and geological study of the Weyburn unit, southeastern Saskatchewan: Report number 1, proposed miscible flood, horizontal well, and waterflood optimization areas; internal report prepared for PanCanadian Petroleum Ltd., 28p.
- Combes, R., Robin, M., Blavier, G., Aidan, M., & Degrève, F. (1998). Visualization of imbibition in porous media by environmental scanning electron microscopy: Application to reservoir rocks. *Journal of Petroleum Science and Engineering*, 20(3–4), 133-139. doi: 10.1016/S0920-4105(98)00012-6
- COMSOL Multiphysics. (2011c). *What does degrees of freedom (DOF) mean in COMSOL multiphysics?* Retrieved March 23, 2013c, from <http://www.comsol.com/support/knowledgebase/875/>
- COMSOL Multiphysics. (2012b). *What hardware do you recommend for COMSOL multiphysics?* Retrieved August 21, 2012b, from <http://www.comsol.com/support/knowledgebase/866/>
- Doveton, H. J. (1999). In Kansas Geological Survey (Ed.), *Basics of oil & gas log analysis* Doveton.

- ESRF / P. Ginter. (2012). *What is a synchrotron?* Retrieved November 28, 2012, from <http://www.esrf.eu/about/synchrotron-science/synchrotron>
- Glemser. (2007). Petrophysical and geochemical characterization of midale carbonates from the Weyburn oilfield using synchrotron X-ray computed microtomography.
- Kinney, J. H., & Nichols, M. C. (1992). X-ray tomographic microscopy (XTM) using synchrotron radiation. *Annual Review of Materials Science*, 22(1), 121-152. doi: 10.1146/annurev.ms.22.080192.001005
- Kotzer, T., & Hawkes, C. (2012). Studying the Effects of CO₂ Exposure on Pore-Scale Mineral Alterations in Carbonates from the Weyburn Field Using Microtomographic Imaging Techniques, reported submitted to the Petroleum Technology Research Centre, Regina, Canada, December 2012.
- Loucks, R. G., Reed, R. M., Ruppel, S. C., & Jarvie, D. M. (2009). Morphology, genesis, and distribution of nanometer-scale pores in siliceous mudstones of the mississippian barnett shale. *79*(12), 848-848-861.
- Montemagno, C., & Gray, W. (1996). Photoluminescent volumetric imaging: A technique for the exploration of multiphase flow and transport in porous medi : G. D. montemagno & W. G. gray, *geophysical research letters*, 22(4), 1995, pp 425–428. *International Journal of Rock Mechanics and Mining Sciences & Geomechanics Abstracts*, 33(2), A59-A60. doi: 10.1016/0148-9062(96)83835-6

- Moretto, P., Michelet, C., Le Gallet, S., Rebillat, F., Guette, A., & Vignoles, G. (2001). STIM tomography: A potential tool for the non-destructive characterisation of SiC microcomposite materials. *Nuclear Instruments and Methods in Physics Research Section B: Beam Interactions with Materials and Atoms*, 181(1–4), 238-243. doi: 10.1016/S0168-583X(01)00461-X
- Mostaghimi, P., M. Blunt and B. Bijeljic, Computations of Absolute Permeability on Micro-CT Images, *Math. Geosci.*, 45, 103-125, 2013.
- Pauli, J., Scheying, G., Mugge, C., Zschunke, A., & Lorenz, P. (1996). Determination of the pore widths of highly porous materials with NMR microscopy.
- Piller, M., Schena, G., Nolich, M., Favretto, S., Radaelli, F., & Rossi, E. (2009). Analysis of hydraulic permeability in porous media: From high resolution x-ray tomography to direct numerical simulation. *Transport in Porous Media*, 80(1), 57-78.
- R. Eymard, T Gallouët and R. Herbin. (2006). Finite volume methods - this manuscript is an update of the preprint which appeared in handbook of numerical analysis. [This manuscript is an update of the preprint n0 97-19 du LATP, UMR 6632, Marseille, September 1997 which appeared in Handbook of Numerical Analysis, P.G. Ciarlet, J.L. Lions eds, vol 7, pp 713-1020]
- Royal Canadian Mint. (2012). *Striking in its solitude – the 1-dollar coin, familiarly known as the 'loonie'*. Retrieved November 27, 2012, from http://www.mint.ca/store/mint/learn/1-dollar-5300014#1D_1

- Rypl, D., & Bittnar, Z. (2006). Generation of computational surface meshes of STL models. *Journal of Computational and Applied Mathematics*, 192(1), 148-151. doi: 10.1016/j.cam.2005.04.054
- Selomulya, C., Jia, X., & Williams, R. A. (2005). Direct prediction of structure and permeability of flocculated structures and sediments using 3D tomographic imaging. *Chemical Engineering Research and Design*, 83(7), 844-852. doi: 10.1205/cherd.04330
- Simon, R. (1981). Enhanced oil recovery: Definitions, fundamentals, applications, and research frontiers. *Physics and Chemistry of the Earth*, 13-14(0), 447-460. doi: 10.1016/0079-1946(81)90022-7
- Stroud, I., & Xirouchakis, P. C. (2000). STL and extensions. *Advances in Engineering Software*, 31(2), 83-95.
- Turcotte, D., & Schubert, G. (2001). Fluid mechanics. *Geodynamics* (2nd ed., pp. 232) Cambridge.
- Visualization Sciences Group. (2010a). Avizo Fire 6.3 reference guide.
- Visualization Sciences Group. (2010b). Avizo Fire 6.3 users guide.
- Visualization Sciences Group. (2012). *Avizo, high-performance 3D visualization and GPU computing*. Retrieved August 21, 2012, from <http://www.vsg3d.com/solutions/high-performance-3d-visualization-and-gpu-computing>

- Wark, D. A., & Watson, E. B. (1998). Grain-scale permeabilities of texturally equilibrated, monomineralic rocks. *Earth and Planetary Science Letters*, 164(3–4), 591-605. doi: [http://dx.doi.org/10.1016/S0012-821X\(98\)00252-0](http://dx.doi.org/10.1016/S0012-821X(98)00252-0)
- Wegelin, A. (1984). Geology and reservoir properties of the Weyburn field, southeastern Saskatchewan.(Saskatchewan Geological Society Special Publication Number 7), 71-84.
- Werth, C. J., Zhang, C., Brusseau, M. L., Oostrom, M., & Baumann, T. (2010). A review of non-invasive imaging methods and applications in contaminant hydrogeology research. *Journal of Contaminant Hydrology*, 113(1–4), 1-24. doi: 10.1016/j.jconhyd.2010.01.001
- Whittaker, S., Rostron, B., Hawkes, C., Gardner, C., White, D., Johnson, J., . . . Seeburger, D. (2011). A decade of CO₂ injection into depleting oil fields: Monitoring and research activities of the IEA GHG Weyburn-Midale CO₂ monitoring and storage project. *Energy Procedia*, 4(0), 6069-6076. doi: 10.1016/j.egypro.2011.02.612
- Wildenschild, D., Sheppard, A., X-ray imaging and analysis techniques for quantifying pore-scale structure and processes in subsurface porous medium systems, *Adv. Water Resour.*, 51, 217-246, 2013.
- Wilson, M., & Monea, M.,. (2004). Weyburn CO₂ monitoring and storage project summary report 2000-2004. *From the Proceedings of the 7th International Conference on Greenhouse Gas Control Technologies*, Edited by M. Wilson, M. Monea, Petroleum Technology Research Centre, Regina.

Appendix A

Representative Elementary Volume

Table 1.1A Porosity change for random 200 voxel regions

Sample Number	Sample Volume (voxels ³)	Sample Length (μm)	Total Porosity (%)	x-direction region	y-direction region	z-direction region
1	200	156	29.22%	1500 to 1700	1500 to 1700	0 to 200
2	200	156	30.97%	1200 to 1400	1600 to 1800	55 to 255
3	200	156	30.54%	600 to 800	1300 to 1500	25 to 225
4	200	156	27.96%	300 to 500	1000 to 1200	55 to 255
5	200	156	30.43%	800 to 1000	1100 to 1300	0 to 200
6	200	156	26.38%	700 to 900	750 to 950	55 to 255
7	200	156	33.69%	1150 to 1350	450 to 650	25 to 225
8	200	156	29.46%	1450 to 1650	625 to 825	0 to 200
9	200	156	33.18%	720 to 920	375 to 575	25 to 225
10	200	156	31.45%	425 to 625	800 to 1000	20 to 220
11	200	156	32.30%	600 to 800	1400 to 1600	0 to 200
12	200	156	26.80%	900 to 1100	700 to 900	0 to 200
13	200	156	28.54%	1300 to 1500	200 to 400	0 to 200
14	200	156	19.39%	1600 to 1800	400 to 600	25 to 225
15	200	156	30.29%	400 to 600	300 to 500	0 to 200
16	200	156	27.15%	1550 to 1750	1100 to 1300	55 to 255
17	200	156	29.77%	200 to 400	850 to 1450	0 to 220
18	200	156	26.48%	1350 to 1550	1550 to 1750	20 to 220
19	200	156	28.61%	900 to 1100	200 to 400	25 to 225
20	200	156	32.61%	350 to 550	1450 to 1650	30 to 230

Standard Deviation = 2.85%

Average porosity = 29.26% (Minimum 24.40%, Maximum 33.85%, Median 30.23%)

Table 1.2A Porosity change for random 100 voxel regions

Sample Number	Sample Volume (voxels ³)	Sample Length (μm)	Total Porosity (%)	x-direction region	y-direction region	z-direction region
1	100	78.0	34.15%	338 to 438	560 to 660	71 to 171
2	100	78.0	31.12%	371 to 471	1496 to 1596	20 to 120
3	100	78.0	27.45%	243 to 343	1501 to 1601	126 to 226
4	100	78.0	24.57%	1546 to 1646	1151 to 1251	24 to 124
5	100	78.0	32.63%	493 to 593	705 to 805	108 to 208
6	100	78.0	26.00%	575 to 675	1605 to 1705	33 to 133
7	100	78.0	28.01%	75 to 175	794 to 894	76 to 176
8	100	78.0	28.27%	905 to 1005	488 to 588	20 to 120
9	100	78.0	38.29%	330 to 430	1407 to 1507	52 to 152
10	100	78.0	32.28%	771 to 871	1284 to 1384	107 to 207
11	100	78.0	34.25%	1174 to 1274	318 to 418	73 to 173
12	100	78.0	24.19%	513 to 613	191 to 291	124 to 224
13	100	78.0	24.91%	1535 to 1635	722 to 822	28 to 128
14	100	78.0	29.85%	974 to 1074	605 to 705	78 to 178
15	100	78.0	25.09%	809 to 909	946 to 1046	3 to 103
16	100	78.0	24.91%	236 to 336	1223 to 1323	111 to 211
17	100	78.0	19.25%	895 to 995	622 to 722	66 to 166
18	100	78.0	20.80%	1638 to 1738	1049 to 1149	18 to 118
19	100	78.0	33.69%	1304 to 1404	1563 to 1663	134 to 234
20	100	78.0	26.92%	1522 to 1622	486 to 586	46 to 146

Standard Deviation = 4.89%

Average porosity = 28.33% (Minimum 19.25%, Maximum 38.29%, Median 27.73%)

Table 1.3A Porosity change for random 50 voxel regions

Sample Number	Sample Volume (voxels ³)	Sample Length (μm)	Total Porosity (%)	x-direction region	y-direction region	z-direction region
1	50	39.0	15.58%	412 to 462	295 to 345	101 to 151
2	50	39.0	22.16%	351 to 401	686 to 736	162 to 212
3	50	39.0	21.70%	1617 to 1667	662 to 712	140 to 190
4	50	39.0	20.95%	536 to 586	1036 to 1086	133 to 183
5	50	39.0	27.90%	910 to 960	446 to 496	162 to 212
6	50	39.0	28.73%	1108 to 1158	1042 to 1092	63 to 113
7	50	39.0	29.22%	516 to 566	1085 to 1135	40 to 90
8	50	39.0	38.81%	1292 to 1342	1696 to 1746	162 to 212
9	50	39.0	27.34%	929 to 979	1122 to 1172	171 to 221
10	50	39.0	41.83%	935 to 985	1421 to 1471	100 to 150
11	50	39.0	17.16%	647 to 697	1806 to 1856	63 to 113
12	50	39.0	13.47%	1378 to 1428	827 to 877	46 to 96
13	50	39.0	11.93%	1450 to 1500	1238 to 1288	35 to 85
14	50	39.0	46.65%	62 to 112	815 to 865	18 to 68
15	50	39.0	15.18%	1003 to 1053	792 to 842	187 to 237
16	50	39.0	11.03%	481 to 531	1648 to 1698	102 to 152
17	50	39.0	19.51%	673 to 723	1890 to 1940	168 to 218
18	50	39.0	28.30%	922 to 972	265 to 315	76 to 126
19	50	39.0	18.56%	1453 to 1503	1630 to 1680	4 to 54
20	50	39.0	36.01%	1650 to 1700	661 to 711	71 to 121

Standard Deviation = 10.18 %

Average porosity = 24.60% (Minimum 11.03%, Maximum 46.65%, Median 21.93%)

Table 1.4A Porosity change for random 30 voxel regions

Sample Number	Sample Volume (voxels ³)	Sample Length (μm)	Total Porosity (%)	x-direction region	y-direction region	z-direction region
1	30	23.4	71.08%	1222 to 1252	1474 to 1504	15 to 45
2	30	23.4	13.31%	1788 to 1818	1385 to 1415	198 to 228
3	30	23.4	29.45%	454 to 484	1421 to 1451	8 to 38
4	30	23.4	36.24%	507 to 537	906 to 936	100 to 130
5	30	23.4	17.89%	1507 to 1537	391 to 421	152 to 182
6	30	23.4	39.78%	1264 to 1294	1351 to 1381	123 to 153
7	30	23.4	24.37%	1260 to 1290	555 to 585	103 to 133
8	30	23.4	10.24%	514 to 544	1722 to 1752	25 to 55
9	30	23.4	7.30%	437 to 467	1035 to 1065	143 to 173
10	30	23.4	12.73%	1484 to 1514	691 to 721	52 to 82
11	30	23.4	4.17%	379 to 409	905 to 935	47 to 77
12	30	23.4	18.40%	1402 to 1432	1387 to 1417	65 to 95
13	30	23.4	41.15%	803 to 833	1280 to 1310	66 to 96
14	30	23.4	1.99%	1343 to 1373	1299 to 1329	55 to 85
15	30	23.4	14.79%	372 to 402	1006 to 1036	57 to 87
16	30	23.4	9.30%	1185 to 1215	1019 to 1049	39 to 69
17	30	23.4	5.75%	609 to 639	1288 to 1318	21 to 51
18	30	23.4	16.69%	915 to 945	116 to 146	190 to 220
19	30	23.4	45.86%	483 to 513	1448 to 1478	142 to 172
20	30	23.4	15.34%	1683 to 1713	1789 to 1819	184 to 214

Standard Deviation = 17.38%

Average porosity = 21.79% (Minimum 1.99%, Maximum 71.08%, Median 16.01%)

Appendix B

Scaling Factors for Modifying Equations to Real World Values

Appendix B displays the Scaling Factors for Modifying Equations to Real World Values as listed in Table 4.1. The example shows how the calculated transport properties were obtained for [Model 1-y5].

Permeability Calculation:

$$u = -\frac{k dp}{\mu dx} \quad (\text{A 1.1})$$

Darcy velocity from inlet mass fluid flux:

$$q_{in} = \frac{\iint \vec{u} \cdot \vec{n} ds}{S} \quad (\text{A 1.2})$$

$$q_{in} = \frac{-0.175 \left[\frac{\text{voxel}^3}{s} \right] \cdot \left[\frac{0.78 \cdot 10^{-6} m}{\text{voxel}} \right]^3}{30 [\text{voxel}] \cdot 30 [\text{voxel}] \cdot \left[\frac{0.78 \cdot 10^{-6} m}{\text{voxel}} \right]^2} \quad (\text{A 1.3})$$

$$q_{in} = -1.515 \cdot 10^{-10} \left[\frac{m}{s} \right] \quad (\text{A 1.4})$$

Darcy velocity from outlet mass fluid flux:

$$q_{out} = \frac{\iint \vec{u} \cdot \vec{n} ds}{S} \quad (\text{A 1.5})$$

$$q_{out} = \frac{0.173 \left[\frac{\text{voxel}^3}{s} \right] \cdot \left[\frac{0.78 \cdot 10^{-6} m}{\text{voxel}} \right]^3}{30 [\text{voxel}] \cdot 30 [\text{voxel}] \cdot \left[\frac{0.78 \cdot 10^{-6} m}{\text{voxel}} \right]^2} \quad (\text{A 1.6})$$

$$q_{out} = 1.502 \cdot 10^{-10} \left[\frac{m}{s} \right] \quad (\text{A 1.7})$$

Darcy velocity average mass fluid flux:

$$q_{ave} = \frac{|q_{in}| + |q_{out}|}{2} \quad (\text{A 1.8})$$

$$q_{ave} = \frac{1.515 \cdot 10^{-10} \left[\frac{m}{s} \right] + 1.502 \cdot 10^{-10} \left[\frac{m}{s} \right]}{2} \quad (\text{A 1.9})$$

$$q_{ave} = 1.509 \cdot 10^{-10} \left[\frac{m}{s} \right] \quad (\text{A 1.10})$$

Permeability:

$$k = -\frac{\mu \cdot q_{ave}}{dp/dx} \quad (\text{A 1.11})$$

$$k = -\frac{[Pa \cdot s] \cdot 1.509 \cdot 10^{-10} \left[\frac{m}{s} \right]}{\left[\frac{Pa}{30 \text{ voxel}} \right] \cdot \left[\frac{\text{voxel}}{0.78 \cdot 10^{-6} m} \right]} \quad (\text{A 1.12})$$

$$k = 3.531 \cdot 10^{-15} m^2 \quad (\text{A 1.13})$$

$$1 \text{ Darcy } (D) = 9.869233 \cdot 10^{-13} m^2 (\sim 1 \mu m^2) \quad (\text{A 1.14})$$

$$1 \text{ mD} = 9.869233 \cdot 10^{-16} m^2$$

$$k \cong 3.5 \text{ mD} \quad (\text{A 1.15})$$

Formation Factor and Cementation Exponent:

Porosity:

$$\phi = \frac{\iiint dV}{V = volume} \quad (A 1.16)$$

$$\phi = \frac{4988 \text{ voxels}^3}{30 \text{ voxels} \cdot 30 \text{ voxels} \cdot 30 \text{ voxels}} \quad (A 1.17)$$

$$\phi = 18.5\% \quad (A 1.18)$$

Total Inlet Current:

$$I_{in} = \iint \vec{j} \cdot \vec{n} \, ds = \iint [-\sigma \nabla V] \cdot \vec{n} \, ds \quad (A 1.19)$$

$$I_{in} = -1.021 \cdot \frac{1}{\Omega \cdot m} \cdot \frac{V}{\text{voxel}} \cdot \text{voxel}^2 \quad (A 1.20)$$

$$I_{in} = -1.021 \left[\frac{A \cdot \text{voxel}}{m^2} \right] \quad (A 1.21)$$

Total Outlet Current:

$$I_{out} = \iint \vec{j} \cdot \vec{n} \, ds = \iint [-\sigma \nabla V] \cdot \vec{n} \, ds \quad (A 1.22)$$

$$I_{out} = 1.027 \left[\frac{A \cdot \text{voxel}}{m^2} \right] \quad (A 1.23)$$

Average Current:

$$I_{ave} = \frac{|I_{in}| + |I_{out}|}{2} \quad (\text{A 1.24})$$

$$I_{ave} = 1.024 \left[\frac{A \cdot voxel}{m^2} \right] \quad (\text{A 1.25})$$

Resistance:

$$R = \frac{V}{I} = \frac{V}{I_{ave}} \quad (\text{A 1.26})$$

$$R = \frac{1 [V = volt]}{1.024 \left[\frac{A \cdot voxel}{m} \right]} = \frac{\Omega \cdot m}{1.024 \cdot voxel} \quad (\text{A 1.27})$$

$$R = 0.977 \left[\frac{\Omega \cdot m}{voxel} \right] \quad (\text{A 1.28})$$

Resistivity:

$$\rho = R \frac{A}{L} \quad (\text{A 1.29})$$

$$\rho = 0.977 \left[\frac{\Omega \cdot m}{voxel} \right] \cdot \frac{(30 \text{ voxel})^2}{30 \text{ voxel}} = 0.977 \left[\frac{\Omega \cdot m}{voxel} \right] \cdot 30 \text{ voxel} \quad (\text{A 1.30})$$

$$\rho = 29.3 [\Omega \cdot m] \quad (\text{A 1.31})$$

Formation resistivity factor:

$$F = \frac{\rho}{\rho_w} \quad (\text{A 1.32})$$

$$F = \frac{29.300 [\Omega \cdot m]}{1 [\Omega \cdot m]} \quad (\text{A 1.33})$$

$$F = 29.3 \quad (\text{A 1.34})$$

Cementation exponent:

$$F = \frac{\rho}{\rho_w} = \frac{1}{\phi^m} \quad (\text{A 1.35})$$

$$m = -\frac{\log F}{\log \phi} \quad (\text{A 1.36})$$

$$m = -\frac{\log 29.300}{\log 0.185} \quad (\text{A 1.37})$$

$$m = 2.000 \cong 2.00 \quad (\text{A 1.38})$$

Appendix C

Computer Specifications

Computer #1 (used for Results 1)

Processor	Intel Quad Core i7 @ 3.07 GHz (8 cores hyper-threaded)
RAM	24 GB (DDR3, 1333 MHz). More RAM means larger sub-volumes can be analyzed both in Avizo and COMSOL. 24 GB is the limit this machine can hold.
Video Card #1	GeForce GTX 480 (1.5 GB GDDR5). The GTX 480 is capable of drawing up to two billion triangles per second. The previous gaming video card took about 15 minutes to rotate a COMSOL mesh on the screen. The GeForce GTX 480 does the same calculation several times per second. DDR5 on the video card is quicker RAM than the computers DDR3 RAM. The speed comparison is roughly 5 x data rate vs. 3 x data rate for GDDR5 vs. DDR3.
Video Card #2	GT 520 (1.0 GB DDR3). This video card was purchased to drive a third monitor as the GTX 480 doesn't include the hardware connections required for driving a third computer monitor.
Hard Drive #1	300 GB VelociRaptor Drive (10,000 RPM). COMSOL appears to use virtual memory when either starting the problem simulation or solving during a relatively large simulation. Solid State hard drives are not recommended as they may wear-out too quickly with heavy writing to the hard drive. The 10,000 RPM hard drive was considered a good compromise between speed, longevity, and hard drive space. Before using the VelociRaptor Drive, I went through multiple hard drive failures due to heavy writing to the hard drive.
Hard Drive #2	250 GB Sata 3.0 (6 Gbit/s, 600 MB/s). This hard drive was used as an experiment to write the thesis.
Hard Drive #3	~14 TB (multiple hard drives, including backup hard drives)
Operating System	Windows 7 Professional (64-bit). Windows 7 64-bit has limits the physical memory: Windows Professional 192 GB, Windows Home Premium 16 GB, Windows Home Basic 8 GB. Using a 32-bit operating system, the RAM is limited to 4 MB. Windows Professional 64-bit was installed so COMSOL and Avizo can use all available 24 GB of RAM.
Power supply	1000 W (1000 W is required for a secondary GPU, future)

Computer #2 (used for Results 2)

Processor	Intel Eight Core Zeon @ 2.7 GHz (2 cores, 32 cores hyper-threaded)
RAM	128 GB.
Video Card	NVIDIA Quadro 6000 GPU (6.0 GB GDDR5). This video card is up to 8 times faster than the NVIDIA GTX 480.
Hard Drive #1	1 TB. Raid 0 configuration used (striped volume increases performance).
Operating System	Windows 7 Professional (64-bit).

Computer #3 (used for Avizo 7 testing)

Processor	Four Intel Xeon E7430 Quad-core processors @ 2.13 GHz (16 cores total)
RAM	256 GB.
Video Card	GeForce GTX 480 (1.5 GB GDDR5). Local video card was used. Remote connection was completed using Cygwin and Putty software via a secure shell (ssh) connection by the way of X11 tunneling (port forwarding).
Hard Drive	500 GB. Storage was used for storing intermediate calculations.
Operating System	RHEL 5.4 Linux.
